

2020 NSF/REU

RESEARCH EXPERIENCE
FOR UNDERGRADUATES
IN PHYSICS



STUDENT RESEARCH PAPERS

VOLUME 31



REU DIRECTOR
UMESH GARG, PH.D.

REU Student Research Papers – Summer 2020
University of Notre Dame – Department of Physics

| Student | Research Title | Page No. |
|--|--|----------|
| Joseph Brett South Dakota School of Mines Tech. | Modeling Hitchhiking Behavior in Chemotaxis of Cancer Cells | 1 |
| Stanford Broadwater Georgetown College | Characterization of the Efficiency of the St. George Detector | 11 |
| Ryan Buechele Case Western University | Simulating Detector Efficiency in Hyperion and STARLiTeR | 21 |
| Amanda Ehnis University of Texas at Dallas | Incorporating Module Tilt Corrections into Track Trigger Code | 31 |
| Mason Faldet University of Wisconsin-La Crosse | Calibrating data from the Munich Q3D spectrograph using ^{168}Er with the (p,t) reaction | 41 |
| Cassidy Favorite Hendrix College | Modeling STARLiTeR detector array with Geant4 | 49 |
| Yusen Feng Xi'an Jiaotong University | The Calculated and Measured Bend Consistency | 59 |
| Shuaijie Li Xi'an Jiaotong University | Understanding the primordial Lithium-7 problem in Big Bang Nucleosynthesis with Ordinary-Mirror neutron Oscillations | 69 |
| Zifeng Liu Xi'an Jiaotong University | Simulation of Fractal Roadway Traffic Using a Simple Roadway Development Model | 79 |
| Sariah Phipps Brigham Young University - Idaho | Investigating Wobbling Motion in ^{135}Ce | 89 |
| Adam Sanchez Michigan Technological University | Monte Carlo Analysis of the St. George Detector using Geant4 | 99 |
| Isabella Valdes Colby College | Analyzing the Efficiency of the St. George Recoil Separator | 109 |
| Mc Kenna Wallace California State University, Chico | Reach Out for Science Outreach: The U.S. Needs You! | 119 |
| Isabella Zane Texas A&M University | Variance extrapolation in an oscillator basis | 129 |

Modeling Hitchhiking Behavior in Chemotaxis of Cancer Cells

Joseph Brett

2020 NSF/REU Program

Physics Department, University of Notre Dame

ADVISORS:

Dr. Dervis Can Vural

Gurdip Uppal

Abstract

Cancer cells migrate in large groups [1] but the dynamics between cells and how they cooperate is not well understood. We hypothesize that low-motility cancer cells may “hitchhike” on other, higher-motility cancer cells, mirroring a behavior found in migrating bacteria [2]. We are creating a python simulation which uses a Voronoi mesh to model the growth of cancer cells inside healthy tissue, accounting for variations in motility. This will make it possible to determine what factors could drive hitchhiking in cells and how this impacts cooperation. Currently the simulation is in its early testing stages, with a wide range of simulations being run to debug the simulation before full-scale simulation.

Introduction

Collective cell migration is a crucial element of many physiological processes, such as regeneration, and is the proposed mode of motility for metastatic cancer [1]. Although the basic mechanics of metastasis and the forces between cells are known, how these influence the evolution and behavioral strategies of the cancer cells is unknown. The interactions and dynamics between migrating cancer cells may also hold clues to the behavior of the metastasizing tumor.

We hypothesize that a hitchhiking behavior found in some bacteria [2] may be a key component of metastasis. Hitchhiking is a genetically favorable trait for an individual cell since hitchhiking cells can devote all resources to reproduction. If hitchhiking is a genotypic trait the hitchhiking cells should grow to dominate the tumor, eventually rooting the tumor in place. On the other hand, if it is a phenotypic trait, meaning hitchhikers and non-hitchhikers are

genetically identical but act differently due to environmental influences, then the hitchhikers and non-hitchhikers could be considered as parts of a multi-cellular organism. In this situation the ratio of hitchhikers to non-hitchhikers could change depending on the needs of the tumor: less hitchhikers for faster tumor migration and more hitchhikers when the tumor arrives at a favorable site to settle. The interaction may be even more complex if the hitchhikers donate resources to the non-hitchhikers in exchange for transportation.

It is also expected that the tightness with which cells are bound together will affect migration. A weak binding would lead to hitchhikers gradually dropping out of the migratory group, potentially seeding new tumors, while a tight binding would preserve the integrity of the group but slow it down.

Our goal is to model metastatic tumors using a cellular model accounting for hitchhiking variations. Comparing the results of the simulations to experimental data could show if hitchhiking is a genotypic or phenotypic trait, how hitchhikers and non-hitchhikers interact and, ultimately, how this affects the cancer's growth.

There are several popular methods for modelling cell tissues, most of which treat the cells as particles. For our model we have chosen to use a Voronoi mesh in two dimensions [3]. Voronoi meshes offer a good compromise between accuracy and time-efficiency and are easy to understand. Most simulations of this type are built to optimize the area and perimeter of each cell, achieving surprisingly accurate simulations of cell behavior. In our model we will also introduce a chemotactic force which affects motile cells. Each motile cell will have a tendency to move in a certain direction, its cell polarity. In a normal situation the cell polarity fluctuates

randomly and cell movement is irregular and non-migratory. A chemical field, which can be modeled as a function of position, will induce a torque on the orientation which will, over time, align the polarity with the chemical field. The motile cells will then move towards a common goal and migration will occur. The non-motile cells, of course, will not move on their own and will simply be swept along by the motile cells.

We are writing the simulation in Python, basing it on simulations written by other research groups [3]. The main innovation in our simulation compared to past simulations is our emphasis on cell motility and inheritance. Our simulations will be run using three cell types: a generic cell which provides a framework, motile cancer cells which follow a chemical gradient, and non-motile hitchhiking cancer cells. If the hitchhiking is a genetic difference, inheritance will be simple with each cell producing cells of its type. If the hitchhiking is phenotypic an inheritance factor will be considered. The inheritance factor will control how cell's motility evolves over cell generations. We also will model intercellular exchange of goods, such as growth factors and food, which will impact heritability, cellular motility speed, and a cell's tendency to reproduce or die.

The results of our simulations can be compared to experimental data collected by a second group. By identifying which simulations are closest to the experimental results the details of the hitchhiking mechanism in cancer cells can be revealed, deepening our understanding of metastatic cancer tumors.

The rest of the paper is split in two. The methods will deal with the principles of the model and how it differs from previous models. The discussion and conclusion will explain the

current state of the program, discuss issues which need to be solved, and outline the next steps of the project.

Methods

Forces on centroids. In the Voronoi model the individual cells move so as to minimize the total energy of the mesh configuration, which is given by [3]:

$$\sum_{i=1}^N \frac{K_i}{2} (A_i - A_i^0)^2 + \sum_{i=1}^N \frac{\Gamma_i}{2} P_i^2 + 2 \sum_{\langle \mu, \nu \rangle} \Lambda_{\mu\nu} l_{\mu\nu}. \quad (1)$$

The first two terms are over the regions (cells) of the mesh where N is the total number of regions, K_i is the area modulus, A_i is the region's area, A_i^0 is the reference area for the region, Γ_i is the perimeter modulus of the region, P_i is the region's perimeter. The last expression is over all vertex pairs, μ and ν , with a shared junction, $l_{\mu\nu}$ is the length of the junction, and $\Lambda_{\mu\nu}$ is the tension of the junction. All terms in eq. 1 can be expressed as functions of the cell vertices [3].

The force on each cell is calculated by finding the negative gradient of the mesh's energy with respect to the cell centroid, meaning only immediate neighbors of the cell, and the cell itself, contribute non-zero terms. Additionally, each cell can also experience a repulsive force from nearby cells if their centroids get too close, ensuring that distance between cells is not so small that force equations break [3].

At each timestep the forces on a cell are calculated and the cell displacement is calculated following the equation of motion,

$$\gamma \frac{d\mathbf{r}_i}{dt} = f_a \mathbf{n}_i + \mathbf{F}_i + \mathbf{v}_i(t), \quad (2)$$

Where γ is the friction coefficient, f_a is the motile force, \mathbf{F}_i is the force due to the energy in eq. 1, and $\mathbf{v}_i(t)$ is a stochastic force [3].

Torque on cells. Each cell has an alignment vector which controls the direction of the cell's movement due to motility. At the beginning of a simulation the alignment vectors are randomly oriented, but at each time step the cells experience a torque which modifies their alignment. Torque arises from minimizing alignment energy between neighboring cells [3] and from the chemical field driving chemotaxis which is modeled as a function of position. The torque on cell i due to alignment energy is calculated as:

$$\tau_i = -\mathbf{n}_i \times \nabla_{n_i} E_{align} . \quad (3)$$

The cells polarity shifts following the equation of motion:

$$\gamma_r \frac{d\theta_i}{dt} = \tau_i \cdot \mathbf{N}_i + \nu_i^r(t) . \quad (4)$$

In this equation γ_r is the rotational friction coefficient, \mathbf{N}_i is the unit vector normal to the plane of the cell, and $\nu_i^r(t)$ is a stochastic term [3].

Cell fitness, growth, and death. The fitness of each cell cancer cell determines how fast it grows and whether it dies at a timestep or not. It is calculated for cell i as,

$$f_i = a \frac{c(\mathbf{x}_i)}{c(\mathbf{x}_i) + 1} - bv_i - c\alpha_i , \quad (5)$$

where a is the benefit due to the chemical field, $c(\mathbf{x}_i)$ is the chemical field at the location of cell i , b is the cost of motility v_i , and c is the cost of the cell age α_i .

Each cell has a reference area, A_i^0 , at which its energy is a minimum. This reference area, slightly modified from [3] by the fitness factor, changes according to,

$$A_i^0(t + dt) = (1 + \eta f_i dt) A_i^0(t), \quad (6)$$

where η is the growth rate and f_i is the cell fitness.

If a cell's fitness is less than 0 it also has a probability to die given by,

$$P_{death} = r_{death} |f_i|, \quad (7)$$

where r_{death} is the rate of death.

Cell division and motility. Each cell has a probability to divide into a parent cell and a daughter cell after its area surpasses a critical area, A_c . The probability that the cell divides is then given by [3],

$$P_{divide} = \chi(A_i - A_c), \quad (8)$$

where χ is the rate of division. When a cell divides the daughter cell inherits most of its attributes directly from the parent, but the age of the daughter cell is initialized to 0 and the motility has a fixed probability that it will mutate. Mutation varies between simulations, based on the system being modeled, but one example relation modeling gradual evolution is,

$$v_{daughter} = v_{parent}(1 \pm \xi), \quad (9)$$

where ξ is from a gaussian distribution centered on a number less than 1, and there is a 50% chance that either + or - is used.

Boundary conditions. The boundary points cannot be considered as actual cells since their area in the Voronoi mesh is infinite, but they still need to move with the interior cells and, when necessary, expand to accommodate more interior cells. Energy is calculated in a similar manner to interior cells (eq. 1), but it must be noted that there are no terms dependent on the boundary point since its area and perimeter in the Voronoi mesh are technically infinite. Each boundary cell also has energy due to the tension between neighboring boundary cells and the angle and stiffness of the boundary junctions [1]. The force on boundary point i due to the energy is found by taking the negative gradient of the energy with respect to the location of the point, just as with interior cells.

Boundary points need to be added or removed as the boundary grows and shrinks.

Points should be added when the Voronoi region of an interior cell extends past the boundary border; in this case the location of the new boundary point is found by reflecting the centroid of the interior cell across the boundary line [1]. There are two scenarios when boundary points are removed: if the boundary point has no interior neighbors [1], in which case it is essentially useless, and if the boundary point has no neighbors which are also boundary points, indicating that it has been enveloped by the interior cells.

Discussion

Currently the simulation is still in the debugging phase. Errors in calculating interactions between interior cells have been resolved, and the remaining issues relate to the boundary conditions. First, many new boundary points are added far from the already existing boundary. Although they do get pulled inwards by boundary tension relatively quickly their distance from

the interior early on could be pulling interior cells outwards. The other issue is that clumps of boundary points are sometimes enveloped by expanding interior cells. Eventually these clusters are removed, but in the short term they do force the interior cells to move around them. Both of these issues can be easily seen in the middle and right panels of figure 1.

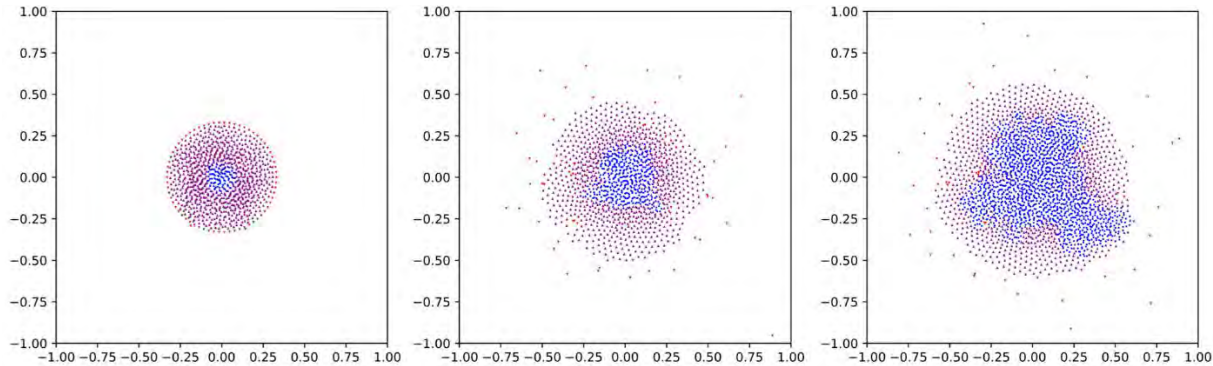


Figure 1. L-R: Initial configuration of a simulation run, with round cancer cells in middle of triangular healthy cells. Cells expanding and boundary moving outwards, with some boundary points enveloped by cells. Cancer cells reproducing and migrating to the right.

Once the simulation is successfully debugged full-scale simulations can begin. Some potential runs may focus on how cancer cells with evolving motility spread out during migration; the expected outcome is that slower cells should filter through the faster cells and be left behind. Another more interesting scenario involves non-motile cancer cells mixed in with motile cancer cells. As in the earlier scenario the non-motile cells should be left behind, but before being completely stranded they should be carried along by the motile cancer cells for some distance. Comparing the hitchhikers' rate of travel to the non-hitchhikers' rate of travel will give insight into the evolutionary advantage or disadvantage given to hitchhikers. It will also be interesting to note how the rate of travel for the motile cells is affected by the hitchhiking of the non-motile cells, and what affect the non-motile cells have on the survival of the tumor as a whole.

Conclusion

Our goal was to create a program which will enable simulation of cancer cells as they evolve and migrate. This program will not be limited exclusively to cancer tissues either. With modifications of the cell classes in the python script it should be possible to model a wide variety of cell types and systems. Although the program is not yet completed the basic principles of the program are working, with only a few bugs left to be solved. Early test runs of the simulation show promising results, with cancer cells reproducing and migrating as expected (figure 1). In the future the results of these simulations could be compared to experimental studies, helping to verify the behavior of metastatic tumors and explain evolution of cooperation in cancer tumors

References

- [1] Cheung KJ, Padmanaban V, Silvestri V, et al. Polyclonal breast cancer metastases arise from collective dissemination of keratin 14-expressing tumor cell clusters. *Proc Natl Acad Sci U S A.* 2016;113(7):E854-E863. doi:10.1073/pnas.1508541113
- [2] Xiong L, Cao Y, Cooper R, et al. Flower-like patterns in multi-species biofilms. *bioRxiv* 550996; doi: <https://doi.org/10.1101/550996>
- [3] Barton DL, Henkes S, Weijer CJ, Sknepnek R (2017) Active Vertex Model for cell-resolution description of epithelial tissue mechanics. *PLoS Comput Biol* 13(6): e1005569.
<https://doi.org/10.1371/journal.pcbi.1005569>

Characterization of the Efficiency of the St. George Detector

Stanford Broadwater

2020 NSF/REU Program

Physics Department, University of Notre Dame

Advisor:

Dr. Manoel Couder

Abstract

The St. George recoil mass separator at the University of Notre Dame studies helium capture reactions of elements lighter than Argon (1). The detection system at the end of the separator consists of two foils which give start time signals and a silicon detector for energy measurement. As particles scatter in the foils, they may miss part of the detection system. As such, it is important to know the efficiency of the detector to correct for proper yield. We studied the geometrical efficiency of the detector with a Geant4 simulation (2). Of particular interest was characterizing the efficiency as a function of the energy of the incoming particles as well as the dependence on where they hit the first foil. Using the results we obtained, we can correct experimental measurements for the number of particles detected and provide a reliable yield of a given nuclear reaction.

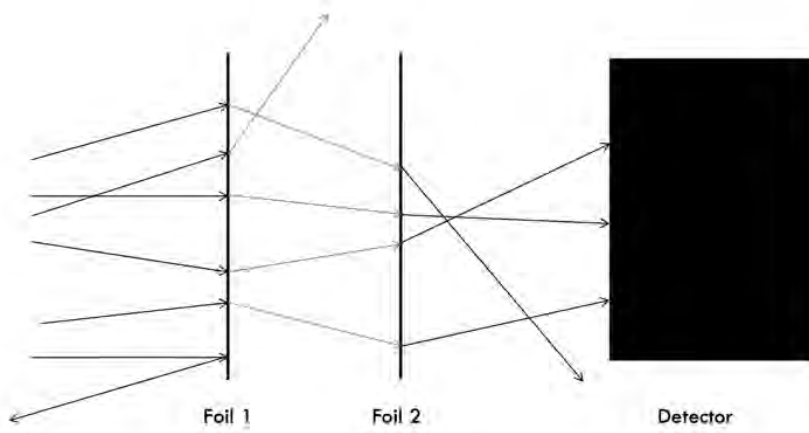
Introduction

We are made from stardust. Ultimately, most macroscopic things are also made from stardust. The process starts with hydrogen in the core of a star. The hydrogen undergoes nuclear fusion, creating helium. Then, helium fuses and so on, producing elements up to iron. The process of the fusion of these lighter than iron elements interests the St. George Project as we seek to better understand how these reactions work.

St. George stands for Strong Gradient Electro-Magnetic Online Recoil Separator for Capture Gamma Ray Experiments and is a device designed to study nuclear reactions involving particle capture fusion. The system is used in inverse kinematic experiments, which inverts the usual fusion process by shooting a beam of the atoms of the heavier element at lighter atoms instead of firing the lighter at the heavier element. In particular, St. George works with helium capture to reenact the fusion process in stars. For the heavier element, St. George can use

elements up to and including Argon from the periodic table. It mainly uses nitrogen to produce Fluorine-19 as a testing example. The machine tries to filter out the leftover nitrogen and helium atoms through use of a Wien filter while the Fluorine-19 travels to a detector. For the purpose of the REU project, we focused on the detection system at the end which is comprised of two time pick-up foils and the silicon detector. Ideally, particles pass through the foils and hit the detector, activating signal clocks to calculate the atoms' velocities.

However, no machine functions perfectly. The atoms are not perfectly filtered out and some Fluorine-19 atoms don't reach the detector. Other atoms may experience multiple scattering effects at the foils or otherwise be deflected off course and never reach the detector. The ratio of particles that stay on course and hit the detector and the total number of particles is termed the geometrical efficiency.



Setup of the St. George Detector Simulations for Geometrical Efficiency

The goal of this REU was to characterize the geometrical efficiency of the detector in terms of radial efficiency and energy efficiency. Radially, we worked to determine if firing the beam of particles at specific positions changes the efficiency of the detection system. For example, we investigated whether hitting the center of the foil causes more deflection than if the beam hit more toward the edge. Additionally, we investigated the relationship of the starting

energy of the particles and the geometrical efficiency. This investigation was furthered by simulating different elements to find a relationship between efficiency and energy per nucleon or if the efficiency had a Z dependence. All of this was done through Geant4 simulations. It is our hope that by obtaining the geometrical efficiency, we can correct for the number of particles detected and provide a reliable yield of production of the recoils of interest for a given nuclear reaction study so we can better understand the evolution of elements in stars.

Differences between the Detector and Simulation

One notable difference between the actual detector and the simulation is the path of the particle. These beams in the simulation followed either a random path or a parallel path. With random particle trajectories, the simulation selected points on the foils at random and constructed the paths of the ions. This allowed the widest possible range of trajectories to occur. At the other extreme, the particle trajectories can be parallel and go straight through the foils. The ions at St. George most likely follow some path between the two extremes. The vast majority of the simulations I ran followed the random beam path.

It is also important to note that in real life, a 70 Gauss magnetic field affects the particles uniformly so they curve after hitting each foil. However, the results in this paper were simulated without the magnetic field for simplicity.

The standard scattering method used by Geant4 may not best recreate the actual scattering of the particles. Two possible alternative methods were attempted in simulations, but both were ultimately not explored. G4Coulomb scattering, the first alternative method, resulted in the simulation abruptly terminating before completion. However, G4WentzelVI scattering failed because of operator coding errors. It may prove viable for future investigation.

Method

The simulations as mentioned previously were run using Geant4, initially using pre-existing code. This code was modified and corrected as needed. Initially, I ran simulations of 100,000 particles with an initial energy of 4-5 MeV. Later, for purposes of more in-depth analysis, I ran simulations of 1,000,000 particles from 0-30 MeV. However, physics and available experimental time constrains us in real life to particles with initial energy between .2 MeV times the number of nucleons of the element simulated and 2 MeV times the number of nucleons. For example, Argon-40 would be run from 8 MeV to 80 MeV. As such, I settled on this as the range of initial energies for the simulation. While initially I only looked at Fluorine-19 as St. George currently experiments with that, I also studied Argon-40, Carbon-12, Beryllium-9 to see if there were any noticeable efficiency dependence on Z, and Phosphorous-31 and Magnesium-24 to compare efficiency further with Carbon-12 and Beryllium-9 respectively. To reflect changes in the detector at Notre Dame, the size and material of the foils was also changed in the simulations from 25.4 mm diameter to 50.8 mm and from Carbon to Aluminum.

The data from the simulations was stored as TTrees in ROOT files (3). ROOT is a software program used to analyze data files. This data was then analyzed using post-processing methods which use Boolean conditions to select the data to be graphed. For example, the graph below was generated by the command *store -> Draw("e_in", "x_det>-100&&x_foil2>-50.4&&x_foil2<50.4")*. Ions that miss a foil or the detector are assigned values of -1000, so selection statements like *x_det>-100* are needed to see the particles that actually hit the detector.

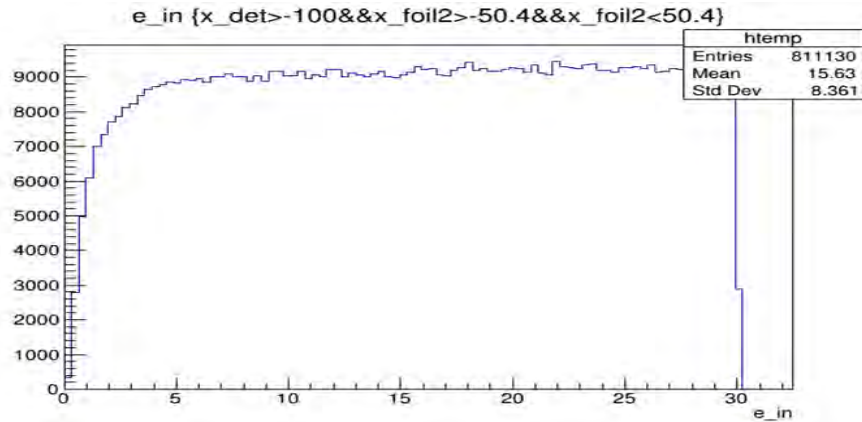


Figure 1 Selection Statement Example

While I used ROOT macros to analyze the data, I used Excel to do calculations and create scatterplots of different data sets. Geometric efficiency was calculated by taking the number of particles in a given energy or radius range that hit both foils and the silicon detector and dividing by the total number of incoming particles in the range. For graphing purposes, I took the midpoint of the given range as the x-coordinate and the efficiency as the y-coordinate. In the case of plotting energy efficiency, I also divided the energy x-coordinate by the number of nucleons so that the x-range would be between .2 and 2 MeV/nucleon to aid in comparative analysis of different elements.

Results and Discussion

The dependence of efficiency on energy per nucleon follows general intuition: the more energy the particles have, the more likely they are to go through the foils with minimal deflection and hit the detector, resulting in high efficiency. While the F shows interesting trends such as how Fluroine is mostly on the top of or Carbon is mostly on the bottom, there is no noticeable Z-dependence. Indeed, I included analysis of Magnesium to see if like Beryllium, it would remain mostly in the middle, but it does not. The points all follow a general curve with different trends for different elements, but the differences do not depend on Z.

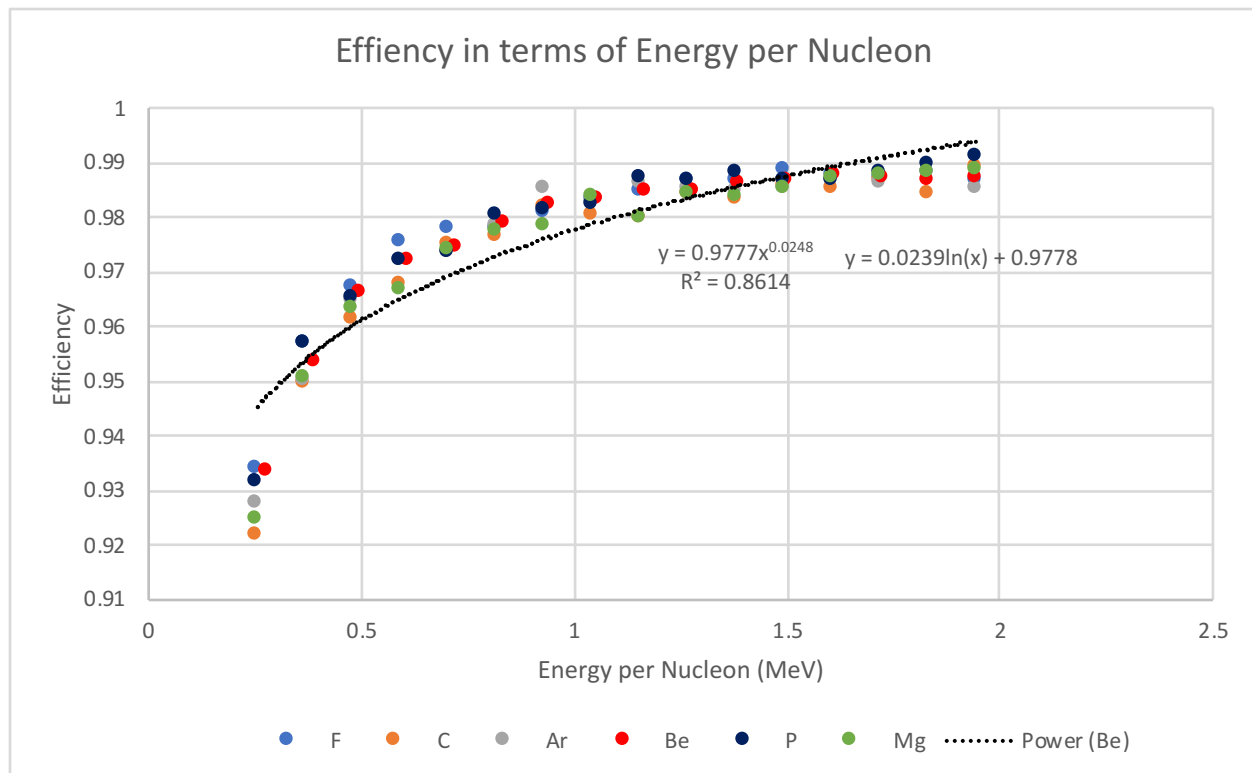


Figure 2 Efficiency of incoming ions in terms of Energy per Nucleon

The trend of the graph, when looking for simple functions to compare it with, is best described as logarithmic though it can be reformulated as a fractional power of x. This logarithmic trend is also demonstrated in Figure 1. However, the trend is not so easily regressed into an equation as demonstrated by the trendline. Indeed, several regressions were attempted on various data sets, but they lacked predictive power. Regressions did gain more predictive power as more particles were simulated, but they failed to follow the steep curve and level off afterward. However, when I changed the simulation to have initial energies based on nucleons instead of a blanket 0-30 MeV, the steep curve was cut off as it takes place below the $.2*A$ MeV cutoff.

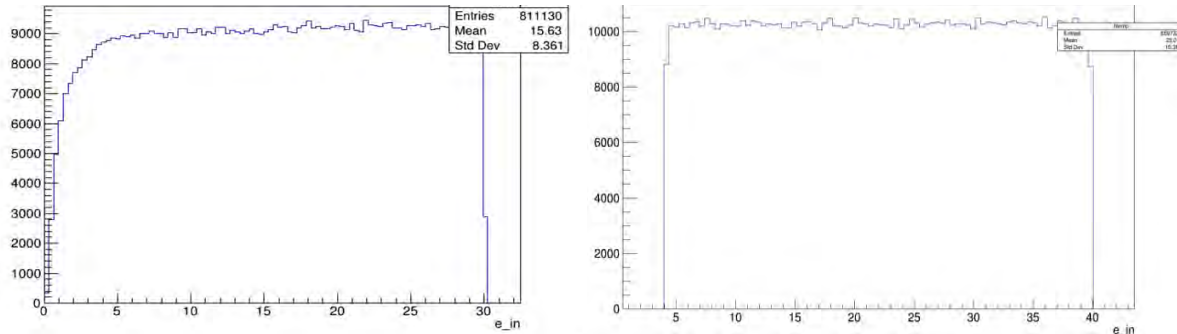


Figure 3: Comparing curves of Fluorine-19 with starting energies of 0-30 and 4-40 MeV

This produced more accurate regressions as in Figure 4 within the $.2^*A-2^*A$ MeV range.

Outside that range, the regressions still lack predictive power, especially on the steep curve, but that does not matter as much as particles cannot be used experimentally outside the range.

Perhaps, the trend would better fit a logistical function with a horizontal asymptote of $y=1$, but such a regression was beyond the scope of simple Excel functions.

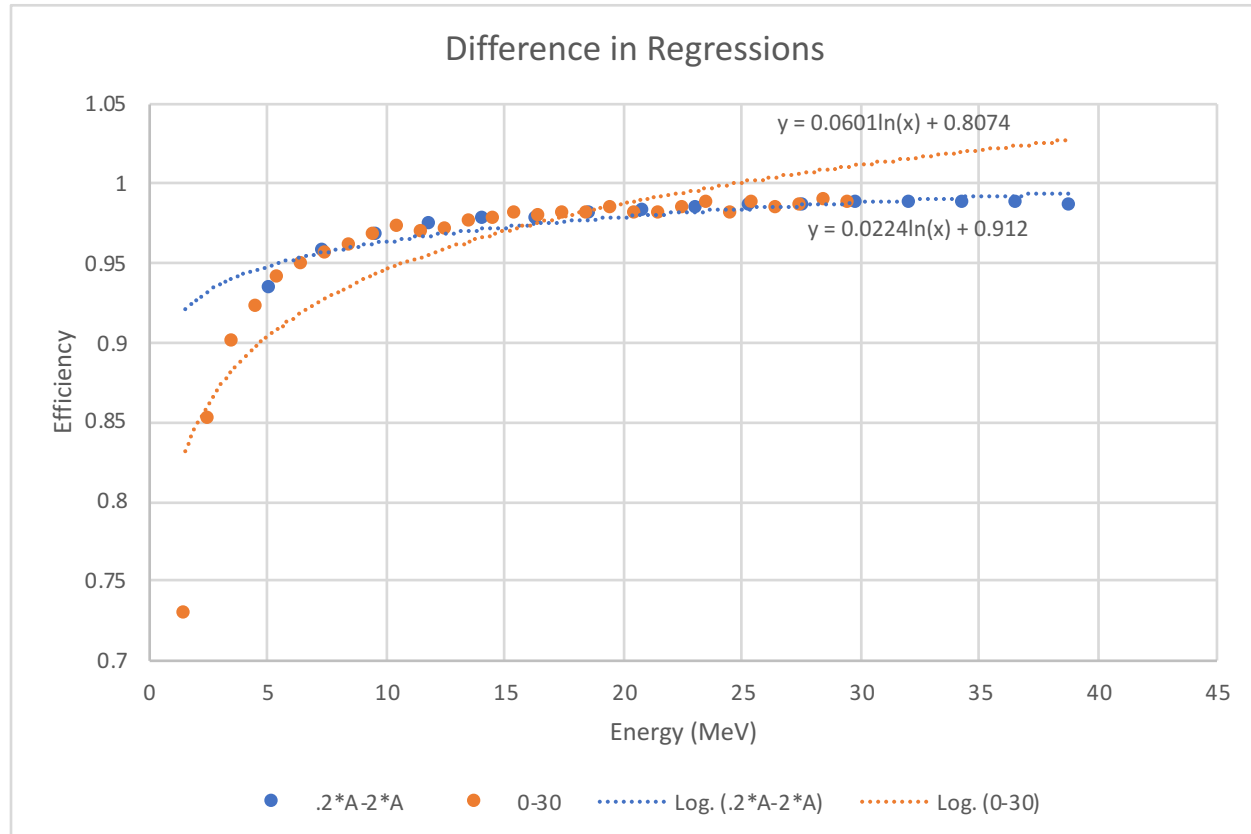


Figure 4 Difference in Fluorine-19 regressions

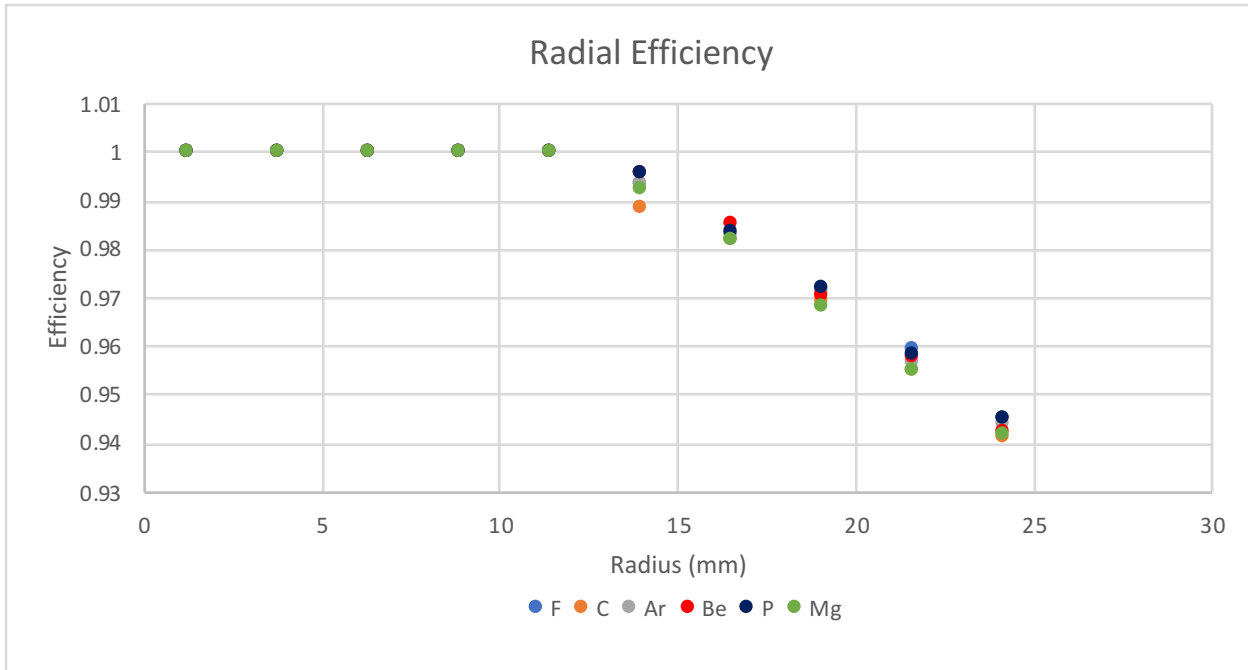


Figure 5 Radial Efficiency

The radial efficiency also follows intuition: particles that hit closer to the edge of the first foil are more likely to be scattered away from the second foil and the silicon detector while particles that hit closer to the center of the foil are more likely to retain a trajectory that reaches the detector. However, for the first half-inch, the radial efficiency remained at a steady 100%.

Conclusion and Further Work

This REU sought to characterize the geometric efficiency of St. George and found it to be very efficient. Particles with energies between $1^{*\#}$ of nucleons MeV and $2^{*\#}$ of nucleons MeV generally are efficient above 98%. Radially, any particles that hit the foil within 1 in. of the center have 100% efficiency.

Future analysis may look at simulations involving even more elements to find trends in graphs of energy per nucleon. It would also be useful to add the 70 Gauss magnetic field and see if it changes the efficiencies. Alternative methods of scattering would also be worth investigating. By refining the geometrical efficiency even more in these ways, St. George will be

able to correct the experimental data from the reactions, leading to better understanding of how these nuclear processes function. After all, it's one thing to know that we are stardust; it is another thing entirely to know how dust can become something as wondrous as our universe.

References

1. M. Couder , et al., *Design of the recoil mass separator*, Nuclear Instruments and Methods in Physics Research A 587 (2008) 35-45
2. S. Agostinelli, et al., GEANT4 - A simulation toolkit, Nucl. Instrum. Methods Phys. Res. A 506 (2003) 250–303
3. Brun R and Rademakers F ROOT Object Oriented Data Analysis Framework *New computing techniques in physics research V. Proceedings, 5th International Workshop, AIHENP '96 (Lausanne, Switzerland, September 2-6, 1996)*

Simulating Detector Efficiency in Hyperion and STARLiTeR

Ryan Buechele*

2020 NSF/REU Program, Department of Physics, University of Notre Dame

Advisor: Dr. Anna Simon[†]

Department of Physics, University of Notre Dame

Abstract

The study of γ -ray emission from excited nuclei plays a crucial role in nuclear physics by offering insight into the structure of nuclei and the formation of heavy elements in stars. The Hyperion and STARLiTeR systems are detector arrays currently housed at Texas A&M University used in the study of astrophysical nuclear processes. To better understand the efficiency of the γ -ray detectors in these arrays, computer simulations can be built in Geant4 to model the interaction of γ -rays with the detector materials. Simulations like these allow researchers to quickly and easily determine the effects that changes in the detector setup have on the γ -ray spectrum recorded in experiments. A simulation was constructed to most accurately reproduce data taken in the STARLiTeR system for radioactive γ -emitting ^{137}Cs and ^{60}Co calibration sources and was used to calculate an efficiency function for the detector as a function of γ -ray energy.

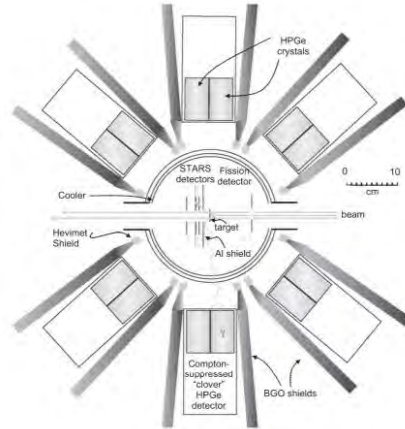
I. INTRODUCTION

γ -ray emission from excited nuclei is one of the most useful ways to determine information about nuclear systems; observing γ -ray spectra from different nuclear processes can reveal energy structures of nuclei, as well as help determine cross sections of nuclear reactions. This data is valuable in a variety of fields, from understanding processes of nuclear fusion and describing how heavy elements are formed in stars, to designing nuclear reactors for energy production and safely containing and handling radioactive material in disarming nuclear weapons.

STARLiTeR and Hyperion are detector arrays housed at the Texas A&M Cyclotron Institute that are used in the study of γ -ray emission from various nuclear systems. STARLiTeR consists of six individual detectors in a circle around a target chamber where reactions take place; Hyperion is an upgraded version of the system, with up to fourteen detectors distributed in a hemisphere around the target chamber. Visualizations of each detector array are shown in Figure 1.



(a) CAD Drawing of Hyperion array [1]



(b) Schematic of STARLiTeR Array [2]

FIG. 1: Visualizations of detector setups

A key limiting factor in the experimental collection of γ -ray emission spectra is the efficiency of the detectors; γ -rays scatter in every direction from a reaction, so the detector absorbs only a fraction of the total emitted γ -rays. This fraction is affected by the size and shape of the detector, as well as the effects of other outside material on the γ -rays. Ideally, a good detector covers the largest solid angle around the γ -ray source, in order to capture the greatest number of events. Additionally, it is necessary to consider how other materials in the system may absorb or scatter some amount of γ -rays, preventing them from being absorbed in the detector. Knowing the efficiency of the detector is crucial in understanding the full scope of γ -rays emitted in a nuclear reaction. In order to learn about detector efficiency, computer simulations of detector arrays can be used instead of running numerous experiments in the lab, which are often expensive and time-consuming.

The main component of this project is a simulation built in Geant4 of a single detector of the type used in STARLiTeR and Hyperion. Geant4 is a simulation tool for radiation transport through matter; it uses Monte Carlo algorithms to model probabilistic interactions of radiation with objects or particles. After building the shapes of the detector components, Geant4 simulates a large number of γ -ray events, and calculates their trajectories and interactions with the detector materials. From this, Geant4 outputs a data file describing the amount of energy deposited from each γ -ray in the germanium crystals, and this energy spectrum can be examined using the data analysis software ROOT.

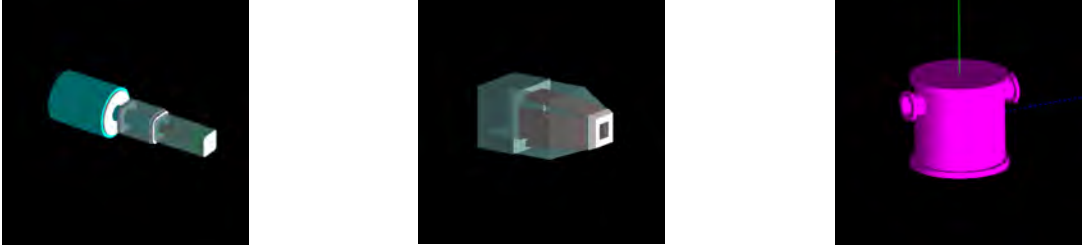
Ultimately, the goal of this work is to generate a function describing the efficiency of

the detector across a range of energies in order to determine the optimal setup for the detector in experiments. The following sections describe the development of the simulated geometries of the detector array's components and the manipulation of these components in order to compare the output of the simulation to known experimental data from standard radioactive calibration sources (^{137}Cs and ^{60}Co) and calculate the efficiency of the detector setup. With an accurate simulation, predictions can be made about future experiments, particularly those with higher energy γ -ray emissions than those from the aforementioned calibration sources.

II. DETECTOR CONSTRUCTION AND SIMULATION

The central component of the γ -ray detector used in the Hyperion and STARLiTeR arrays is a collection of four high-purity germanium (HPGe) crystals. Germanium is a semiconductor, so a γ -ray can be absorbed in the crystal by exciting an electron from the valence band to the conduction band. A potential difference is applied across each crystal, which causes the excited electrons to form a current that can be measured and interpreted to determine the energy of the absorbed γ -ray. As γ -rays interact with the crystals, the added energy may cause their temperature to rise and thermally excite additional electrons to the conduction band; to prevent noise in the measured current due to the thermally excited electrons, a dewar of liquid nitrogen is situated behind the detector casing with a conduit connecting the crystals to the liquid nitrogen to keep them cool. The crystals, electronics, and cooling apparatus are enclosed in a thin aluminum casing, which keeps the crystals contained under vacuum while adding the least amount of additional material between the crystals and γ -ray source.

The detector is placed inside a Compton suppression shield which is comprised of an aluminum casing containing four bismuth germanate (BGO) crystals which surround the front end of the detector. The purpose of this shield is to detect when γ -rays scatter from a HPGe crystal and only deposit a portion of their energy in the detector; by knowing when γ -rays are only being partially absorbed, that event can be excluded from the spectrum since it does not represent the complete γ -ray energy. The detectors are arranged around an aluminum chamber which contains the source of the γ -ray emissions. Figure 2 shows the construction of the detector components in the Geant4 simulation.



(a) Detector with N_2 dewar (b) Compton suppression shield (c) Aluminum target chamber

FIG. 2: Some Geant4 geometries used in the simulation

Geant4 (GEometry ANd Tracking) is a simulation software that uses Monte Carlo methods to simulate radiation transport and interactions with matter. The simulated shapes of the detector components are built combining simple geometric objects like cubes and cylinders with Boolean operations (union, subtraction, and intersection). For each γ -ray event, an initial direction is randomly selected for the photon; as it travels through a material, Geant4 calculates the mean free path and uses this to randomly select a distance for the γ -ray to travel before interacting with another particle. At each interaction, Geant4 uses built-in physics models to calculate the probability of different types of interaction such as absorption, Compton scattering, or pair production and uses these probabilities to determine the energy and trajectory for the photon after the interaction. This process of calculating a mean free path, interaction, and trajectory repeats until all particles produced in the event either travel far enough away or fall below a certain energy threshold. During a run of the simulation, Geant4 performs a large number of γ -ray events, records the energy absorbed by each detector component during each event, and exports this data to ROOT for analysis.

III. METHODS

A γ -ray energy spectrum describes the amount of different energy γ -rays absorbed in a detector, and the spectrum has a number of features related to the interaction of the γ -rays with the detector material. The most prominent feature is the photopeak on the far right of the spectrum, which results from total absorption of the incident γ -ray energy. At a slightly lower energy than the photopeak is the Compton edge, which results from a γ -ray scattering from an electron in the detector, then leaving the crystal. The energy imparted to the electron depends on the incident γ -ray energy and the angle at which it scatters

off, so there is a Compton plateau across the range of energies that can be absorbed in Compton scattering. Some γ -rays can also scatter off of materials surrounding the detector and then be absorbed, resulting in a smaller backscatter peak located around the energy difference between the photopeak and Compton edge. An example of a γ -ray spectrum from a radioactive ^{137}Cs source is shown in Figure 3. For γ -rays that exceed twice the mass energy of an electron ($m_e = 511 \text{ keV}$), there is a chance that the γ -ray will produce an electron-positron pair, which can in turn recombine into two photons with energy equal to m_e ; one or both of these photons can escape the detector, leading to two smaller single- and double-escape peaks, located at m_e and $2m_e$ less than the photopeak energy. These pair production effects are only significant for γ -ray energies much greater than the electron mass ($E_\gamma > 5 \text{ MeV}$).

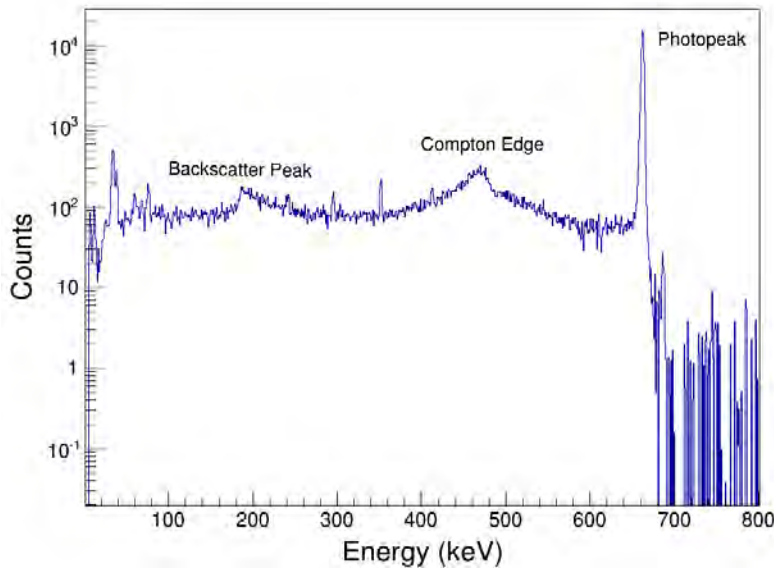


FIG. 3: γ -ray energy spectrum for ^{137}Cs

The exported energy data from the simulation was used to create γ -ray energy spectra by summing the energy deposited in each of the four HPGe crystals. A histogram plot was created and analyzed in ROOT showing the number of events recording a given amount of energy in the detector. The simulation was run using γ -ray cascades from radioactive ^{137}Cs and ^{60}Co sources; ^{137}Cs emits just one γ -ray at 661 keV, while ^{60}Co emits two γ -rays at 1172 keV and 1332 keV. The resulting spectra were compared with calibration data from the actual detectors. Spectra for both sources are shown in Figure 4, comparing the simulation

output to the experimental spectra.

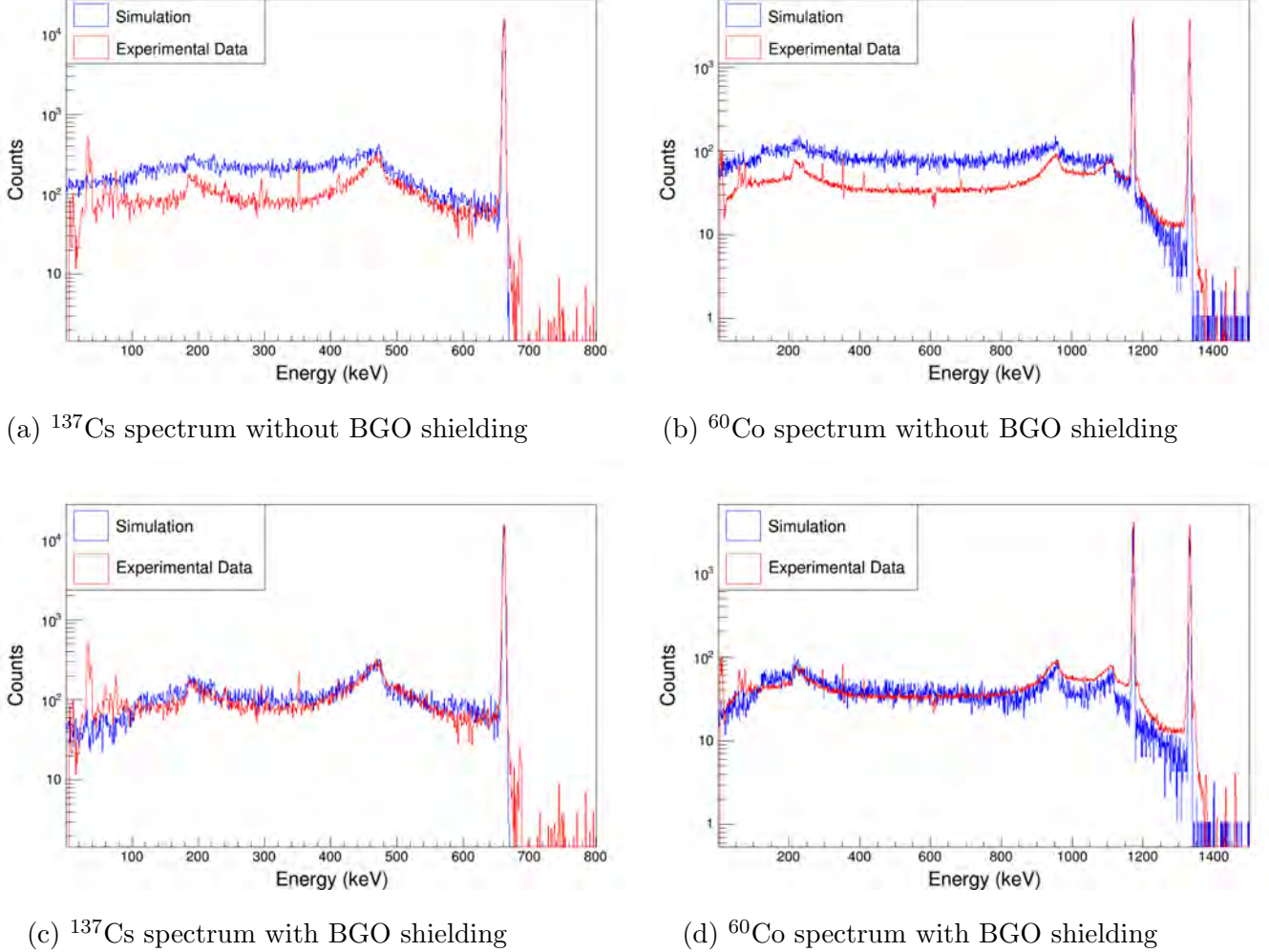


FIG. 4: γ -ray spectra for simulated ^{137}Cs and ^{60}Co sources

The first step in configuring the simulation to match experimental data was to determine the photopeak width as a function of energy. The photopeaks in the provided experimental data were fit to a Gaussian curve to determine their width σ . A linear fit was applied to determine the width at any energy, and this fit was applied in the script controlling the process for γ -ray events in the simulation. In addition, the simulation was normalized to match the photopeak heights to the experimental data. This was achieved by scaling the simulation output by the ratio of the total counts in the photopeak of the experimental data to the total counts in the simulated photopeak; in both cases, the total counts were calculated by integrating the spectrum over a 5σ range around the photopeak energy. The

final step in matching the simulated spectra to experimental spectra was accounting for the Compton suppression shield. If any of the four BGO crystals recorded an absorbed γ -ray, that event was removed from the spectrum since the full energy of the γ -ray was not absorbed in the detector. Removing the BGO events lowers the Compton plateau in the spectrum, causing the backscatter peaks and Compton edge to become more pronounced, as seen in Figures 4c and 4d.

IV. RESULTS AND DISCUSSION

The photopeak efficiency of the simulated detector at a particular energy was determined by running the simulation with five million monoenergetic γ -ray events and calculating the percentage of the total simulated events N_{total} that were fully absorbed in the detector. Thus, the efficiency ϵ of the detector as a function of incident γ -ray energy E_γ is calculated as the integral of the spectrum $N(E)$ over a 5σ range around the photopeak energy divided by the N_{total} :

$$\epsilon(E_\gamma) = \frac{1}{N_{total}} \int_{E_\gamma - 5\sigma}^{E_\gamma + 5\sigma} N(E)dE \quad (1)$$

A plot of detector efficiency up to 10 MeV is shown in Figure 5. This efficiency function is unique to this type of single detector setup, and the simulation allows insight into the behavior of the detector in an environment without noise or background radiation from other objects in the room with the detector setup. The detector has a maximum efficiency of about 0.5% around 200 keV; γ -rays with a lower energy are more often absorbed or scattered by other detector materials before reaching the HPGe detector crystals, while higher energy γ -rays are more likely to reach the HPGe, then pair produce or scatter outside the crystals, thus only depositing a portion of their energy in the detector.

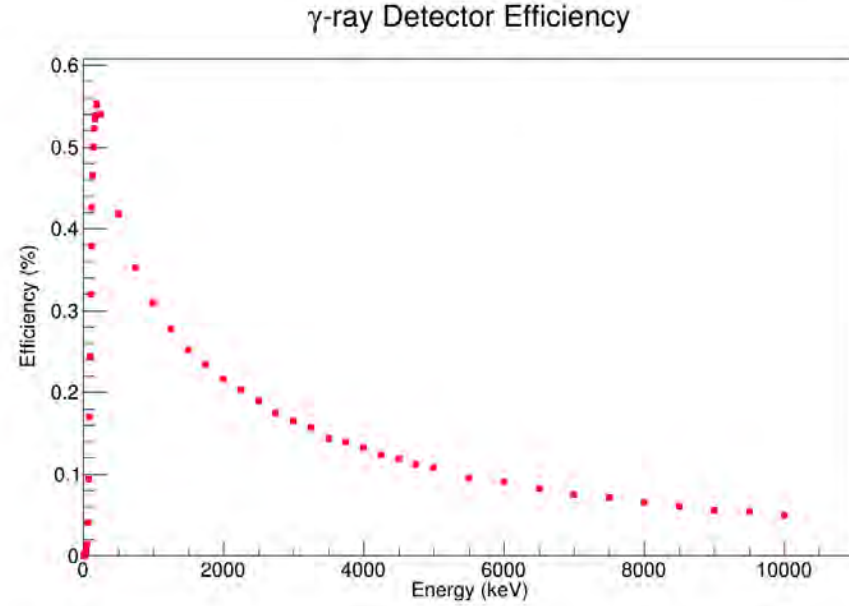


FIG. 5: Detector efficiency from 0-10 MeV

V. CONCLUSIONS

Understanding the efficiency of γ -ray detectors is crucial to the laboratory study of nuclear reactions. This work describes the development of an accurate simulation built in Geant4 of a single γ -ray detector of the type used in the Hyperion and STARLiTeR detector arrays. The output of the simulation has been configured by recreating experimentally determined γ -ray spectra from ^{137}Cs and ^{60}Co . The photopeak efficiency for this particular detector has been determined for energies up to 10 MeV, with a maximum efficiency of around 0.5% at around 200 keV. In the future, this simulation can be easily extended to model larger experimental setups with a greater number of detectors in different configurations, such as the full STARLiTeR or Hyperion arrays. This can be utilized to optimize the detection of γ -rays by testing potential modifications to the detector array without the time or cost associated with running repeated experiments in the lab. In this way, the development of this simulation greatly accelerates the process of collecting useful data in the study of nuclear processes.

ACKNOWLEDGMENTS

I would like to thank my advisor, Dr. Anna Simon, the REU program coordinator, Dr. Umesh Garg, and the entire University of Notre Dame Physics department for working hard to ensure the success of the REU program this year while facing the challenges of the ongoing global pandemic. I would also like to thank Cassidy Favorite, who worked with me on this project for the duration of the summer, and Orlando Gomez, for his assistance in proofreading and providing feedback on parts of this report.

* rtb89@case.edu

† anna.simon@nd.edu

- [1] R. Hughes, J. Burke, R. Casperson, S. Ota, S. Fisher, J. Parker, C. Beausang, M. Dag, P. Humby, J. Koglin, *et al.*, Nuclear Instruments and Methods in Physics Research Section A: Accelerators, Spectrometers, Detectors and Associated Equipment **856**, 47 (2017).
- [2] S. Lesher, L. Phair, L. Bernstein, D. Bleuel, J. Burke, J. Church, P. Fallon, J. Gibelin, N. Scielzo, and M. Wiedeking, Nuclear Instruments and Methods in Physics Research Section A: Accelerators, Spectrometers, Detectors and Associated Equipment **621**, 286 (2010).

Incorporating Module Tilt Corrections into Track Trigger Code

Amanda Ehnis

2020 NSF/REU Program

Physics Department, University of Notre Dame

Advisors:

Dr. Kevin Lannon and Dr. Michael Hildreth

Abstract

Protons are sent towards each other every 25 nanoseconds in the LHC. This generates massive amounts of data. The track trigger reduces the amount of data produced, keeping only certain events. In order to keep up with the HL-LHC upgrade, the track trigger in the CMS detector was updated so as to increase efficiency by taking into account the geometry of the detector. The track trigger works by taking in the stubs from the layers and disks and matching them together to form tracklets. After matching, the tracklets and additional stubs are matched together to find a best fitted trajectory. To determine which stubs go together, the measured bend, which is the horizontal distance traveled between two matching stubs caused by the magnetic field of the CMS detector, and the projected bend are used. If the measured bend and projected bend are close enough, the stubs are matched together. The projected bend can be found more accurately by accounting for geometrical details of the CMS detector. The lookup tables were expanded to contain this information. The efficiency was increased in the endcap section of the detector by 0.5% but decreased in the overlap section by 0.5% which was unexpected.

Introduction

The LHC (Large Hadron Collider) at CERN collides two proton beams together to search for and study new types of particles such as the Higgs boson. The Compact Muon Solenoid (CMS) is used to measure the trajectory, momentum, and energy of the particles as they pass through it. The goal of

the CMS experiment is not only to find new particles in the standard model and explain them more fully, such as in the case of the Higgs boson, but to find suggestions of something beyond it; for example, supersymmetry, extra dimensions, a possible candidate for dark matter, or a reason for the imbalance of matter and antimatter in our universe.

The beams are crossed once every 25 nanoseconds because rare particles and collisions of interest are produced at a highly reduced rate from other types of collisions. During an experiment each of these beam crossings create an event, which usually results in one or more collisions. This generates an enormous amount of data, too much to store and process fully. If every event that happened were to be recorded, there would be 40 terabytes generated per second.

To have a manageable sized data set, something has to be done to reduce the number of collisions that are studied. The software used in the CMS hardware simulation that analyzes the collisions is called the track trigger. The CMS tracker (as shown in figure 1) is composed of six layers of silicon, each split into two sub-layers. There are also disks positioned like caps to the cylinder which pick up particles that may have only gone through a few layers. The barrel consists of only layers, the endcap only disks, and the overlap contains both layers and disks. The geometry of the modules is described by three coordinates, the radial coordinate r , the longitudinal coordinate z , and the azimuthal coordinate ϕ . The value of eta, η , is the pseudorapidity which tells the angle of the particle relative to the beam. The regions of the barrel are determined by their η value.

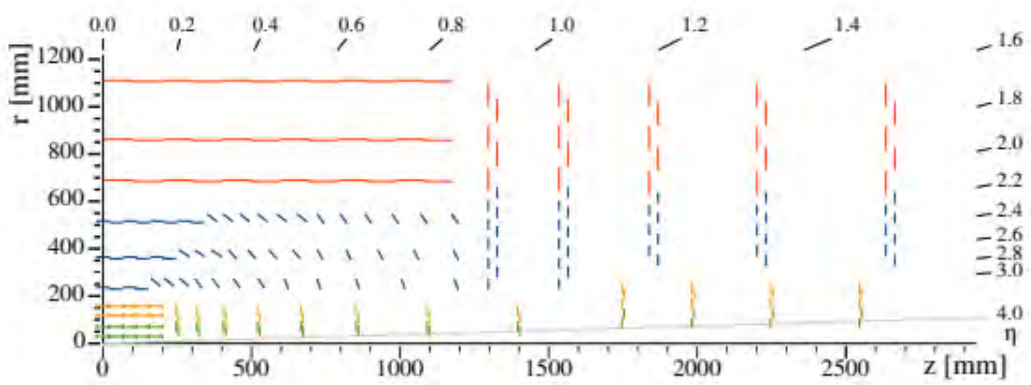


Figure 1: Geometry of CMS detector, showing layers and disks in blue and red.[1]

The tracker records the positions of particles, called stubs, as they pass through the six layers and five disks. The track trigger uses this data in three steps to construct trajectories for these particles. The seeding step takes two stubs from adjacent modules and builds a tracklet. In the next step called projecting, the tracklet is used to match further stubs with it. At the end, the fitting step takes all the stubs in the tracklet and matches them to produce the best fitting trajectory. In all of these steps the track trigger uses a lookup table to match a trajectory to them. Lookup tables are used because this software will be implemented in the hardware using FPGAs, which process data quicker, but require simpler algorithms than a computer. It takes the current tracklet and calculates the projected bend, which is due to the influence of the magnetic field of the solenoid, and matches it to the observed bend to determine whether the stubs match.

The track trigger sends the reconstructed tracks to the Level 1 Trigger (L1 Trigger). The Level 1 Trigger takes these tracks and other data and decides

which collisions to keep. This reduces the data from collisions by a factor of 400.

In 2027 LHC will turn into High Luminosity Large Hadron Collider (HL-LHC). This high luminosity means that there will be even more collisions than there were previously and thus the track trigger must be added to further restrict the number of recorded collisions.

Thus, the goal of this research was to make changes, provided by previous research, to the code based on the geometry to increase the efficiency of the CMS detector. This was done by taking simulated collision events and using the track trigger to put together projected tracks. Those tracks that were both high energy and deemed to be correct were kept. Since the simulated data is well known, the false tracks can be detected and the efficiency can be calculated. In the code, corrections were implemented for the tilt angle of the modules. Increasing the efficiency will allow for new particle interactions to be found more easily. Eliminating false tracks will reduce the amount of superfluous and inaccurate data, allowing the track trigger to focus on only pertinent data.

Methods

Prior to this research, Arianna Garcia implemented module tilt corrections for an older version of the CMSSW(CMS software) code [2]. The code has meanwhile been updated, so the previous changes had to be merged with existing code. In the current version, the code has changed in the areas of the

tracklet engine, the tracklet processor, the match engine, the projection router bend table, and some minor changes to the settings and util files.

The current version of the code had one lookup table, located in the tracklet engine for the seeding process, for the whole detector. The changes made it so that there are now three separate lookup tables, one for each region of the detector. New functions for calculating the bend were created, one for layers, called bendBarrel and one for disks called bendDisk. These new bend functions take in different parameters than the old bend functions in order to use the module tilt corrections.

The tracklet processor did not exist in the code that Arianna was working with. But it also has a division of three lookup tables. Because of this, it was easy to put in the different bend functions. Because this code is not being used currently by this research, even though changes were made, they have not been tested yet.

The projection router bend table file gives the endcap projected bend. This uses a different disk bend function, with a correction factor for the geometry. While it would make sense to have the barrel projected bend in the projection router bend table as well, it has been put into the match engine instead. This is because to move the code from the match engine to the projection router bend table would require significant rewriting of the code. In the match engine, the barrel lookup table now includes z information and uses a different bend function for layers with access to bend window parameters.

The last two files changed were the settings header and the util header files. All the bend functions mentioned above were placed into the util header.

Constants for use in the other files above were added to the settings header file.

Results

All the changes made in Arianna’s previous research were made to the current version of the code. After the changes to the code were made, the code was run on 500 $t\bar{t}$ (which stands for a top quark and its antiparticle) events. A table of efficiencies was created from running the new version of code both with and without the above modifications, and then with and without reduced bend window sizes, as shown in Table 1.

Table 1: Table of Efficiencies for 500 RelVal $T\bar{T}$ events for original and modified code. Efficiency is in percentage form.

| | Barrel $ \eta < 1.0$ | Overlap $1.0 < \eta < 1.75$ | Endcap $1.75 < \eta < 2.4$ | Overall $ \eta < 2.4$ |
|---------------------------------------|--------------------------|----------------------------------|---------------------------------|---------------------------|
| Original | 96.7 | 95.5 | 94.8 | 96.0 |
| Modified | 96.7 | 95.0 | 95.3 | 95.9 |
| Original with Reduced Bend Windows | 96.4 | 94.0 | 92.0 | 95.0 |
| Modified with Reduced Bend Windows | 96.7 | 95.0 | 95.3 | 95.9 |

The efficiencies stayed nearly the same in the barrel, decreased by 0.5% in the overlap portion, and increased by 0.5% in the endcap. The overall efficiency went down by 0.1%. The decrease of efficiency in the overlap portion is shown in figure 2, at a midway modulus of η . The increase of efficiency in

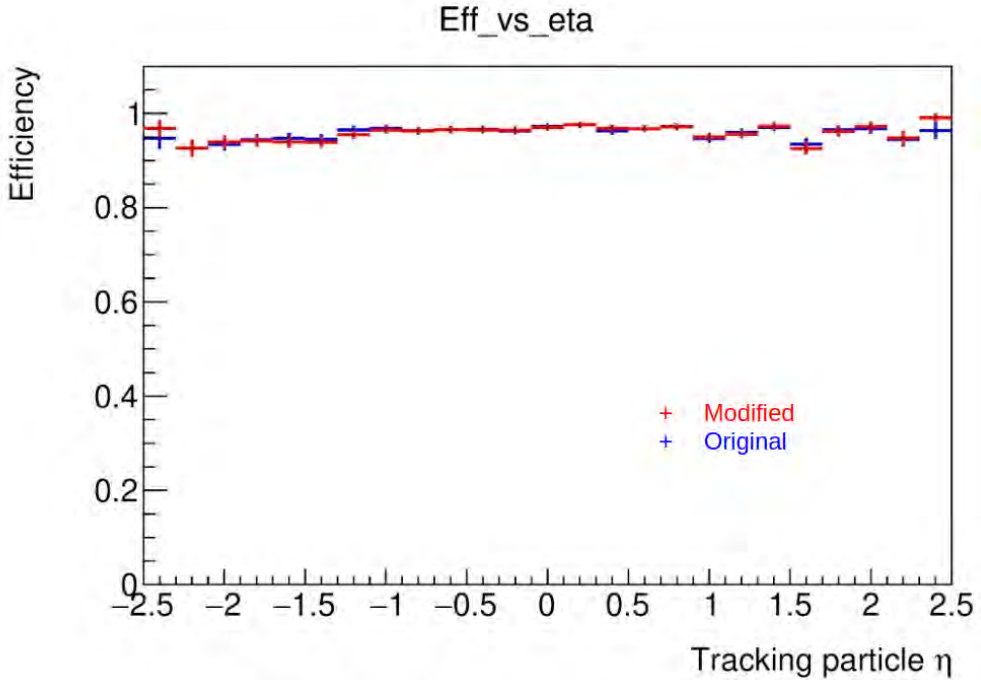


Figure 2: This plot shows the efficiency plotted against the eta.

the endcap region is shown at the high modulus of η . The efficiencies should have all increased due to the module tilt corrections because the corrections would have increased the accuracy of the projected bends. If more projected bends matched the observed bends, less true tracks would be missed.

Since it seems that the problem is in the overlap section, efficiency was calculated for the two seeds of the overlap, numbers 6 and 7. In figure 3, the efficiency for seed 7 is shown in the original and modified code, both with original bend windows.

The efficiencies were also calculated with reduced bend windows. Reducing bend windows means that for checks, the range of projected bends that are close enough to be valued as true for the lookup tables, is smaller. Efficiencies

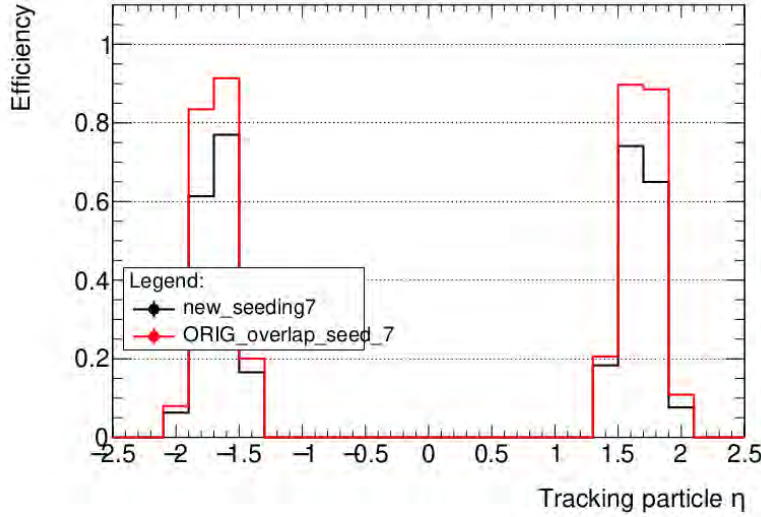


Figure 3: This plot shows the efficiency plotted against the eta for seed 7, in the overlap.

in the modified code with both normal and reduced bend windows were the same. The original code with reduced bend windows has reduced efficiency in comparison to the modified code. It is good that the modified code did not reduce with the reduced bend windows in comparison to the original because it likely means that the code with the module tilt corrections has values closer to the real value and thus didn't get cut out when the window reduced. If the projected bend values are further away from the real values, they will likely get thrown out when the window reduces.

Conclusion

All the changes have been made in the new version of code. While using these new module tilt corrections should have in theory increased the efficiency overall, adding the changes to the code made improvements in the endcap of

0.5% and made efficiency in the overlap decrease with a drop of 0.5% and overall efficiency dropped by 0.1%. The results indicate that while the changes have been made, they may not be properly implemented in the code for the overlap. Further research would need to be done to find out which part of the code is contributing to the loss in efficiency. This could be done by checking why seeding efficiency is low in seed 7, checking the truncation, and modifying the bend windows. While the changes to the module tilt have been implemented, these steps need to be taken to further increase the efficiencies.

References

- [1] CMS Collaboration. The phase-2 upgrade of the cms tracker cern-lhcc-2017-009.
- [2] Arianna Garcia. Implementation of titled module bend corrections in the cms detector track trigger. 2020.

Calibrating data from the Munich Q3D spectrograph using ^{168}Er with the (p,t) reaction

Mason Faldet
2020 NSF/REU Program
Physics Department, University of Notre Dame

Advisor: Dr. Ani Aprahamian and Dr. Shelly Lesher

Abstract

Nuclei can deform in transition between excited states. One such deformation, called β -vibration, corresponds to the 0^+ excited states. In effort to study β -vibration we are working to identify 0^+ excited states in rare-earth nuclei via the (p,t) reaction. Data was collected in a one-dimensional histogram with the x-axis corresponding to channel of the detector and the y-axis corresponding to counts. Before this data can be analyzed the histograms must be calibrated, i.e. matching each channel to the corresponding energy level. The isotope ^{168}Er has been studied in previous experiments thus is used as calibration data. This allows us to identify the proper positions of 0^+ excited states in lesser studied rare earth nuclei.

Introduction

When nuclei transition between excited states they don't always maintain a spherical shape, instead they may deform to prolate (football) or oblate (frisbee) shapes. While nuclei are deformed, they vibrate. Two types of nuclear vibration are γ -vibrations corresponding to the 1st excited state and β -vibrations theorized to correspond to 0^+ states [1]. Nuclear physicists have observed γ -vibration however β -vibration is unknown. Thus, in effort to fully understand the shape and motion of nuclei we are identifying 0^+ states in even-even rare earth nuclei.

To populate the 0^+ states of rare earth nuclei we use the (p,t) reaction. A (p,t) reaction consists of a beam of protons, which interacts with a target and releases tritons, one proton and two neutrons. Tritons are then detected using a focal plane detector. In particular the following (p,t) reactions were preformed: $^{176}\text{Yb}(\text{p},\text{t})^{174}\text{Yb}$, $^{180}\text{Hf}(\text{p},\text{t})^{178}\text{Hf}$, and $^{170}\text{Er}(\text{p},\text{t})^{168}\text{Er}$. The third reaction is used to calibrate our data, i.e. match peaks in our spectra to corresponding energy levels. Obtaining the correct calibration is the focus of this work and is essential to the analysis

of ^{178}Hf and ^{174}Yb spectrums. After calibration we will study angular distributions of the ^{174}Yb and ^{178}Hf to identify their respective 0^+ excited states.

Experiment

In summer of 2019 data was collected at the Munich Q3D spectrograph. The targets in the collimator were composed of ^{168}Er , ^{178}Hf , and, ^{174}Yb . Each target was used for multiple runs with detector positions $\theta_L = 6^\circ, 10^\circ, 15^\circ, 20^\circ, 25^\circ, 30^\circ$ and magnetic settings $E_x = 580\text{ keV}, 1850\text{keV}, 2850\text{keV}$. Increasing the energy of the magnetic setting allows us to observe higher energy levels in our spectra. A one-dimensional histogram was created for each run with focal plane detector channel on the x-axis and particle counts on the y-axis. The histogram was recreated with only tritons counted on the y-axis.

Analysis

Before we are able to analyze ^{174}Yb and ^{178}Hf data we must calibrate ^{168}Er spectra for each angle and magnetic setting. Obtaining a calibration for ^{168}Er will allow us to match each channel in our spectrum to an energy level in a quadradic fashion. Using CERN Root [2], we fit peaks in the ^{168}Er spectra with a gaussian to estimate the centroid of each peak. A program for Root called SpectroPlot [3] predicts locations and energy of peaks. Using SpectroPlot (figure 1) and published labeled ^{168}Er spectra [4](figure 2) we match centroids of our peaks to energy levels.

At lower energies there are peaks in the ^{168}Er that are unaccounted for in both the SpectroPlot and previously labeled ^{168}Er spectra. We found our ^{168}Er targets was contaminated with ^{166}Er , ^{178}Hf , and ^{176}Hf . This is because hafnium was added to all targets as a reduction

agent [5]. To label the peaks of the contaminants in addition to the ^{168}Er we used SpectroPlot to predict their positions (figure 1).

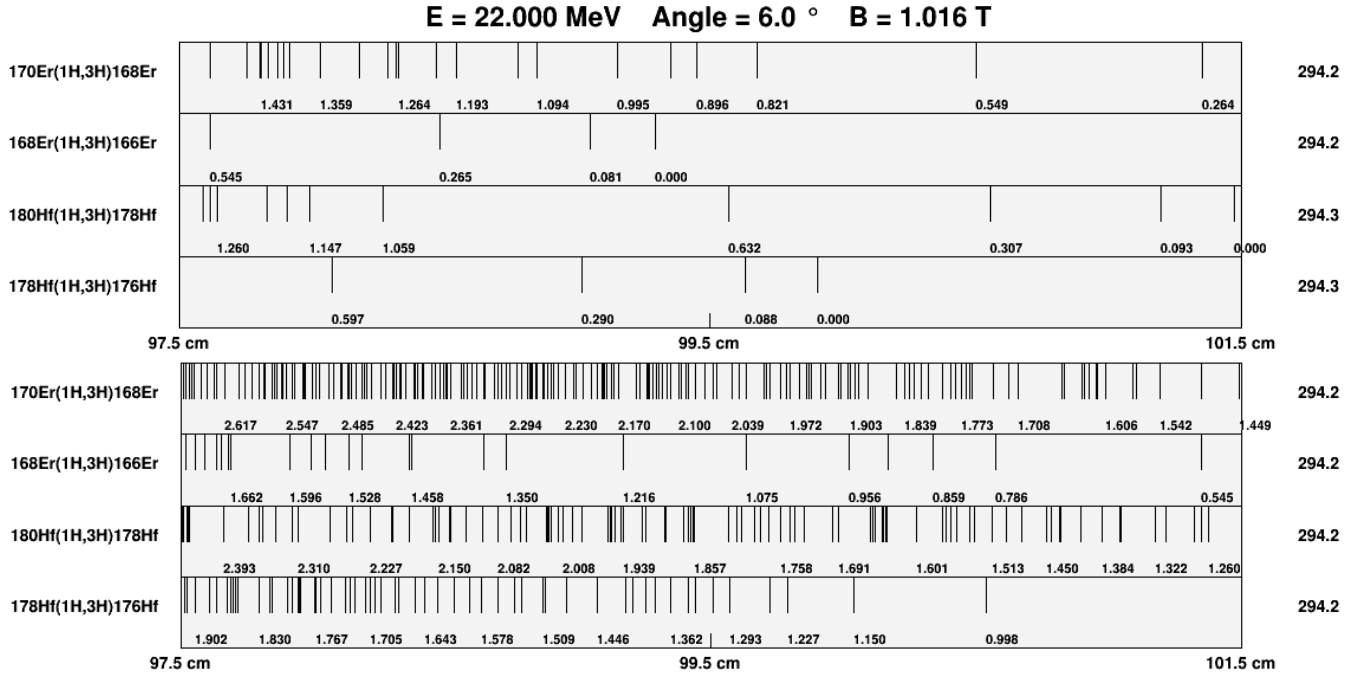


Figure 1: SpectroPlot for $\theta_L = 6^\circ$ $E_x = 580 \text{ keV}$ and $\theta_L = 6^\circ$ $E_x = 1850 \text{ keV}$

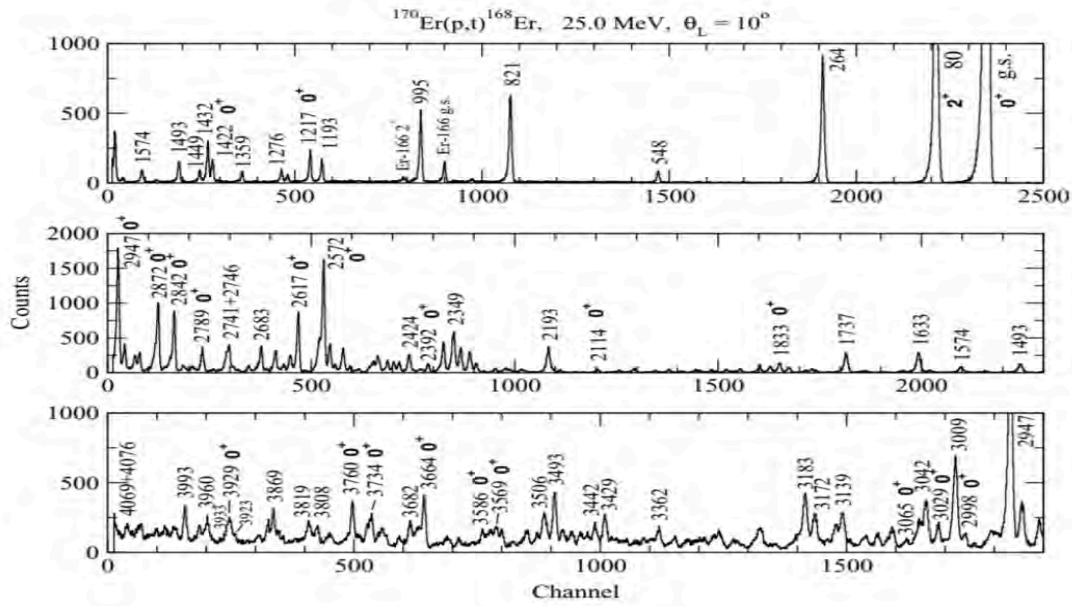


Figure 2: Labeled ^{168}Er spectra from published works.

Results

We successfully labeled our ^{168}Er spectra at angle $\theta_L = 6^\circ$ with magnetic settings $E_x = 580 \text{ keV}, 1850 \text{ keV}, 2850 \text{ keV}$ (figures 3, 4, and 5). To determine the calibration from our labeled spectra we enter peak energy and position data on a channel vs. energy scatter plot (figures 6 and 7). After the scatter plot is created, we fit the points with a quadratic function. The fit equation will calculate energy as a function of detector channel.

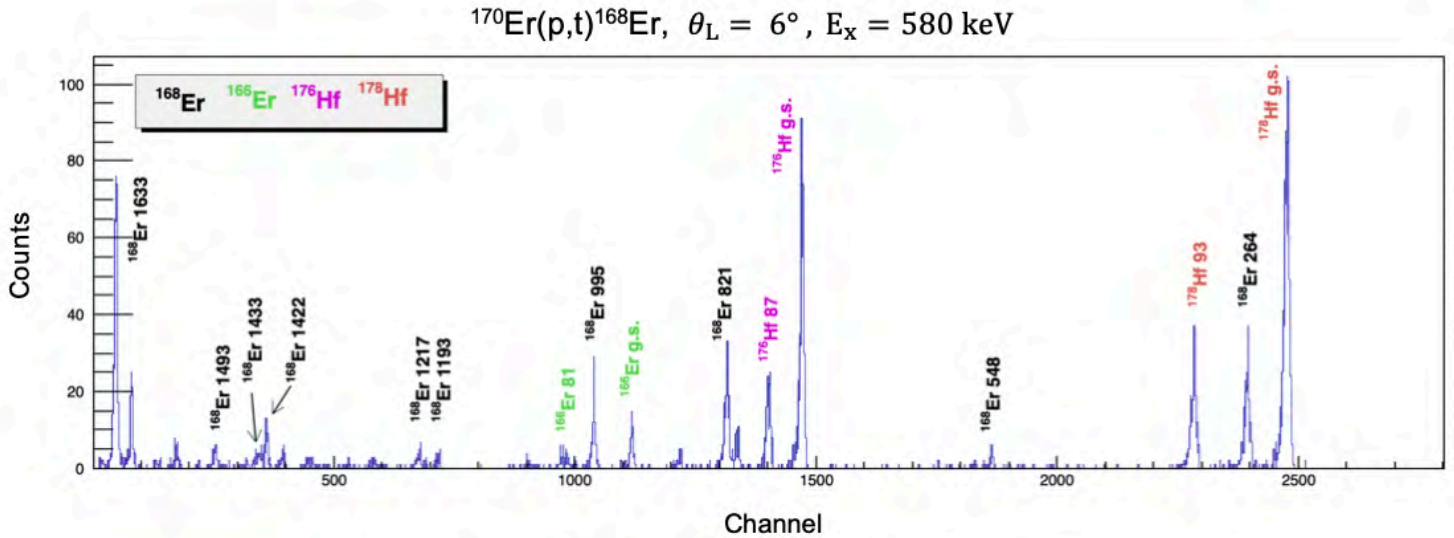


Figure 3: Labeled $^{170}\text{Er}(p,t)^{168}\text{Er}$ spectra, at the low magnetic setting 580 keV we see peaks from the ^{166}Er , ^{176}Hf , and ^{178}Hf .

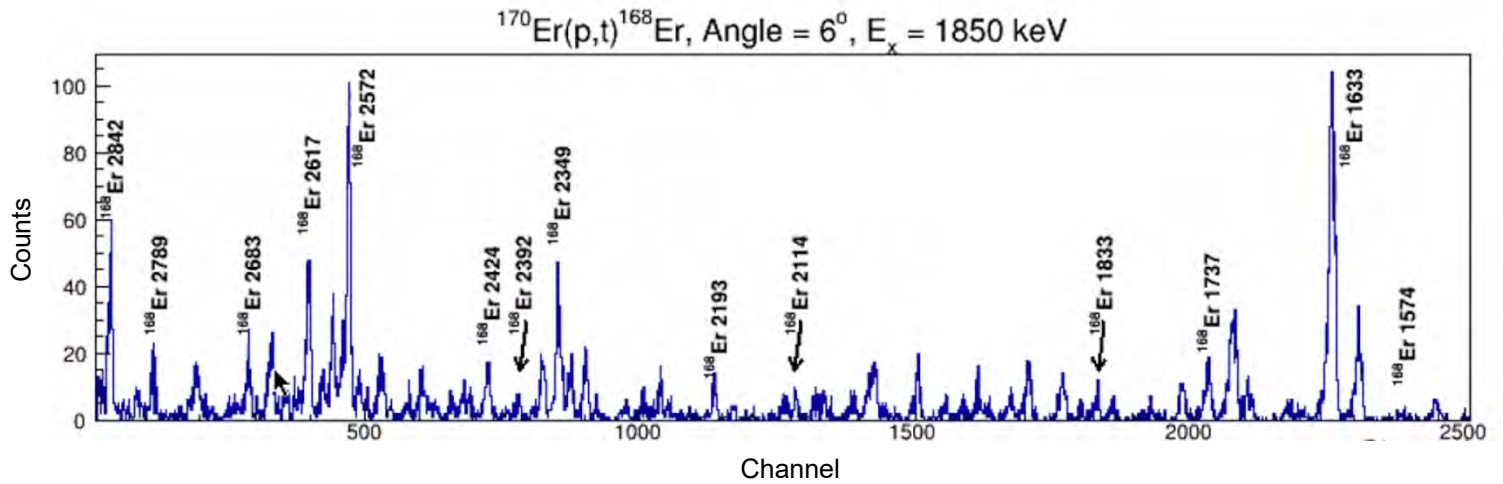


Figure 4: Labeled $^{170}\text{Er}(p,t)^{168}\text{Er}$ spectra with magnetic settings $E_x = 1850 \text{ keV}$.

$^{170}\text{Er}(p,t)^{168}\text{Er}$, Angle = 6° , $E_x = 2850 \text{ keV}$

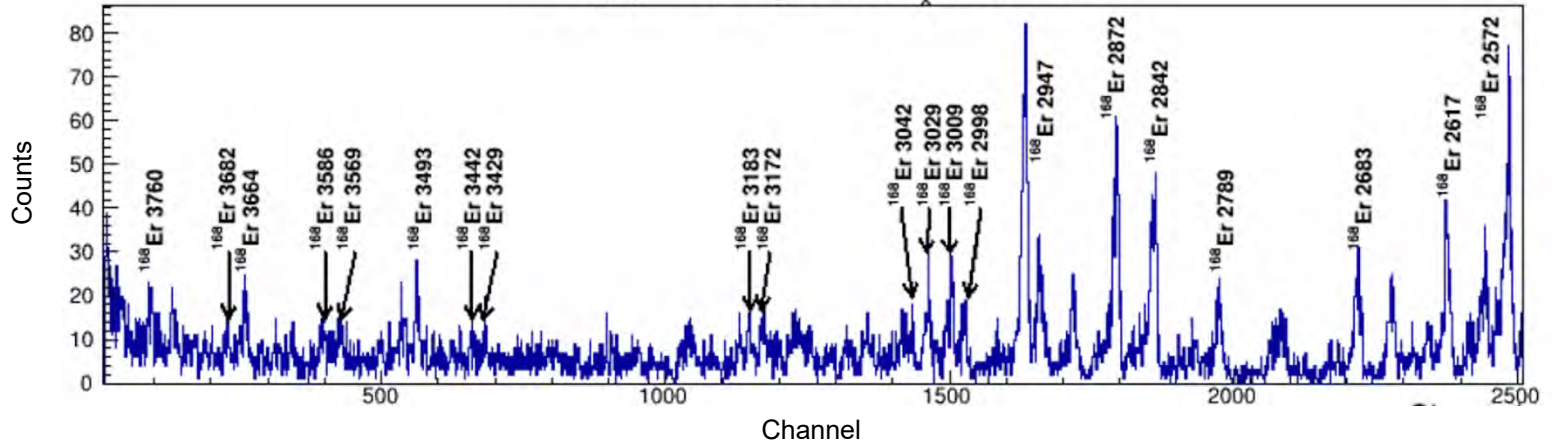


Figure 5: Labeled $^{170}\text{Er}(p,t)^{168}\text{Er}$ spectra with magnetic settings $E_x = 2850 \text{ keV}$.

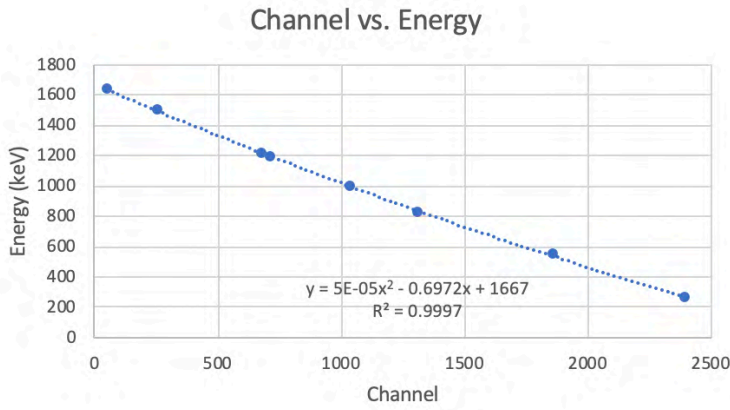


Figure 6: Channel vs. energy plot for $^{170}\text{Er}(p,t)^{168}\text{Er}$ with magnetic setting $E_x = 580 \text{ keV}$. The equation for the quadratic fit will calculate energy as a function of detector channel under the same position and magnetic setting conditions.

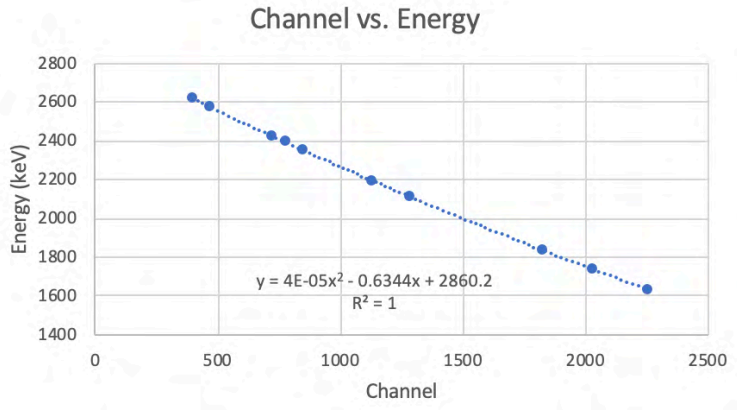


Figure 7: Channel vs. energy plot for $^{170}\text{Er}(p,t)^{168}\text{Er}$ with magnetic setting $E_x = 1850 \text{ keV}$. The equation for the quadratic fit will calculate energy as a function of detector channel under the same position and magnetic setting conditions.

Conclusion

Using published $^{170}\text{Er}(p,t)^{168}\text{Er}$ labeled spectra we calibrated our data for runs with detector position $\theta_L = 6^\circ$. Spectra from detector positions $\theta_L = 10^\circ, 15^\circ, 20^\circ, 25^\circ$, and 30° still must be calibrated. After all calibration is complete we will analyze $^{176}\text{Yb}(p,t)^{174}\text{Yb}$ and ^{180}Hf

(p,t)¹⁷⁸Hf data to identify their respective 0⁺ states. Determining 0⁺ states in rare earth nuclei is important in understand β-vibration.

References

- [1] Lesher, S. R. (2004). Low-lying collective excitations in nuclei: mixed-symmetry states in ^{96}Mo and 0^+ states in ^{158}Gd [Unpublished doctoral thesis]. University of Kentucky.
- [2] Fons Rademakers, Philippe Canal, Axel Naumann, Olivier Couet, Lorenzo Moneta, Vassil Vassilev, ... Raphael Isemann. (2019, August 23). root-project/root: v6.18/02 (Version v6-18-02). Zenodo. <http://doi.org/10.5281/zenodo.3895860>
- [3] Adsley, P. SpectoPlot/root: v6.18/02 (Version v6-18-02). Zenodo. <http://doi.org/10.5281/zenodo.3895860>
- [4] Bucurescu, D., Graw G., Hertenberger R., Wirth, H-F., Lo Iudice, N., Sushkov, A. V., Yu. Shirikova, N., Sun, Y., Faestermann, T., Krućken, R., Mahgoub, M., Jolie, J., von Brentano, P., Braun, N., Heinze, S., Moeller, O., Mücher, D., Scholl, C., Casten R.F., & Meyer D.A. High-resolution study of 0^+ and 2^+ excitations in ^{168}Er with the (p, t) reaction. *Phys. Rev. C* **73**, 064309. <https://doi.org/10.1103/PhysRevC.73.064309>
- [5] https://physics.nd.edu/assets/299393/book_final_part_1.pdf

Modeling STARLiTeR detector array with Geant4

Cassidy Favorite

2020 NSF/REU Program, Department of Physics, University of Notre Dame

Dr. Anna Simon

Department of Physics, University of Notre Dame

(Dated: August 6, 2020)

Abstract

γ -ray detectors are versatile tools for low energy nuclear and astrophysics. Modeling these detector arrays provides clearer understanding of their efficiencies, a serious limiting factor of surrogate measurements of cross sections. The Silicone Telescope Array for Reaction Studies (STARS) consists of silicone detectors used for particle identification. The Livermore Berkeley Array for Collaborative Experiments (LiBerACE) is an array of 6 Compton-suppressed high-purity germanium Clover γ -ray detectors. This STARLiTeR array is housed at the Cyclotron Lab at Texas A&M University. To determine efficiency of the STARLiTeR array, a Geant4 simulation was constructed and used to compare simulation data to experimental data of γ -spectra for ^{60}Co and ^{137}Cs . Efficiencies of a single detector from various positions around the chamber as well as efficiencies of the 6-detector array will be presented.

I. INTRODUCTION

Neutron capture cross sections are an important concept with applications in several fields, such as nuclear and astrophysics. However, direct measurements of these cross sections can be very difficult to obtain, specifically in nuclei with very short half lives. These cross sections can be inferred indirectly in surrogate reactions by using γ -ray detectors focused on a target and using the resulting gamma ray probabilities in combination with knowledge of nuclear structure [1].

γ -rays can interact with matter in three main ways: photoelectric absorption, Compton scattering, and pair production. For this project, we are most interested in photoelectric absorption and Compton scattering. In photoelectric absorption, a γ -ray gives up all its energy. The γ -ray does this by using some energy to break electron bonds and the rest is transferred to the freed electron as kinetic energy. The resulting pulses from photoelectric absorption fall in the photopeak as seen on Figure 1. In Compton scattering, the γ -ray loses part of its energy colliding with an free or loosely bond electron, transfers some energy to that electron as kinetic energy, and scatters out. In this case, only part of the γ -ray's energy is absorbed. When a γ -ray deposits the full energy it can deposit during Compton scattering, this creates a Compton edge that can be seen in Figure 1 [1].

A Clover detector is a gamma-ray detector that is composed of four high purity germanium crystals arranged as a four-leaf clover. The crystal arrangement can be seen in Figure

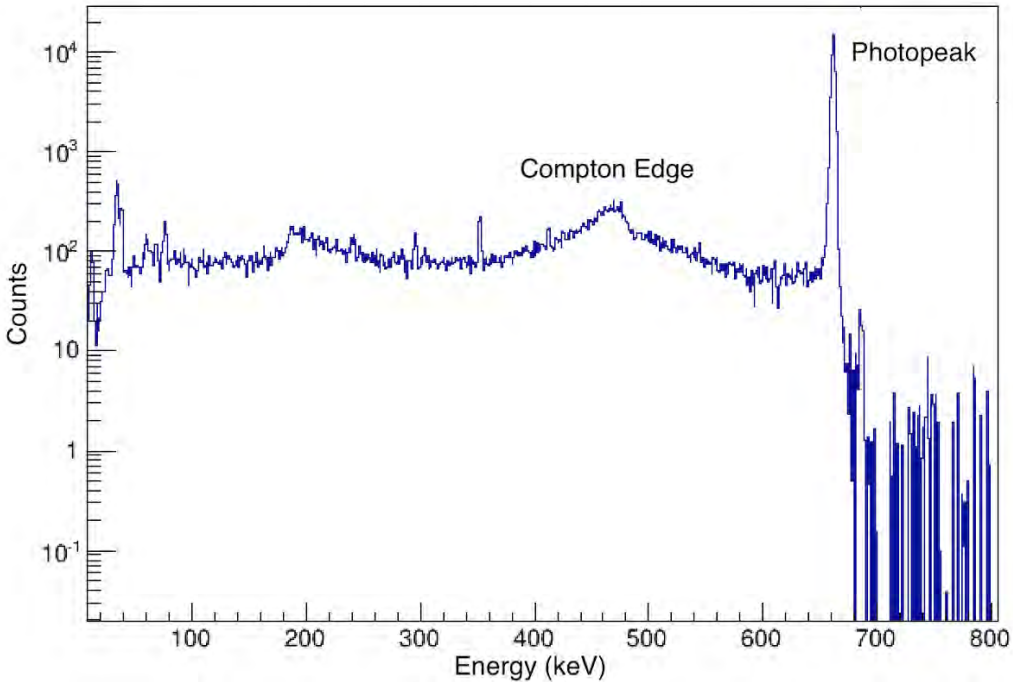


FIG. 1: Energy spectrum of ^{137}Cs measured by a germanium clover detector.

2. STARLiTeR is a Clover detector array used to study gamma ray emission housed at Texas A&M University Cyclotron Institute. The STARLiTeR array consists of six Compton suppressed Clover detectors arranged on the same plane in a circle around the target chamber. A cross section of the array can also be seen in Figure 2.

In this project, the main goal was to build a simulation in Geant4 of the Clover detector to better understand how the detectors worked and the efficiency of this setup. Using this software, a code was developed which simulated the target chamber and Clover detector. However, the design details of the Clover detector are considered proprietary and therefore were only vaguely known. The goal of this project was to use the simulation and data received to compare to actual data taken at Texas A&M to determine the structure of the detector. We also wanted to study how different components of the detector and target chamber affect the data and the efficiency of the array. With this simulation, we were also able to measure the efficiency of a single detector placed at various positions and angles around the target chamber.

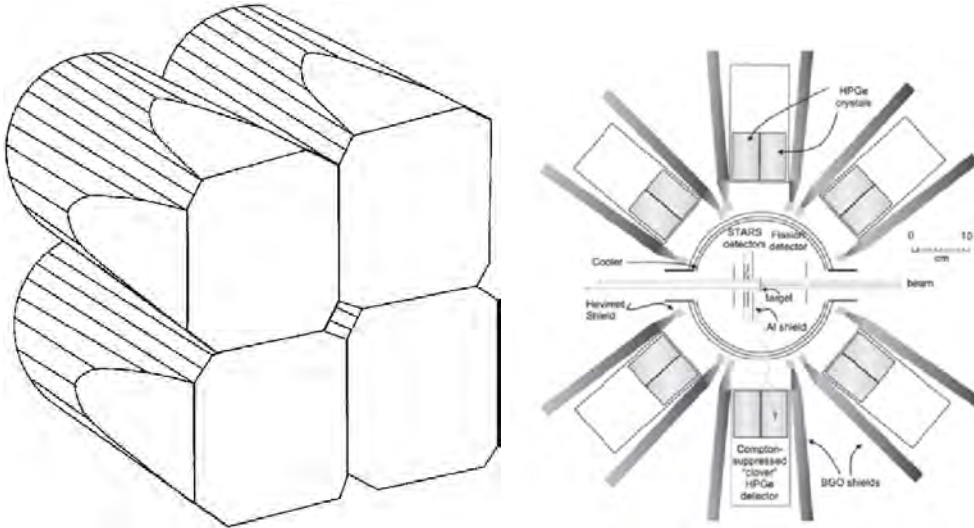


FIG. 2: Left: Schematic of the germanium crystals in the clover detector [2]. Right: This is a cross section of the STARLiTeR array configuration [3].

II. MATERIALS & METHODS

In this project, Geant4 was used to simulate the STARLiTeR detector array. Geant4 is a Monte Carlo program for the transport of radiation through matter. Geant4 works through a combination of random numbers and estimates of what will happen to the particle based on nuclear physics processes. In order to do this, the materials in the simulation and the energies of the gamma rays must be specified.

To make shapes in Geant4, first the materials being used must be defined starting with defining all elements used in the simulation. For this project, the elements defined were hydrogen, oxygen, nitrogen, argon, aluminum, germanium, manganese, silicon, chromium, nickel, iron, and copper. After defining the elements, materials were created using the defined elements. For this experiment, the materials defined were air, germanium crystals, aluminum, stainless steel, and copper.

Once all the materials were defined, the geometries of the room, the target chamber, and the detector were created next. The room must be created as a large space where all other shapes can be placed. The placements and sizes of all other shapes must fit into the defined room.

To create a simple shape, two options are G4Box* or G4Tubs*. G4Box* creates a box and G4Tubs* creates a cylinder. After defining the variables necessary for these commands, the

volume is created using the command G4LogicalVolume*. This command defines properties of the volume. With this command, the shape is selected, the material of the shape is defined, and the shape is given a name. Finally, the volumes are assigned a physical volume using the command G4VPhysicalVolume*. For the physical volume, the logical volume is selected, it is given a rotation, a placement in the volume of the room, and assigned a new name.

More complex shapes than just boxes and cylinders were needed to simulate the detector and target chamber. To accomplish these more complex figures, there are two commands that were used - G4UnionSolid* and G4SubtractionSolid*. These commands allow for the union or subtraction of any two defined shapes. These commands can be used in conjunction until the desired shape is achieved. Then again, the shape is assigned a logical and physical volume and placed in the simulation.

To build the simulation, measurements from technical drawings of both a Clover detector and the target chamber used in the STARLiTeR array were used for reference. These geometries were created and positioned in the simulation. The information pertaining to the inside details of the Clover detector is proprietary and therefore not wholly known. This includes the exact shape and size of the 4 germanium crystals as well as their exact arrangement, and the design of the cooling finger. These components were considered to be the necessary details for this simulation, any other interior components of the detectors such as wiring or other electronics were determined to be unnecessary as they did not interact with the gamma rays. The measurements used for the original design of the elements were based off of Professor Anna Simon's experience with these elements, correspondences pertaining to their measurements, and were tested through guess and check comparisons of experimental data.

The basic elements of the setup included in the simulation are the target chamber and the Clover detector. A single detector was first designed and tested before comparing to tests of the six detector array. The target chamber is an aluminum cylinder of diameter 9.875 inches with two smaller cylinders on either side centered about 2.4 inches from the top. There are a bottom and upper lid. Any further inner details for this chamber were considered unnecessary to simulate and were not included. Figure 3 shows an image of the completed target chamber in the simulation. The independent elements of the target chamber were designed and placed together to be controlled as one object using the G4UnionSolid* command.

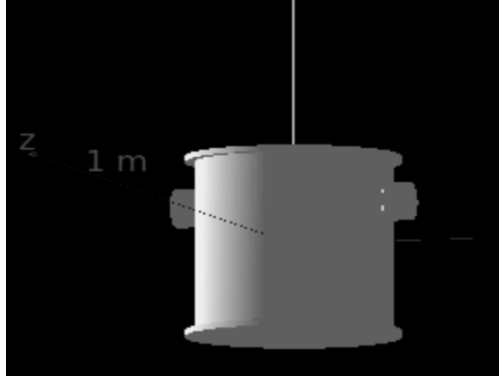


FIG. 3: This is an image of the target chamber that was simulated. The chamber is 9.250 inches tall with a diameter of 9.875 inches. The cylinders on the side have a diameter of 2.0 inches and are centered about 2.4 inches from the top of the chamber. The entire chamber is made of aluminum of thickness 0.4 centimeters.

The detector was a more complex geometry than the target chamber. The chamber is made of seven boxes, the front four with rounded corners. The crystals are housed in the very front box of the machine, set about 10 mm back from the front and attached in a way that only a small portion in the front and back of each crystals is touching some wiring which connects the crystals to the machine and keeps them in place. The sides of the crystals do not touch the sides of the box housing them. The other boxes of the detector were constructed to their correct size and volume but the interior details were considered unnecessary to simulate except for the cold finger.

The cold finger runs from the very last box of the detector to the crystals. The exact shape and size of the cold finger were unknown and different arrangements were tried. We suspect the cold finger is made of copper and is a cylinder of a diameter of 1 cm running through the detector and meeting with a thin disk also made of copper which touches the back of all four crystals. The copper is cooled to about 0° Celsius. The cold finger was considered to be an essential part of the design because the detector works at a very high resolution and cooling the crystals reduces noise in the spectra. The germanium crystals have free electrons in the lattice. By cooling the crystals, we can reduce noise caused by thermally excited electrons. The four crystals and the cooling technology can be seen in Figure 4.

The detector is 748 cm in length total. The outer casings are all made of 1 cm thick

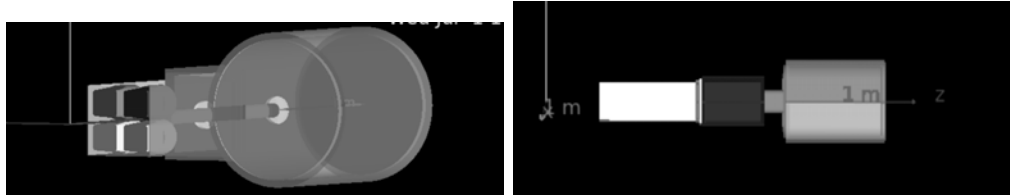


FIG. 4: Left: Schematic of the germanium crystals in the clover detector. Right: This is a cross section of the STARLiTeR array configuration.

stainless steel, except the the front box which holds the crystals. This front box is made of aluminum and is only about 1 mm thick. The inner details other than the cooling finger were not designed in this simulation because nothing else touches the crystals and everything falls behind the crystals. Therefore, those pieces could not block gamma rays before entering the crystal and they are not volumes that deposited energy is recorded from. Extra interior details do not have an effect on how much energy is deposited in the crystals. Images of the detector and it's components can be seen in Figures 4.

The crystals themselves are cylinders with a radius of 25 mm and are 40 mm long. They are shaved on the sides to better fit together in the square nozzle. They are touching on their sides.

There are two types of volumes in Geant4 - active and passive. A passive volume is a volume in which energies from particles are not deposited or measured. This included most elements of the design: the entire target chamber, the outside of the detector, and the cold finger. In an active volume in Geant4, the energies deposited by the γ -rays are recorded and measured. In this project, this was only the four germanium crystals.

III. RESULTS & DISCUSSION

The ROOT data analysis software was used to compare the experimental data to our simulation data. The total energies deposited in each crystal was summed in ROOT and plotted as a histogram showing the number of events which recorded a given energy in the crystals. This created a graph of the γ spectra. In this project, we focused on γ spectra from ^{137}Cs and ^{60}Co . ^{137}Cs emits one γ ray at energy 0.6614 MeV and ^{60}Co emits two rays at energies 1.1715 and 1.3316 MeV. The spectra created from the simulation was compared to experimental data.

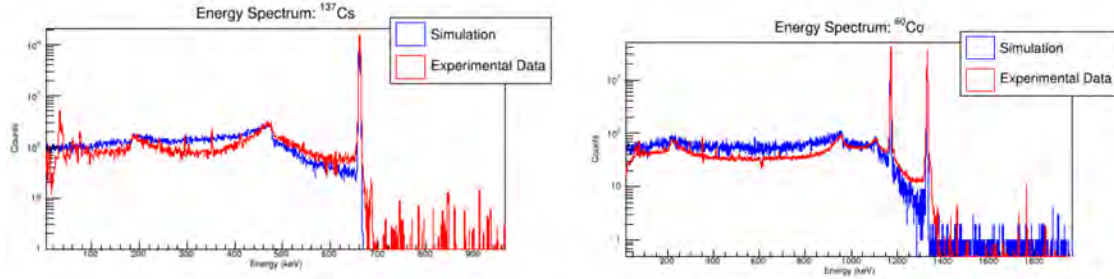


FIG. 5: Left: The experimental and simulated γ spectras of ^{137}Cs after final design. Right: The experimental and simulated γ spectras of ^{60}Co after final design.

Figure 5 shows the energy spectra simulated for ^{137}Cs and ^{60}Co after the simulation design was finalized. We found that many of the internal design details did not have a significant effect on the resulting energy spectra. The size and shape of the cold finger, the thickness of the aluminum casing around the crystals all created only minimal changes. The radius of the crystals and the thickness of the dead layer had the greatest effect. Each crystal had an thin, inactive layer in the front and back of the crystal caused by the mechanisms which hold the crystal in place. This is referred to as the dead layer.

After the design of the simulation was finalized, the efficiency of a single detector was tested at various positions around the target chamber as well as the efficiency of the six detector STARLiTeR array up to 10 MeV. The single detector was tested for a γ -ray energy of 1 MeV at increasing distances away along the z-axis from the target chamber, at increasing sideways distances along the x-axis away from the chamber, and offset at increasing angles from the target chamber. The resulting graphs are shown in Figure 6.

The efficiencies were calculated by running 1 million events of a single energy through the simulation, then taking an integral of the resulting photopeak within a 5σ range to determine how many events the detector captured. This number was then divided by the total 1 million events and multiplied by 100 to determine a percent efficiency.

First, the single detector was tested at various points around the target chamber: offset along the x-axis, angular offset, and at various distances away from the chamber. The results shown in Figure 6 illustrate that even just a slight change in position of the detector can lead to a much lower efficiency in the reading. This shows the importance when placing the detector. The detector is completely detached from the target chamber and it is imperative that it is placed directly in front of the chamber as close as possible to get the best readings.

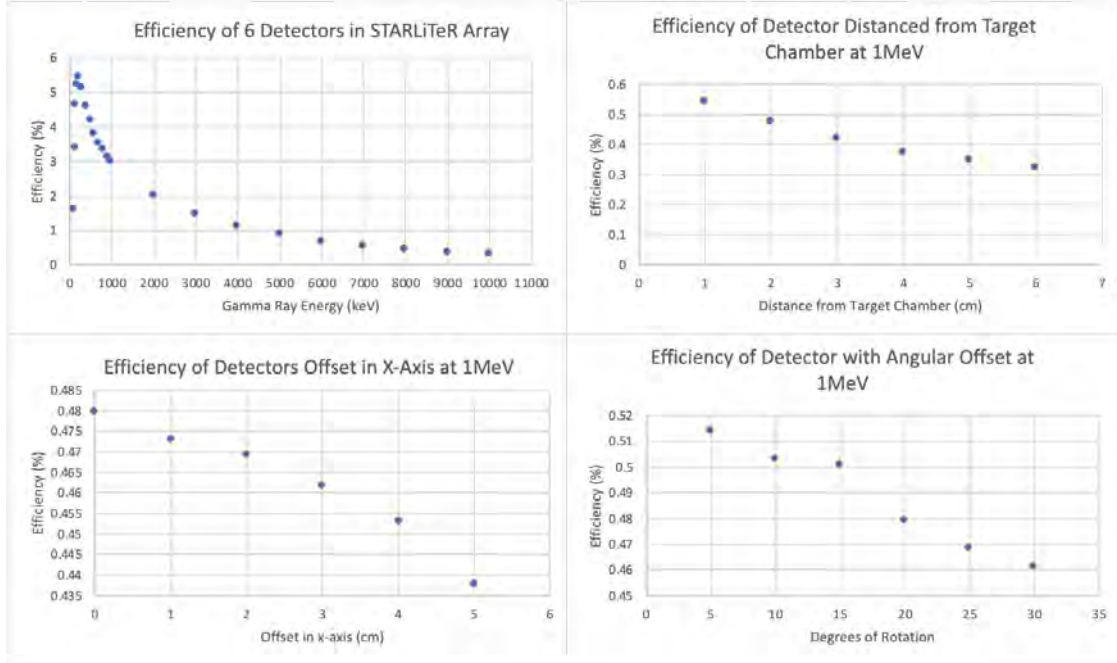


FIG. 6: Graphs of efficiencies of the detector arrangement and single detector placed in various positions around the chamber for a γ -ray energy of 1MeV.

Lastly, the six detector STARLiTeR array was tested at varying energies up to 10 MeV. The array had the greatest efficiency around 200 keV with an efficiency of about 5.4%. Energies below this amount quickly fall to zero. This is due to the fact that γ -rays with energy this low may not have enough energy to even reach the crystal, instead they are stopped by materials of the casing or the target chamber. Energies above 200 keV slowly decrease because these higher energies are more likely to scatter out of the crystal before depositing all their energy or pair producing.

IV. CONCLUSION

In this project, a computer simulation of a Clover detector and that STARLiTeR detector array was created in Geant4. It is much easier to create slight changes in a program to find the most effective distances and arrangements than testing them each in a lab setting which can be costly and time consuming. This simulation helped to better our understanding of the design and efficiency of the Clover detector, as well as the efficiency of the STARLiTeR array. We found that any slight misplacement of a single γ detector significantly reduces

the efficiency of that detector. We also found efficiency of the STARLiTeR arrange to be highest at about 200keV, where efficiency is about 5.4%. This simulation can be used test other possible detector arrangements to improve the efficiency and to design future experiments in nuclear astrophysics.

ACKNOWLEDGMENTS

I would like to thank my advisor, Dr. Anna Simon, the REU program coordinator, Dr. Umesh Garg, and the entire University of Notre Dame for working hard to continue the success of this program and support us students, especially in these challenging times. I would also like to thank Ryan Buechele, who worked on this project with me throughout the summer and Orlando Gomez, for proofreading and providing feedback of this paper.

- [1] G. Nelson and D. Reilly, Gamma ray interactions with matter, in *Passive Nondestructive Assay of Nuclear Materials*, edited by D. Reilly, N. Ensslin, and H. Smith, Jr. (Office of Nuclear Regulatory Research U.S. Nuclear Regulatory Commission, NuREG/cR-5550 LA-UR-90-732, Washington, DC, 1991) Chap. 2, p. 27.
- [2] I.-Y. Lee, M. Deleplanque, and K. Vetter, Developments in large gamma-ray detector arrays, Reports on Progress in Physics **66**, 1095 (2003).
- [3] S. Lesher, L. Phair, D. Bernstein, J. Burke, J. Church, P. Fallon, J. Gibelin, N. Scielzo, and M. Wiedeking, Stars/liberace: Segmented silicon and high-purity germanium detectors arrays for low-energy nuclear reaction and structure studies, Nuclear Instruments and Methods in Physics Research Section A: Accelerators, Spectrometers, Detectors and Associated Equipment **621**, 286 (2010).
- [4] R. Hughes, J. Burke, R. Casperson, S. Ota, S. Fisher, J. Parker, C. Beausang, M. Dag, P. Humby, J. Koglin, E. McCleskey, A. McIntosh, A. Saastamoinen, A. Tamashiro, E. Wilson, and T. Wu, The hyperion particle- γ detector array, Nuclear Instruments and Methods in Physics Research Section A: Accelerators, Spectrometers, Detectors and Associated Equipment **856**, 47 (2017).

The Calculated and Measured Bend Consistency

Yusen Feng

2020 NSF/ REU Program

Physics Department, University of Notre Dame

Advisors:

Kevin Lannon, Michael Hildreth

Abstract

The world's largest particle accelerator, the Large Hadron Collider (LHC) will meet its High Luminosity upgrade by 2027 to make the simultaneous collided particles increased about 10 times. The Track Trigger will serve as the filter system to select only the interesting data to process to make sure the efficiency of CMS as the detector. The measurement of the consistency of from-experiment bend and from-calculation bend is a useful indicator of the efficiency of rejecting fake tracks. After carrying that consistency check, we got the Gaussian distribution of calculated bend to measured bend.

1. Introduction

LHC(Large Hadron Collider) is the energy-largest high energy particle accelerator in the world. The LHC consists of a 27-kilometer ring of superconducting magnets with many structures accelerating the particles along the way. There are two beams of protons bumping together with extreme high energy in the speed of near light. Due to a series of upgrading of LHC (High Luminosity LHC) [1], the rate that generates high energy particles will be about ten times as the current collider. Which makes the pace of finding new particles that are rather faster.

The detector should be improved so as the generator. The CMS (Compact Muon Solenoid) is one of the four main detectors attached to the LHC. The CMS is a particle detector and high-performance system designed to see a wide range of particles produced in high energy collisions in the LHC, and it is particularly good for detecting and measuring muons. As a

matter of fact, the detector will not save all the instant information from the generator because there will be another new particle every 25 ns. Thus, there is a filter system which selects only some interesting information from amounts of data. A very important part of the upgrade of CMS is the Track Trigger system which serves as an extraordinary alarm system to report the particles whose kinetic energy is high enough to make something beyond changing direction in the collision.

The layers of the CMS detector are the tracker, electromagnetic calorimeter, hadronic calorimeter, superconducting solenoid and muon chamber. My research only cares about the tracker part which serves drawing the trajectories of colliding particles. The tracker is made of 6 barrel layers and 5 end-cap layers and the particles which go through it will leave some marks on each layer one by one. To track each particle's trajectory, a high intensity magnetic field is applied to make those particles bend. The trajectory of each particle is divided into many parts because of the layers are separated in that plane. Picking up those broken partial trajectories (also called stubs) to form the complete one is the way the CMS reduced data size. Note that the whole trajectories must have some cross points with the location of particular detectors in the barrel part of CMS. We can use that information in different layers to infer the whole trajectories to be like to save memory of detector and save time.

The detecting algorithms have been upgraded for many times by the team of CERN. Systematically learning the way that the partial trajectories of collided particles are measured is an important first step in high energy physics. I am in this program to use the ‘bend’ value that describe the bending level of trajectory to compare the consistency of experiment and theoretical analysis. In fact, the upgrade of LHC has not been done, so there are not even any

real experiments carried out with the Track Trigger system. But, we can use simulation algorithms to generate particles that are in accordance with physical facts. Using the comparison can also serve as an example-analysis for understanding how the Track Trigger system works.

2. Methodology

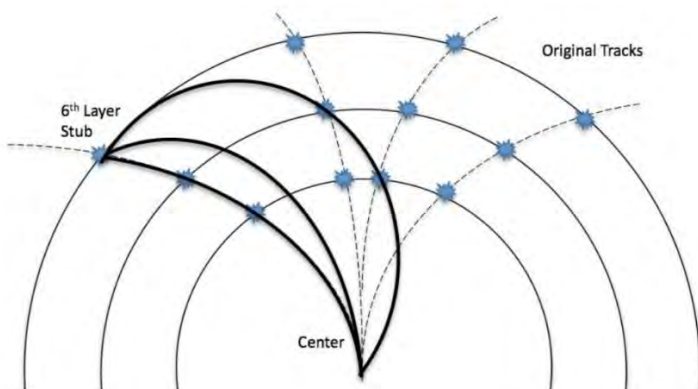


Figure 1 The illustration of tracks and layers' cross points (they are often called 'hits' which are in blue color) in barrel part, the figure was made in the former REU Students' paper [2]

When collisions are over, particles emerging from the collision first encounters the tracking system which is made up of silicon pixels and silicon strip detectors (which means that there are many small detectors to acquire enough spatial resolution). This accurately measures the positions of passing charged particles (often are called hits) to reconstruct their trajectories. The curvature of the path implies their momentum (particularly for muons). The particles flying out of the collisions have such high energies that it takes big distances to absorb them and vice versa.

The main coordinates we use in this analysis are r , ϕ and z . But the FPGAs in the detectors' firmware region collects the information of each hits' x and y location. So, in the program, we should convert it to polar coordinates:

$$r = \sqrt{x^2 + y^2} \quad \varphi = \arctan\left(\frac{y}{x}\right)$$

As we known, the reason why we want to store the information of hits is we want to reconstruct the whole trajectory. In that aspect, we can roughly think that the hits which carry the important value of the curvature are local tracks which are often called stubs.

Inside the CMS, particles with a charge q are accelerated in a 3.8 T magnetic field B . The Lorentz force experienced by the particle is given by:

$$m \frac{v^2}{\rho} = qvB$$

In both part of the first equation, cancel out the velocity and multiply the curvature radius, then left part is the expression of transverse momentum (The particle must have another momentum along the symmetry axis which functions at travel along the z axis):

$$p_T[\text{Gev}] = \rho[m] \times 1.602 \times 10^{-19} q [C] \times B \left[\text{kg} \frac{m}{s} \right] \times \left(\frac{1 \text{Gev}}{5.36 \times 10^{-19} \text{kg} \frac{m}{s}} \right) = 0.3qB\rho = 1.14q\rho$$

As seen in the *Figure 1*, the ϕ position of each hits are different. The horizontal distance between the first and second hit describes the particle's bend which is a value describing the curvature of the particle's trajectory. That value is called bend or stub width for short.

The bend value is measured in units of strips. Strips means that there are small individual detectors arranged into layers to build whole sensor. So, bend is just the number of horizontal individual detectors the particle passes. The relationship of values that can be measured and the geometry inside the CMS are explained in the *Figure 2*.

SW is the bend (also known as stub width), pitch is the width of the detector strips, Δr is the sensor spacing of modules perpendicular to the radial axis, r is the radial position of the layer, ρ is the distance from the event's vertex to the module or the curvature radius, and β is the angle between the z-axis and p .

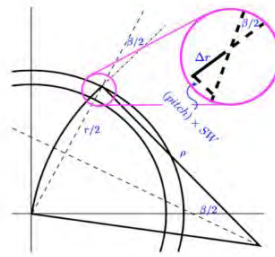


Figure 2, The relationship of measured values and the geometry inside the CMS, picture made by Kevin Lannon[3]

In fact, in the *Figure 2*, the pink circle zoom window, the Δr which means the difference of two layers' radius should be the dash line part in the right part of that window. But, still, the transverse distance which is calculated by $\text{pitch} \times SW$ is what is shown in that Figure. That's because the β which describe the deflection angle is too small, there are some subtle approximations. Below is the deduction of the calculation of SW in other measured values:

$$\tan \frac{\beta}{2} = \frac{\text{pitch} \times SW}{\Delta r} \quad \sin \frac{\beta}{2} = \frac{r}{2\rho}$$

We have the equation that $p_T = 1.14q\rho$, so we can get:

$$SW = \frac{\Delta r}{pitch \times \sqrt{(\frac{p_T}{0.57qr})^2 - 1}}$$

Considering the β value small, so as the $\frac{p_T}{0.57qr}$. With approximation, conclude that:

$$SW = \frac{\Delta r \times 0.57qr}{pitch \times p_T}$$

As said over and over again, we just care about those particles with high energy. In actual experiment, we use some techniques to split $p_T < 200MeV$. We get muons as our main simulation object, and the muons are the muons and antimuons aggregate. So, the charge can only be +1 or -1. The pitch is also not a static value, and with the radius of layer becomes larger the pitch goes even smaller to make more detectors.

When we generate both experiment values of bend and theoretical values, we can plot them to see if there are something are not in correspondence.

3. Results

The results are calculated by CMSSW_11_1_0_pre8 edition. There are two simulation experiments which each has 700 events and the entries of each experiment are about 1.3e07.

First, the stubs' location is presented in the way of 1D histograms.

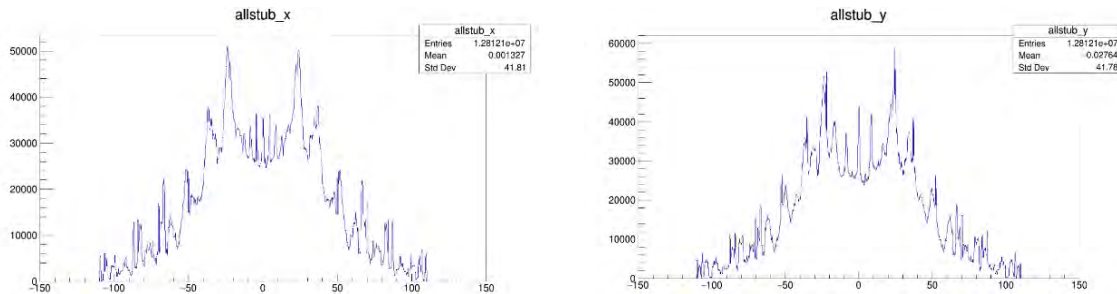


Figure 3, each stub's x, y positions

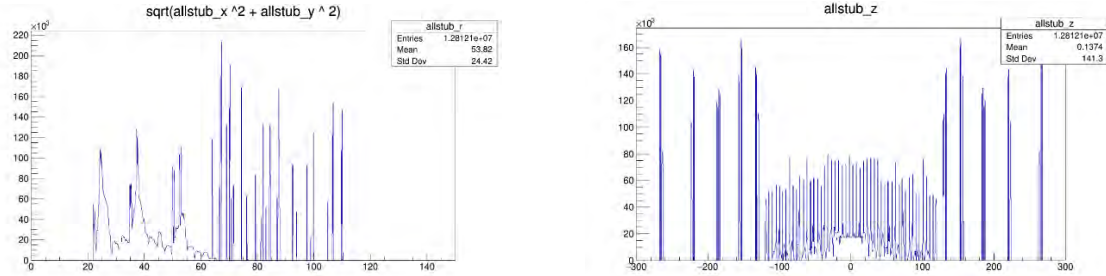


Figure 4, each stub's r , z positions

If we plot x vs y in one figure, we can know where the particles leave marks on the sensors in a plane, which will be easier for directly understood. Basically, there are two separated parts, the barrel part and end-cap part (also there exists an overlap part, but we do not care it much in this thesis). If we use the variable `allstub_isBarrel` to mark the difference, we can also generate the separated plots.

Of course, the r vs z plot together with the rotational symmetry will present the whole blueprint of the tracker. The z direction is almost symmetric because there are two beams of particles after collision flying in opposite directions.

My research is mainly about the barrel part which has 6 different layers. The barrel part's `x_vs_y` plots are overlapped, so draw them separately.

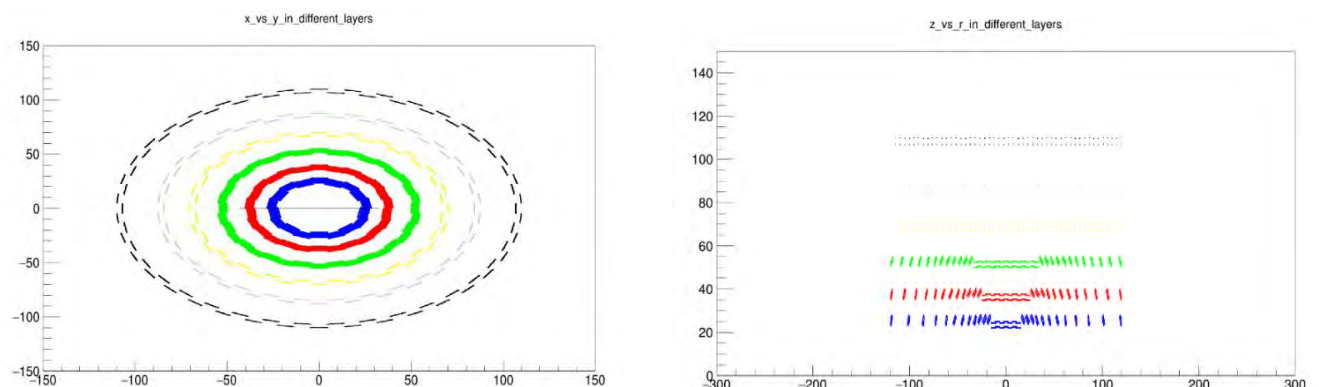


Figure 5 & 6, Each stub's x vs y with color distinguished layers (left) each stub's r vs z plot with color distinguished layers (right)

Till now, we have acquired all spatial information of each hits. The physics information of each hits is determined by other algorithms beyond the trigger part. Taking them as granted (as for the simulated particles, we just set their equations at the generating algorithms to get the exact value of them), we can use listed final equation to get that result.

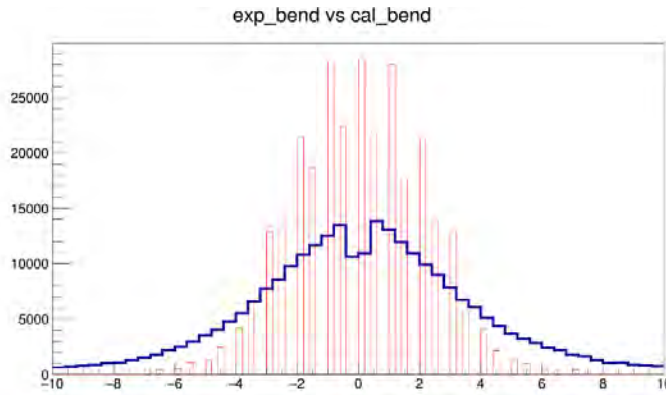


Figure 7, The result of calculated bend (red line) vs measured bend (blue line)

From Figure 7, we can find the blue line whose height is a bit shorter than the calculated bend. That's because the blue line which denotes the calculated bend should be continuous value while the red line which denotes the measured bend just are some discrete values due to the measuring precision. In general view, the blue curve is the Gaussian distribution of the red one which just makes sense, considering the properties of particles are simulated using Gaussian distribution.

Just like the other results which can be separated due to difference in layers, we can do this in the presentation of comparison result. Using the 2D histograms whose slop equals to +1 can be the criterion of consistency can lead to the direct understanding of the comparison. And under figures in different layers show good enough result of comparison check.

4. Conclusions

With the upgrade of HL-LHC will be completed by 2027, the algorithms of reconstructing tracks should also be systematically learned to fully understand its power. The main study focuses on the process of using the some measured spatial values and transverse momentum to get the bend value which is the ingredient of trajectory. The correspondence check of measured bend and calculated bend is of importance for next step in refusing fake tracks. After carrying the check, I get the calculated bends maintain the Gaussian distribution of the measured ones.

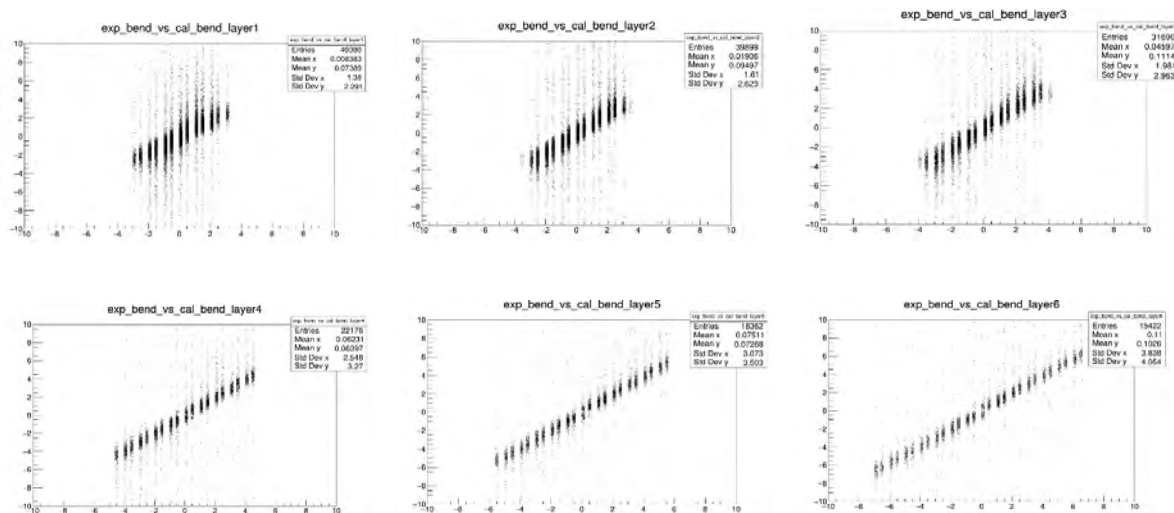


Figure 8 exp_bend vs cal_bend in different layers

References

- [1] CERN: Accelerating Science. High-luminosity lhc. <https://home.cern/science/accelerators/high-luminosity-lhc>, 2019.
- [2] R. Creager, M. Swift, K. Lannon, M. Hildreth. Analysis of a Potential Tracking Algorithm for the SLHC Upgrade, 2012.
- [3] K. Lannon. Using bend information in track finding. L1 Tracker, 2018

Understanding the primordial Lithium-7 problem in Big Bang Nucleosynthesis with Ordinary-Mirror neutron Oscillations

Shuaijie Li

*School of Science, Xi'an Jiaotong University,
Xi'an 710049, China*

2020 NSF/REU Program

Physics Department, University of Notre Dame

Advisor: Wanpeng Tan

*Department of Physics,
Joint Institute for Nuclear Astrophysics,
University of Notre Dame, IN 46556, USA*

ABSTRACT

During the big bang, the early universe was in a state with extraordinarily high density and temperature leading to the Big Bang Nucleosynthesis (BBN). In addition, the neutrons were unstable and protons were stable leading to a low n-to-p ratio in the early universe. Once the universe is cool enough, various elements in the early universe began to be produced via nuclear reactions. Due to lack of stable nuclei at mass = 5 and 8, only light particles are produced such as ^2H (deuterium), ^3He , ^4He , ^7Be and ^7Li . While most of elements of their predicted abundances are in agreement with observations but the discrepancy on the ^7Li abundance is about of a factor of three. The model of ordinary-mirror neutron oscillation seems hopeful to solve this persistent problem. This oscillation would lead to lower ^7Be production by lowering participating neutron's energy in the reactions, so there will be fewer ^7Li because of the fact that most of ^7Li came from decays of ^7Be . As a result, the abundance of ^7Li may decrease to the level which agrees with observations. After tracing the time when the oscillation happens and the original abundance of mirror neutron in the code, our computations give the expected results.

I. INTRODUCTION

Nowadays, big bang theory is considered as a basic and classical physics model to describe the development of the universe. The early universe was copious with kinds of light elements, which can be explained by Big Bang Nucleosynthesis (BBN). According to BBN, shortly after the big bang, the early universe was in a state with extraordinarily high density and temperature. In addition, the neutrons in the early universe were unstable although protons were stable, and the quantities of them were balanced at that time.

It is precisely due to the instability of neutrons that various elements in the early universe

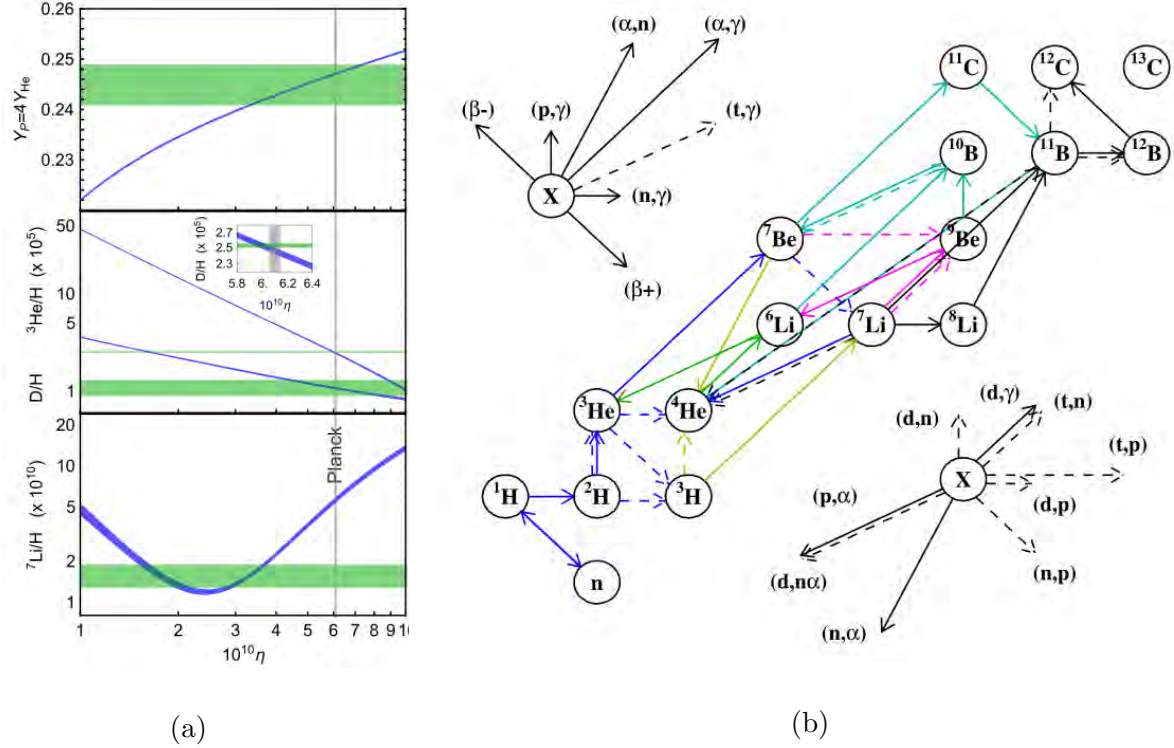


FIG. 1: (a) Calculated and observed abundances of light elements as function of baryon density. (b) Nuclear reactions in BBN. Both figures are taken from Ref. [2].

began to interact and produce nuclear reactions. The most basic reaction being between a neutron and a proton, which produces 2H (deuterium). All other reactions follow that reaction and other light particles (heavy particles are rare in the reactions) are produced such as 4He , 7Be and 7Li .

With the help of the primordial classical theory BBN, physicists can predict the abundances of the four important elements by computing or stimulating according to the theory. Three of the four elements of their predicted abundances are in agreement of the experimental observations. However, to their surprise, the predicted abundance of 7Li is as three times as that in observation. The results might accord with the abundance given in experimental observations. We anticipate that the abundance of 7Li could decrease and match the data.

As shown in Fig. 1a, η is baryon density. The green line is experimental observation results, and the blue one describes the predictions of the abundance of ^7Li which is nearly three times that of observations. Therefore, there is a need for fresh blood to be injected in the field to solve the longstanding ^7Li problem. In terms of that, the model about ordinary-mirror neutron oscillation seems hopeful to solve this persistent problem.

II. BIG BANG NUCLEOSYNTHESIS

As talked in Section I, when the universe is cool enough, all kinds of elements began to be produced by nuclear reactions. Due to lack of stable nuclei at mass=5 and 8, only light particles are produced such as ^2H , ^3He , ^4He , ^7Be and ^7Li . The network of nuclear reactions in BBN is shown as Fig. 1. The most important and basic nuclear reaction in BBN is the reaction between a neutron and a proton, shown as Equation (1).



According to Fig. 1, after $p(n,\gamma)^2\text{H}$ reaction, other particles can be produced through nuclear reactions followed by n-p reaction, such as $^2\text{H}(p,\gamma)^3\text{He}$, $^3\text{He}(d,p)^4\text{He}$, $^3\text{He}(\alpha,\gamma)^7\text{Be}$, $^7\text{Be}(n,p)^7\text{Li}$. The last nuclear reaction is shown as Equation (2).



Because of the truth that the protons were stable in the early universe while neutrons were unstable at that time, an overwhelming majority of particles in the early universe are protons. As the universe gradually cools, there are still plenty of protons in the universe. Once there were ^7Li produced through a series of nuclear reactions (Equation (2) is one of them), they will be captured by those protons through the reaction shown as Equation (3).



That's why there is very little ^7Li in the universe.

Through Equation (2) and (3), if we inject extra neutrons participating in those related nuclear reactions, more ^7Be will be destroyed through Equation (2), thus fewer ^7Be will be left. As for the abundance of ^7Li , for one thing, if more neutrons were added in reactions, after reaction (2) and (3), more ^7Li will be destroyed, thus fewer ^7Li will be left. For another, because there were fewer ^7Be left, fewer ^7Li can be produced through the decay of ^7Be . As a result, the abundance of ^7Li will decrease.

III. ORDINARY-MIRROR NEUTRON OSCILLATION

From the primordial BBN code (by A. Coc), the flow chart is shown as Fig. 2. The abundances of various elements are shown as Fig. 3. A mirror sector of the universe has long been conjectured since Lee and Yang published their work[1] on parity violation which won the Nobel Prize. This idea has just been fully developed into a new theoretical framework in a series of papers which explain a lot of unanswered puzzles. The celebrated Standard Model is naturally extended with a mirror sector of particles sharing the same 4-dimensional spacetime. The mirror particles are almost an exact copy of the ordinary ones participating in similar yet separate mirror interactions (i.e., mirror electromagnetic, weak, and strong forces). Nevertheless, both sectors share the same gravity, namely, the same stage of spacetime. The breakdown of mirror symmetry is so tiny (about one part out of one hundred trillion in mass splitting) but the effects are significant. Both tiny neutrino masses and dark energy (that dominates the Universe's energy budget) are originated from the mirror symmetry breaking. So are neutral particle oscillations, in particular, neutron ($n-n'$) and kaon ($K-K'$) oscillations that serve as the most important messengers between the two sectors. And $n-n'$ oscillations can solve the persistent ^7Li problem.

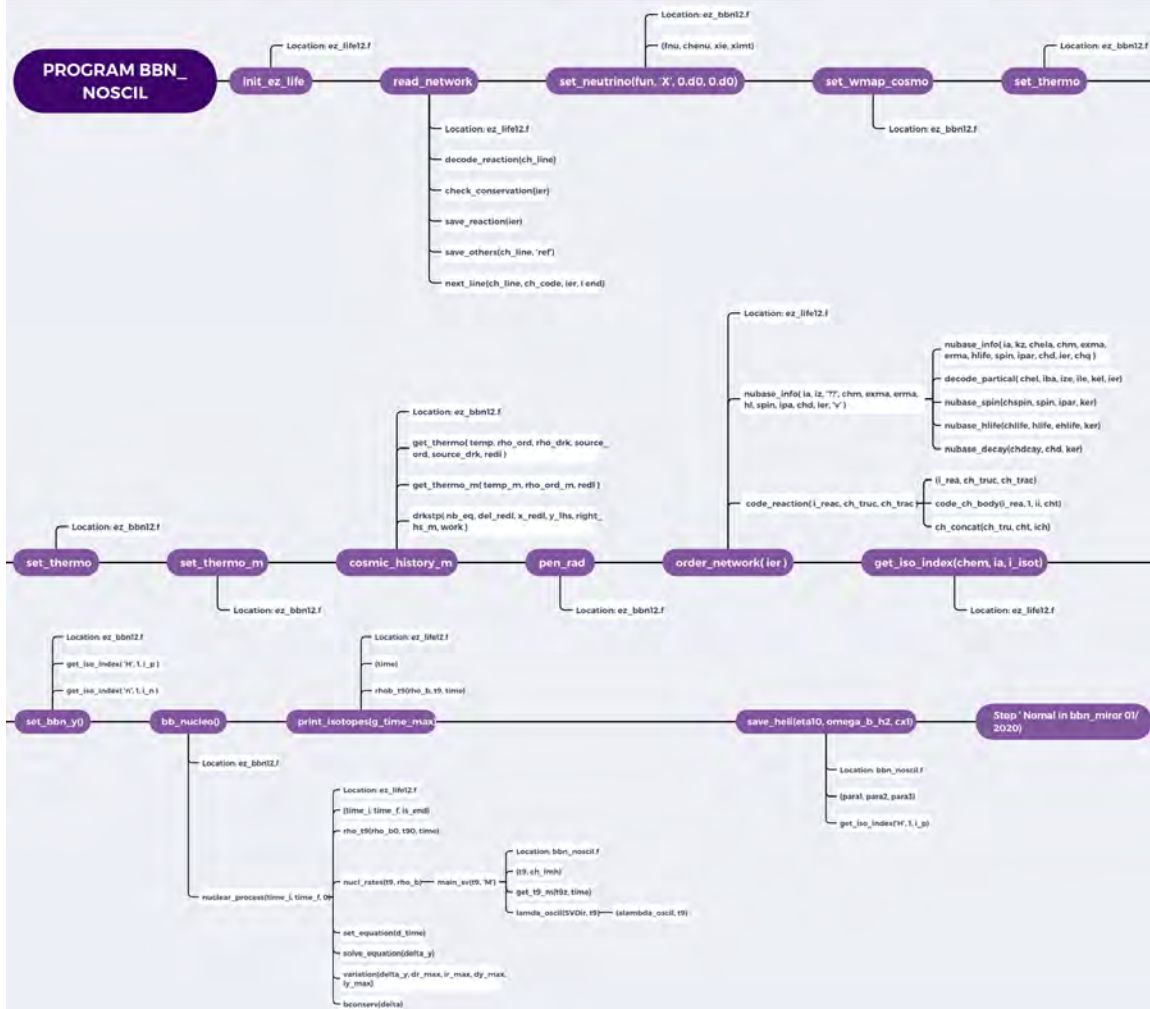


FIG. 2: The flow chart of the primordial BBN code

The broken mirror symmetry mentioned above will naturally lead to the oscillations of neutral particles due to a mass difference $\Delta_{nn'}$. We can find the probability of nonrelativistic n-n' oscillations in free space[3],

$$P_{nn'}(t) = \sin^2(2\theta)\sin^2\left(\frac{1}{2}\Delta_{nn'}t\right) \quad (4)$$

where θ is mixing angle, $\sin^2(2\theta)$ denotes the mixing strength, t is the propagation time, and $\Delta_{nn'} = m_n - m_{n'}$ is the mass difference. Note that such oscillations do not affect the stability of nuclei with bound neutrons owing to energy conservation. For n-n' oscillations, the mixing strength and the mass difference are two constants, i.e., $\sin^2(2\theta) = 2 \times 10^{-5}$,

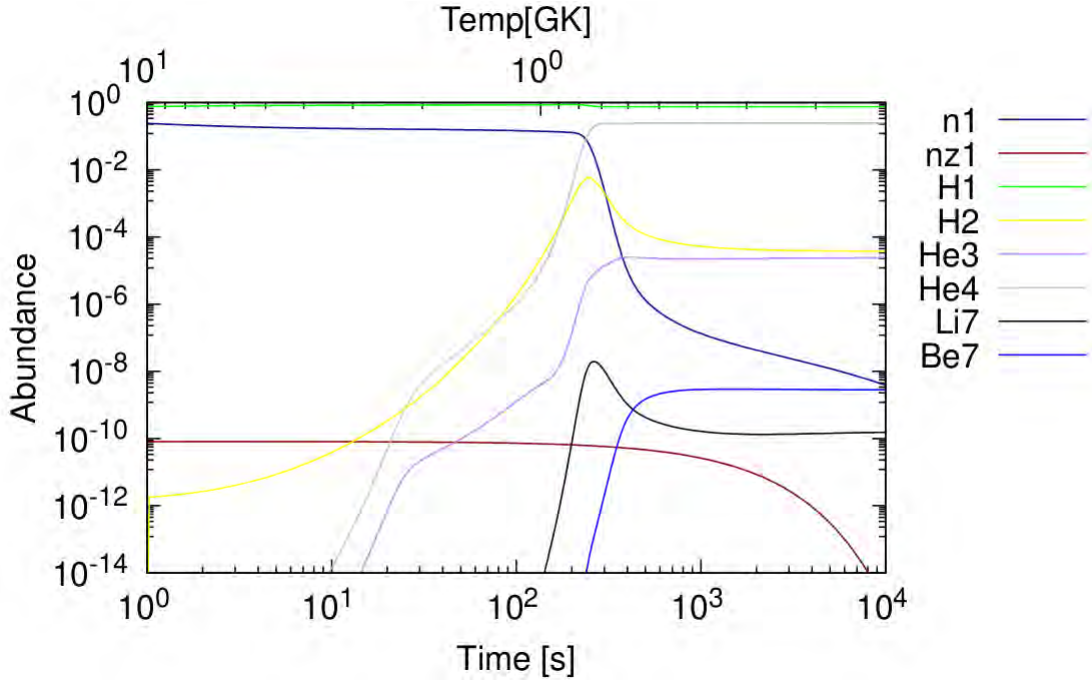


FIG. 3: Evolution of light elements abundances

$\Delta_{nn'} = 2 \times 10^{-6} eV$. The corresponding invisible decay branching ratio due to n-n' oscillations

is,

$$B_{inv} = \frac{1}{2} \sin^2(2\theta) \frac{(\Delta_{nn'} \tau)^2}{1 + (\Delta_{nn'} \tau)^2} \quad (5)$$

where τ is the neutron's mean lifetime.

Based on the known observational and experimental evidence, these large yet realistic estimates of the oscillation effects in the new mirror matter model may help motivate more experimental efforts in search of invisible decays of long-lived light neutral hadrons. New physics could be revealed in such experiments and it is also one of the promising laboratory approaches to test the unique predictions of the new mirror matter model.

IV. RESULTS

Considering the interactions between mirror matters and ordinary sectors, in order to add the whole n-n' oscillation model in the code, we firstly reset the temperature in BBN after a certain time, which was replaced from the temperature of ordinary matters to the weighted temperature of ordinary matters and mirror matters. The weighted ratio depends on that of the abundance of ordinary neutrons and mirror neutrons.

In addition, the set of time parameter can change automatically in a loop in FORTRAN. After finishing the reset of time parameter, we should consider another important parameter which have strong effects on the abundance of ^7Li , and that is the initial abundance of mirror neutrons. Similar to the reset of time parameter, we can also make the abundance of mirror neutrons change automatically in a FORTRAN loop. In the two loops mentioned above, we can get the complete results with all combined situations, which is recorded in a final data document. Specifically, the observations and predictions from A. Coc[2] and the computations in this work were given in Table. I.

TABLE I: Primordial abundances compared to observations

| | Observations[2] | Predictions[2] | This work |
|---|------------------------|-----------------------|------------------|
| Y_P | 0.2449 ± 0.0040 | 0.24709 ± 0.00017 | 0.24648 |
| $\text{D}/\text{H}(\times 10^{-5})$ | 2.527 ± 0.030 | 2.459 ± 0.036 | 3.929 |
| $^3\text{He}/\text{H}(\times 10^{-5})$ | $<1.1 \pm 0.2$ | 1.074 ± 0.026 | 1.217 |
| $^7\text{Li}/\text{H}(\times 10^{-10})$ | $1.58^{+0.35}_{-0.28}$ | 5.623 ± 0.247 | 1.571 |

In Table. I, we can see that there exits obvious difference between two results for $^7\text{Li}/\text{H}$, and D/H change a little as well (we think this change was tiny compared with that of the

value of ${}^7\text{Li}/\text{H}$). For the other two elements, Y_P (known as ${}^4\text{He}/\text{H}$) and ${}^3\text{He}/\text{H}$, nearly change nothing. And our results are in good agreement with the observed values.

V. CONCLUSIONS

According to the mirror-matter model, there will be neutron oscillations produced by the interactions between ordinary matters and mirror matters. After adding the ordinary-mirror neutron oscillation model in the primordial BBN code, the long lasting ${}^7\text{Li}$ problem can be solved perfectly. The oscillation between ordinary neutrons and mirror neutrons would lead to more destruction of ${}^7\text{Be}$ by adding more neutrons, which will cause fewer ${}^7\text{Be}$ left. Thus the abundance of ${}^7\text{Li}$ will decrease to the observational value because of the decay of ${}^7\text{Be}$.

ACKNOWLEDGMENTS

It is my great honor to be a member of this Summer 2020 REU Program. I learned a lot and spent a wonderful summer time working with outstanding professors and researcher in Notre Dame and other REU members from all over the world. I would like to thank the University of Notre Dame for organizing the program, so that many students including me who aims to contribute themselves to physics field can have the precious opportunity to work with professors in Notre Dame and do a research project with them together. Also, I should thank Dr. Umesh Garg, Ms. Lori Fuson and all professors of REU courses, Mr. Sushrut Ghonge, Mr. Scott Carmichael, Mr. Orlando Gomez, Mr. Mark Bourgeois, Mr. Don Howard (just to name a few), all of them are responsible and patient enough. I enjoyed these courses and lecturers a lot. Thanks for their efforts.

In addition, I want to especially thank my advisor, Dr. Wanpeng Tan. We had a

wonderful cooperation on the project this summer and he taught and inspired me a lot. He is the most interesting person that I've ever met, and I am very willing to work with him. The experience working with him is memorable and unforgettable. He is so patient to teach me basic knowledge and background of the project when I only knew little in this new field, otherwise, I cannot finish the project so quickly and smoothly. Also, he can always accurately point out the problem in the work that I've finished in my progress report to him every time, and then he will give me some key suggestions and encourage me to have my own ideas and verify them. Besides the patient guidance and precious suggestions on the project, he also gave me a lot of invaluable advices on my future research career, which make me feel quite clear and firm about the field that I want to contribute to and the road that I would like to keep on going.

In the end, I want to thank Xi'an Jiaotong University for selecting me to participating in this 2020 REU program, and thank School of Science for the financial support to me. And thank University of Notre Dame again for all in the 2020 REU program. I wish that the REU project gets better and better.

- [1] T. D. Lee and C. N. Yang, *Question of Parity Conservation in Weak Interactions*, Phys. Rev. 104, 254 (1956).
- [2] C. Pitrou, A. Coc, J. Uzan, E. Vangioni, *Precision big bang nucleosynthesis with improved Helium-4 predictions*, Physics Reports 754 (2018) 1–66.
- [3] W. Tan, *Neutron oscillations for solving neutron lifetime and dark matter puzzles*, Physics Letters B 797 (2019) 134921.

Simulation of Fractal Roadway Traffic Using a Simple Roadway Development Model

Zifeng LIU

2020 NSF/REU Program

Physics Department, University of Notre Dame

ADVISOR: Zoltán Toroczkai

Abstract

Roadways are transportation infrastructure networks that are vital to the functioning of a society as they ensure efficient transportation of materials and goods across a wide range of spatial scales. While the structure of roadway transportation networks have been studied previously, the traffic distribution on these networks received less attention. Here we show that the traffic on these networks obeys a fractal scaling. We present a simple model capturing this behavior and hypothesize that it is described by Laplacian growth dynamics, common to many other dynamic fractal phenomena such as viscous fingering, diffusion limited aggregation and dielectric breakdown, to name a few.

1 Introduction

Fractal structures are geometrical structures that have unique properties including scale-independence and self-similarity. Although structurally, roadways are not clear-cut fractals, previous studies[1] have shown the existence of fractal-like scaling in the structure of certain associated networks. Since traffic is one of the most important attributes of a road, it is natural to assume that the traffic distribution on roadways is also fractal. A recent, theoretical paper from T.Nagatani[5] used analytical and numerical approaches to study the traffic behavior in fractal structured model roadways. Nevertheless, the study focused mostly on theoretical analysis. The network used in the article to describe roadways is the percolation-backbone network, which is strictly self-similar and lacks connection with reality. Apart from that, other models and assumptions used and made in the article may also seem inappropriate when considered in real life.

Our work focuses on simulating the evolution process of road networks. We build up a simple model that is fundamental enough to describe the dynamical evolution of a roadway network over a spatial area, such that the growth of the new roads are determined by the appearance of new settlements, the need for connecting this

settlement to the rest of the network and by the traffic distribution on the existing roads at that time. The traffic was simulated using the so-called radiation model, which is a previously validated traffic model[7] that uses the population of villages to calculate the daily commuting flux of every road segment.

One of the most important parts of our model is a hierarchical road system, which assigns higher level roads higher speed limits and shorter travel time, since they generally hold more traffic. This model, although being simple, preserves the most fundamental properties of real life roadway networks.

At last, we used the box-counting algorithm[4] to determine the fractal dimension of the traffic fractal. Possible interpretation of the result is discussed, and Laplacian growth is expected to be the forming mechanism of the fractal.

2 A Simple Roadway Network Development System

In order to model the evolution steps of traffic, we set up a simple model that simulates the growth of a roadway network. As the area constantly receives population influx, the town also experiences an update in traffic. The way we model the traffic is that we used a cost-based radiation model[7],

which is introduced in section 2.2.4.

2.1 Important Assumptions

In order to simplify the system while keeping the crucial properties, we made several important assumptions. We believe that these properties would be able to give an acceptable description of the roadway network in reality.

In our code, we use a directed weighted network to describe the road network. Nodes represent communities or intersections while edges represent road segments. The weight of every edge is assigned with the travel cost of the corresponding road segment, which will be explained in detail in section 2.1.2.

2.1.1 Roads and Villages Placed on Square Lattices

Without loss of generality, we put all roads and villages on a square lattice. This would mean that every node in the network would have a degree that is at most four, and two arbitrarily chosen roads are either parallel or perpendicular to each other.

2.1.2 Hierarchical Speed Limits and Travel Cost

Roads in reality follow a hierarchical structure. Community roads have relatively low traffic thus lower speed limits and capacity, while more major roads like state roads hold more traffic and higher speed limits. In our model, the newly-built roads are assigned with the lowest speed limit. When a road is being used by many citizens (which means decent amount of traffic), the governor would update the road to allow more traffic and shorter travel time. As a consequence, this road would obtain a higher speed limit and lower travel cost.

Research from Y.Ren et al.[7] have concluded that compared to travel distance, travel time is a better measure for travel cost when considered as the weight of the road segment when simulating traffic. Since the time used to travel on a unit length of road is inversely proportional to speed, assuming that roads have no capacity limits(no traffic congestions) and people drive at the speed of the speed limit, we can set the travel costs per unit length as follows.

$$c_{unit} = \frac{d_{unit}}{v_{limit}} \quad (1)$$

In the equation, c_{unit} is the travel cost per unit length, which is also the travel time per unit length. Unit length is written as d_{unit} , and v_{limit} is the speed limit of the road.

We picked the United State's usual settings of speed limits and implemented it into our simulation. The following table shows the settings we are using.

| Road Level | Road Type | Speed Limit (mph) | Travel Cost Per Unit (c_i) |
|------------|----------------|-------------------|--------------------------------|
| 1 | Freeway | 70 | 30 |
| 2 | Main Road | 60 | 35 |
| 3 | Secondary Road | 50 | 42 |
| 4 | Community Road | 20 | 105 |

As long as the ratio between travel costs stays the same, the actual value of the cost does not matter. For simplicity, we set the unit length as 2100 so that we can assign integer values to travel costs.

(Note that $105 * 20 = 42 * 50 = 35 * 60 = 30 * 70$)

2.1.3 Travel Cost of a Road Segment

To acquire the total travel cost of a road segment, we simply multiply the unit cost by the length of the road, which is

$$c_{ij} = c_{unit} \cdot l_{ij} \quad (2)$$

where c_{ij} stands for the travel cost of the edge from node i to node j , c_{unit} stands for the travel cost per unit length, while l_{ij} is the length of the road.

After that, we can obtain the travel cost for every road in our system.

2.1.4 Logistic Population Growth

We know from basic biology that the populations of species in a resource-limited area tend to grow in a logistic pattern, also known as the Logistic growth model. The growth rate is defined as follows:

$$\frac{dp}{dt} = r \cdot p(1 - p) \quad (3)$$

Here, p stands for the population size of a species, and r is the speed parameter.

In the simulation, we set the speed parameter as p , so as to slow down the growth of population. After doing a simple integration, one can get:

$$n_{t+1} = n_t + p \cdot n_t \cdot \left(1 - \frac{n_t}{n_{max}}\right) \quad (4)$$

Here, p stands for the speed parameter

mentioned in the previous paragraph, n_t stands for the population of the village at time t , while n_{max} stands for the maximum number of citizens a village can have, which can also be denoted as n_∞ . Figure 1 illustrates the change of population of a new village, with $n_0 = 200$, $n_{max} = 10000$ and $p = 0.02$.

2.2 The Model

In the simulation of each step, we do the following:

- Generate a new village and connect it to the existing road networks
- Implement Logistic growth to all existing villages
- Use the radiation model to calculate traffic on every road
- Update speed limits if necessary

The following sections further explain the process in detail.

2.2.1 Initial Stage

We tried two different initial settings. The first consists of nine villages positioned on

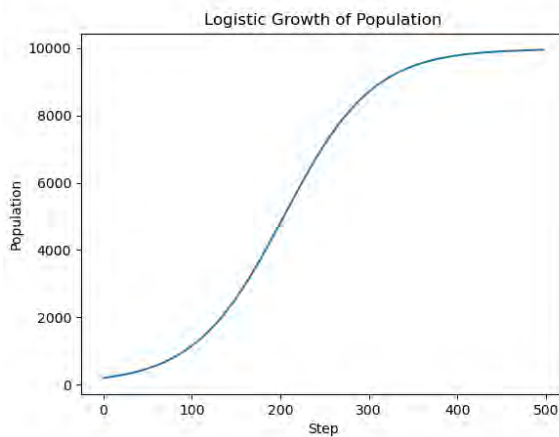


Figure 1: The population change of a new village with initial population $n_0 = 200$, maximum population $n_{max} = 10000$ and update parameter $p = 0.02$. The population reached its maximum value at around 500 steps. We can set the total number of steps in the simulation accordingly, to have an appropriate population distribution.

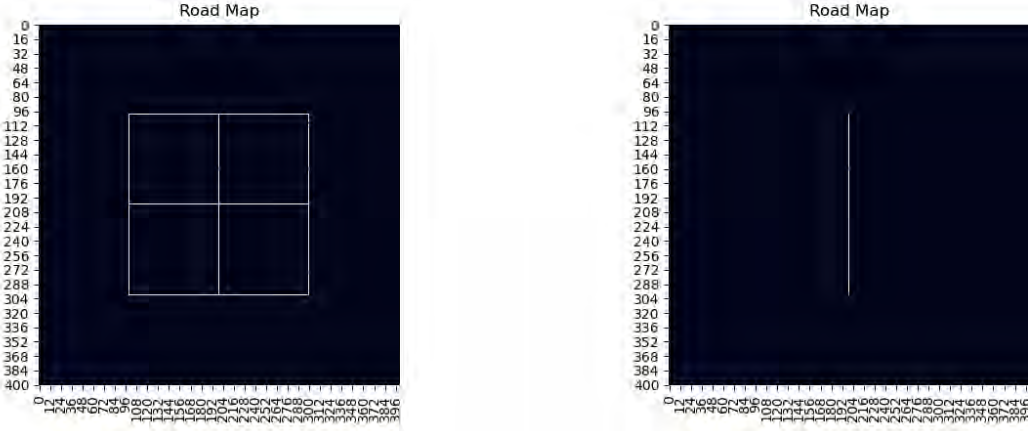


Figure 2: Two initial settings of roads.

a three by three grid, with road connecting adjacent villages(see the picture on the left in fig.2). This setup successfully represent the early stage of a roadway network's development, where there are few settlements in the area. Another is much simpler, with only two villages connected by a single road(see the picture on the right in fig.2).

We assigned the secondary tier of speed limit to the initial roads, since it would be reasonable to assume that initial roads would be built with a higher standard and not necessarily a simple dirt road.

2.2.2 New Settlements and New Road Formation

We put villages randomly in unoccupied regions, in order to simulate the process of the appearance of new settlements. To be more specific, in each step we randomly generate a position and put a new village there. If the position was occupied by a road or a village, we draw a random position again.

After a village is formed, residents of the village need road access to other places. What we did is that roads to four directions, up, down, left, right, will be formed to connect to the nearest existing roads. If such road cannot be found, the formation on that direction will be postponed. Figure 3 illustrates the process, with u being the new

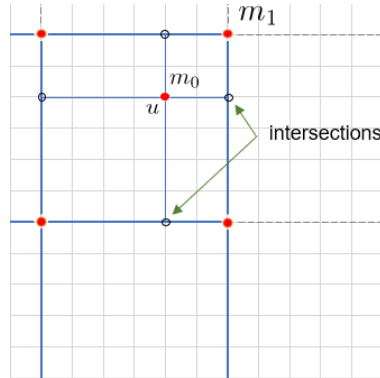


Figure 3: The process of forming intersections and new roads

village.

When a new road is connected to an old road, a T-junction is formed and an intersection is added. Intersection points also work as a node in the roadway network, but with a population of zero.

After putting a new intersection into the network, the previous road will be divided into two sections, which means that they may not necessarily have the same traffic.

Also, if in the process of forming new roads, we found that the new intersection overlaps existing nodes or intersections, no new nodes would be added to the system and the very node will be set as one of the end points of the new road.

Moreover, if all four roads to four directions failed to form, we cancel the formation of the village and continue to the next step. This generally means that the village is too far away from others and may not be able to survive.

2.2.3 Village Population Increase

In this step we update the population of all villages according to the process mentioned in section 2.1.4. Intersections will not experience a population growth, as they hold no settlements.

2.2.4 Calculate Traffic using a Cost-Based Radiation Model[7]

Previous study from Y. Ren et al.[7] have concluded that the average daily OD flux between two nodes in a roadway network can be calculated using a cost-based radiation model. The "O" and "D" in OD flux stands for "origin" and "destination", so OD flux counts the number of people traveling from the origin point to the destination point. Although occasional travels may have an impact on the traffic, we should notice that since we are counting the average OD flux,

after being averaged over a long period of time, these occasional travels can be ignored since commuters take up the most part of the traffic. To conclude, the average flux would only count the number of people who travel routinely between their homes and their work places.

The radiation model gives an innovative way to find the OD flux, by assuming that people will find the nearest job opportunity that satisfies their expectation. Previous work[8] has found an expression for p_{ab} , which stands for the probability for a person lives in site a (with population of m_a) to find its nearest satisfactory job at site b (with population of n_b), given that the travel cost between two places is c_{ab} .

With that expression at hand, we can work out the expression for the commuting flux:

$$\Phi_{ab} = \zeta m_a p_{ab} \quad (5)$$

where Φ_{ab} is the average number of daily travellers going from site a to site b , and ζ means the proportion of commuters among the total population. The parameter of ζ should be regarded as an overall constant and is a minor factor for the simulation.

Previous studies[8] have derived the expression of p_{ab} , and the flux can be written as:

$$\begin{aligned} \Phi_{ab} &= \zeta m_a p_{ab} \\ &= \zeta \frac{m_a^2 n_b}{(m_a + c_{ab})(m_a + c_{ab} + n_b)} \end{aligned} \quad (6)$$

The population at site a is denoted as m_a , site b as n_b , and the travel cost between node a and node b is written as c_{ab} .

Since we keep a record of the population of every node, it is easy to calculate the OD flux between every two given nodes.

Since we assign travel time to each road segments, for every pair of origin and destination, we can find the optimal path (denoted as ω_{ab}) that has the least travel

time. Assuming that everyone chooses the fastest route, by simply summing through all possible OD pairs, we can get the traffic flow of every road segment, denoted as T_{ij} for the edge connecting node i to node j . The previous process can be written as follows to solve the degeneracy problems for ω_{ab} .

$$T_{ij} = \sum_{a,b \in V} \frac{g_{ab}(i,j)}{g_{ab}} \Phi_{ab} \quad (7)$$

where g_{ab} counts the total number of optimal paths from node a to node b , and $g_{ab}(i,j)$ counts the number of optimal paths that contain the edge of (i,j) .

In every step, after updating the population of each village, we can calculate the traffic of each road segment and get ready to update speed limits, if necessary.

2.2.5 Update Speed Limits

If the traffic of a road segment reaches a certain threshold, the road will experience an update in speed limit, giving the road a lower travel cost.

We might notice that in reality, if a road segment experiences high traffic, it is more likely for the whole road, rather than the single road segment, that gets a raise in speed limit. We simulate the procedure as well.

We update the speed limits according to

the following:

$$c_{ij} = \begin{cases} c_1, & T_{ij} > t_1 \\ c_2, & t_2 < T_{ij} \leq t_1 \\ c_3, & t_3 < T_{ij} \leq t_2 \\ c_4, & T_{ij} \leq t_3 \end{cases} \quad (8)$$

Here, c_i follows the definition from 2.1.2, and T_{ij} stands for the traffic of the road connecting node i and node j , and t_i is defined as follows:

| Threshold for Travel Cost per Unit Length | Values |
|---|--------------|
| t_1 | $n_{max}/50$ |
| t_2 | $n_{max}/5$ |
| t_3 | n_{max} |

where n_{max} is defined in section 2.1.3. Note that the update process may skip some stages, if the road experienced an abrupt boost in traffic.

After this, the system is ready to move on to the next round of simulation.

3 Unrealistic roads

After analyzing the result, we found some part of our simulation to be unrealistic. We noticed that most new villages that formed inside the grid have formed four new roads to four new directions, but we may notice that some of them does not have much traffic and not every road is being used. This seems to be different from reality, since building a road



Figure 4: An example of unrealistic long parallel roads

is costly, and new roads will not be allowed to be built if it costs too much while having poor traffic. This is especially concerning when we see long parallel roads that are very close to each other. Fig 4 shows an example.

4 Revised System: Eliminate Unimportant New Roads

As discussed in section 3, some roads should not be built since they are low in cost performance. To solve the problem, in every step, we first carry out a trial run with new roads in the system, to determine if the road is useful or not to the system. After obtaining the traffic value for each of the road segments, we go through all newly added roads and add to the network new roads that have high enough traffic-length ratio. The formation of some roads would be postponed if the road is proved to be not worthy.

In other words, a new road will be formed only if:

$$\frac{T_{ij}}{l_{ij}} - \text{threshold} > 0 \quad (9)$$

where the *threshold* is defined as $\frac{m_0}{\text{scale}/8}$ in our model, so that the requirement is neither too strict nor too weak.

The village will not be formed if all new roads failed to form.

To sum up, the updated system works as the following:

- Generate a new village and form trial roads to connect it to the existing road networks
- Implement Logistic growth to all existing villages
- Use the radiation model to calculate traffic on every road

- Cancel the formation of unnecessary roads
- Simulate the traffic again
- Update speed limits if necessary

5 Results

5.1 Road Network

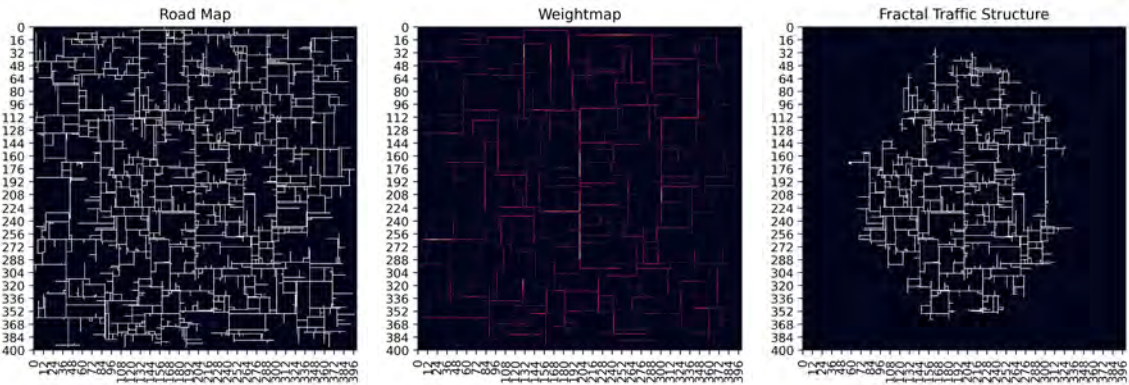
Part(a) in figure 5 shows one of the road network we generated. We are able to see long and short roads covering the whole surface in a reasonable layout. Long paralleled roads cannot be found, meaning that the measure took in section 4 turns out to be successful. Part(b) in figure 5 shows the travel cost of every road, from where we can see the hierarchical pattern of roads.

5.2 Fractal Pattern of Traffic

We can show the fractality of traffic in this way: fix a node in the system, and a fixed cutoff threshold for travel cost. We then plot all positions that are reachable within the cutoff travel cost. The figure we obtained from the simulation(figure 5) truly represents the fractal characteristic of road networks. We are confident to say that it truly look like a fractal, since the pattern looks like fractal clusters formed through diffusion limited aggregation process[3], and dielectric breakdown[6].

5.3 Fractal Dimension

We used the box-counting method[4] to calculate the fractal dimension of the fractal pattern we get from section 5.2. The box-counting method is a widely used method to calculate the fractal dimension, and detailed explanation of the method can be found here[4].



(a) Roadway network created with 1500 steps and the line initial stage
(b) Weight of every road. Brighter means time and higher rank.
(c) Fractal created with travel cost cutoff at 6300

Figure 5: Results

Using the box-counting algorithm, we found the following results:

| Initial Stage | Cost Cutoff | Fractal Dimension |
|---------------|--------------------------|-------------------|
| Line | 4200 | 1.381 |
| | 6300 | 1.490 |
| | 8400 | 1.567 |
| | Infinity (Whole Network) | 1.601 |
| Grid | 4200 | 1.375 |
| | 6300 | 1.509 |
| | 8400 | 1.616 |
| | Infinity (Whole Network) | 1.632 |

5.4 Possible Mechanism: Laplacian Growth

The formation of some fractals, for example viscous fingering, diffusion limited aggregation, and dielectric breakdown, is closely related to the process of Laplacian growth. Laplacian growth means that the boundary of the pattern is growing at a rate proportional to ∇P , with P named as the Laplacian field. Outside of the domain the

The Laplacian field P differs in different scenarios. For instance, DLA clusters can be reproduced when P is defined as the probability field for the random walking particle to hit the pre-existing structures[2]. In the formation of viscous fingering, P is found to be the pressure, and the fact that the pressure in viscous fluid satisfies the Laplace equation $\nabla^2 p = 0$ leads to the fractal structure of viscous fingering[2].

Since the traffic distribution pattern closely resembles to the DLA pattern, we assume that the forming mechanism of traffic structure should be similar. The feature that new road formations is closely related to previous structures can also be found in the DLA formation[3], and other formation procedures of fractals.

Future work can be focused on finding the exact expression for the potential in Laplace equation.

6 Summary

In summary, we have formulated for the first time, a basic roadway network evolution model that keeps the essential features of population growth over a spatial area and provides optimal transportation pathways in that area. Our model, in accordance with real-life observations of traffic distribution demonstrates that the roadway network evolution is hierarchical, which in turn, as we have shown, generates fractal traffic structures. If possible, future work could provide more concrete evidence that is in support of the Laplacian formation mechanism.

References

- [1] V. Kalapala, V. Sanwalani, A. Clauset, and C. Moore. Scale invariance in road networks. *PHYSICAL REVIEW E*, 73, 2006.
- [2] J. Mathiesen, I. Procaccia, H. L. Swinney, and M. Thrasher. The universality class of diffusion-limited aggregation and viscous fingering. *Europhysics Letters*, 257–263, 2006.
- [3] P. Meakin. Formation of fractal clusters and networks by irreversible diffusion-limited aggregation. *Physical Review Letters*, 1119–1122, 1983.
- [4] F. Moisy. *Computing a fractal dimension with Matlab: 1D, 2D and 3D box-counting*. <http://www.mathworks.com/matlabcentral/fileexchange/13063-boxcount/content/boxcount/html/demo.html/>, 2008.
- [5] T. Nagatani. Traffic flow on percolation-backbone fractal. *Chaos, Solitons and Fractals*, 135, 2020.
- [6] L. Niemeyer, L. Pietronero, and H. J. Wiesmann. Fractal dimension of dielectric breakdown. *Physical Review Letters*, 1033–1036, 1984.
- [7] Y. Ren, M. Ercsey-Ravasz, P. Wang, M. C. González, and Z. Toroczkai. Predicting commuter flows in spatial networks using a radiation model based on temporal ranges. *Nat. Commun.*, 5:5347, 2014.
- [8] F. Simini, M. C. González, A. Maritan, and A.-L. Barabási. A universal model for mobility and migration patterns. *Nature*, 96–100, 2012.

Investigating Wobbling Motion in ^{135}Ce

Sariah Phipps

2020 NSF/REU Program

Physics Department, University of Notre Dame

Advisors:

Umesh Garg

Nirupama Sensharma

Abstract

Due to the breakthrough identification of ^{135}Pr as a wobbling nucleus, the A~130 mass region has emerged as a new region of interest to look for exotic nuclei. Wobbling and chirality serve as two irrefutable signatures for the existence of triaxiality. Having already established chirality in ^{133}Ce , the present study aims to look for wobbling in the neighboring ^{135}Ce nucleus where a possible longitudinal wobbling band has been identified. After obtaining and analyzing the DCO-Like ratios of the transitions in the proposed wobbling band, it was determined that it does not correspond to a wobbling motion.

I. INTRODUCTION

Triaxiality occurs when a nucleus has three axes of different moments of inertia. Scientists rely on experimental techniques to identify some unique signatures that only triaxial nuclei can exhibit. Triaxiality can be identified by two attributes: wobbling and chirality.

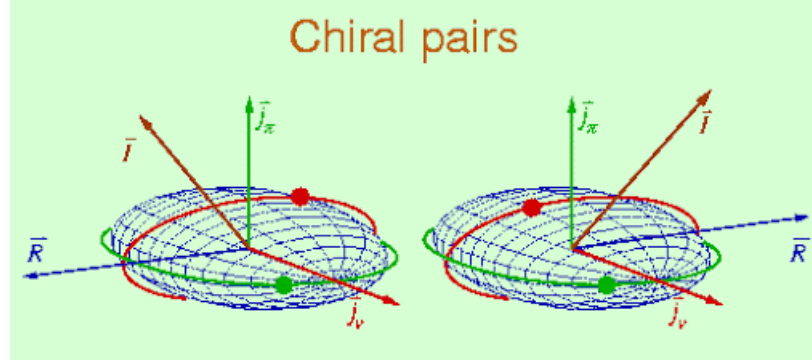


FIG. 1: Two mirror images of a chiral molecule. R is the rotor angular momentum, J is the total angular momentum, j_π is the angular momentum of the odd proton, j_ν is the angular momentum of the odd neutron.

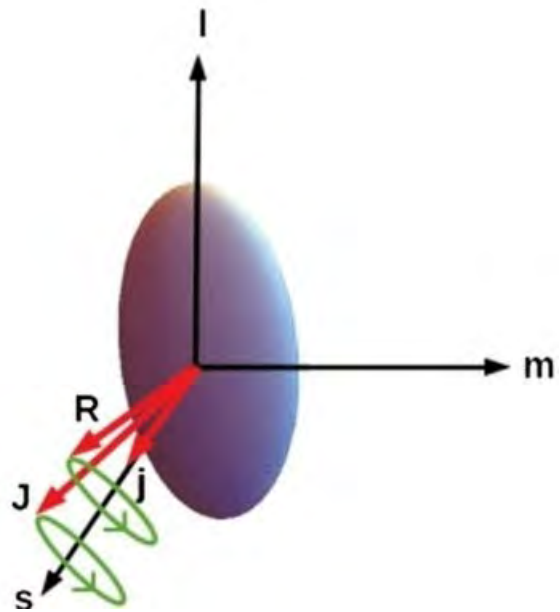


FIG. 2: Angular momentum geometry of a transverse wobbler in the body fixed frame, where I , m , and s correspond to the long, medium, and short axis, respectively. R , j , and J are the rotor, odd particle, and total angular momentum, respectively. Credit: Physical Review Letters (2020). DOI: 10.1103/PhysRevLett.124.052501

As seen in Figure 1, Chirality occurs when the axis of rotation lies outside any of the

three principal planes and exhibits right or left handedness. Wobbling, on the other hand, occurs when one of the nucleus' three axes precesses about the total angular momentum. An example of a wobbling nucleus can be seen in Figure 2. If either of these attributes are experimentally observed, then the nucleus can be identified as having a triaxial shape. Until recently, wobbling had only been observed in five nuclei since its initial prediction: ^{161}Lu [1], ^{163}Lu [2], ^{165}Lu [3], ^{167}Lu [4] and ^{167}Ta [6]. Although chirality has been experimentally observed much more than wobbling, the focus of this work is on observing wobbling.

In 2015, a breakthrough occurred when a research group at The University of Notre Dame discovered wobbling in ^{135}Pr [7]. This was the first instance of wobbling outside the mass 160 region, but there was a discrepancy in understanding the properties of the observed wobbling bands. Wobbling energy is associated with wobbling excitations and was initially predicted to increase with spin. However, all experimentally observed cases so far have exhibited a decrease in the wobbling energy with increasing spin. This discrepancy was resolved by S. Frauendorf and F. Dönau by utilizing the Quasiparticle Triaxial Rotor (QTR) model to study triaxiality in odd-mass nuclei [8]. The QTR model uses transverse and longitudinal as the wobbling modes within a nucleus. Longitudinal wobbling occurs when the odd particle aligns with the maximum MOI axis (medium axis) of the triaxial core while transverse wobbling occurs when the odd particle aligns perpendicular to the maximum MOI axis (short or long axis) of the triaxial core. It was found that the triaxial even-even core was coupled to an odd quasiparticle, modifying the motion considerably. With this interpretation, all the wobbling bands observed until then corresponded to transverse wobbling with ^{135}Pr opening a new region for observation of wobbling motion. ^{133}Ce , another nucleus within said region, was previously found to have chirality, making further research in the $A \sim 130$ region optimal for finding triaxiality. For this reason, ^{135}Ce has been identified as a possible candidate for a wobbling nucleus.

We are able to observe wobbling within the nucleus by using data from the Argonne National Laboratory's Gammasphere. The method of receiving the data is the same as reported in [7], but will be briefly restated. The ATLAS facility at the Argonne National Laboratory produced an 80-MeV beam of ^{16}O that was incident on a ^{123}Sb target. This was

to populate the levels of interest in ^{135}Pr , including other nuclei such as ^{135}Ce . The target used was a $634 \mu\text{g}/\text{cm}^2$ -thick foil of ^{123}Sb with a $15 \mu\text{g}/\text{cm}^2$ aluminum layer at the front. At the time of the experiment, the Gammasphere array had 83 working Compton-suppressed Germanium detectors arranged in 17 different angular rings around the beam line. Data was acquired in the triple coincidence mode. The upgrade to the digital Gammasphere (DGS) enabled collection of nearly 4 times as much data as that in previous experiments in a similar amount of beam time – a total of 1.45×10^{10} three and higher fold γ -ray coincidence events.

Before the data was analyzed, it was calibrated for energy and efficiency. I then constructed a matrix and cube that helped us create a level scheme. From carefully examining that level scheme and DCO (Directional Correlation of Oriented Nuclear States) - Like ratios, we are able to investigate the yrast band within ^{135}Ce and determine that it was not a wobbling band

II. METHOD

With the data recorded, it was my job to decipher it. The 83 working detectors provided different spectra that needed to be calibrated due to its varied starting points and background counts. The energy and efficiency calibrations were performed for each of the working detectors of the Gammasphere array using a standard ^{152}Eu radioactive source. From the energy spectra, I used RADWARE's auto calibration function to filter out the peaks that match with ^{152}Eu . However, the varied background energies received by each detector meant that the auto-calibration function was not always guaranteed to work. To check the accuracy of my calibration, I used RADWARE's effit and encal functions to fit the data from calibrations to an exponential curve shown in Figure 3. There were several detectors whose background peaks prohibited them from being auto-calibrated accurately, making several points on the curve fit deviate. To fix this error, I manually calibrated the desired peaks until I was able to fit an accurate curve. Once all the detectors were calibrated, I added all the spectra together and calibrated the total relative efficiency of the data as seen in Figure 3.

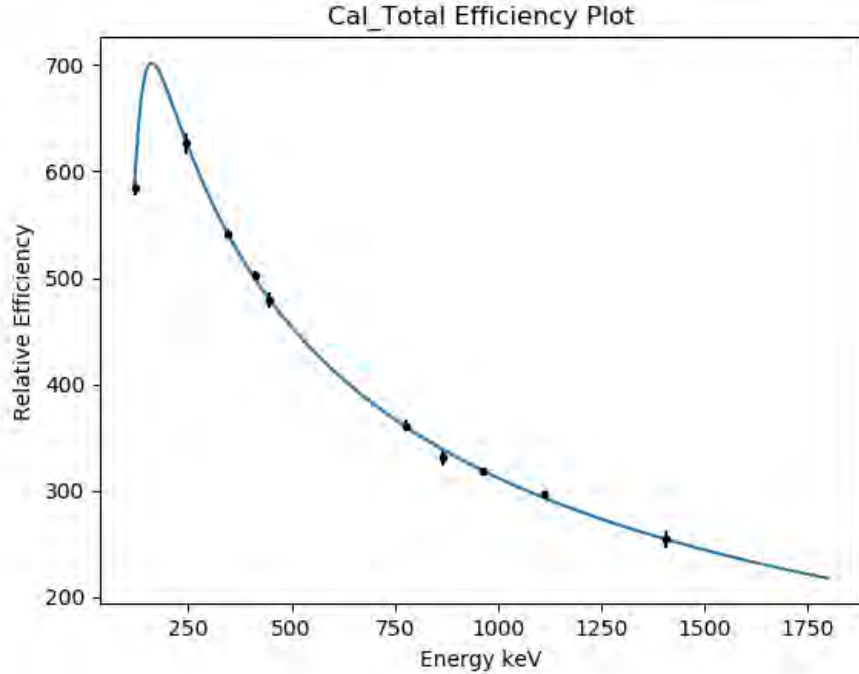


FIG. 3: The efficiency plot of the total calibrated data. The equation for the curve fit is $\text{eff} = e^{[(A+Bx+Cx^2)^{-G} + (D+Ey+Fy^2)^{-G}]^{-\frac{1}{G}}}$ where A, B, and C describe the efficiencies at low energies and D, E, and F describe the efficiency at high energies.

Next came creating the level scheme. ^{135}Ce has been observed in two previous cases, so I used the papers from [9] and [10] to construct a level scheme. The data that Notre Dame had collected had more statistics, so we were able to look at the level scheme more clearly and build a more accurate version. Using gf3, a program that edits and displays spectra, I was able to search for each energy and transition from the previous papers. Many of the previously observed energies were visible in the data we had collected, but there were some transitions that were too weak to observe. The transitions between the yrast band and the $n=1$ band were found to connect only in one direction, making the $n=0$ and $n=1$ bands an optimal place to look for wobbling. The level scheme can be seen in Figure 4.

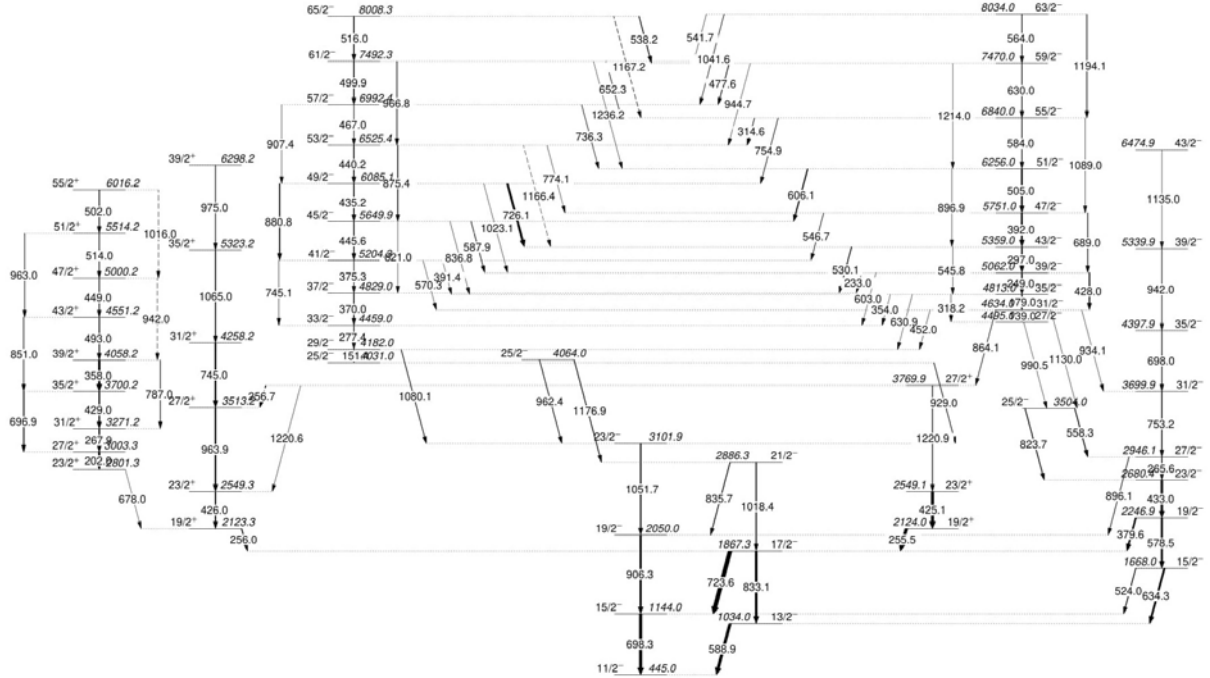


FIG. 4: The level scheme of ^{135}Ce .

To be certain of wobbling, I needed to organize the data into rings based off of the detector angles. All the spectra were put into three different rings: forward, middle, and backward. Like stated earlier, there was a possibility of wobbling in the $n = 0$ and $n = 1$ bands so I viewed the energies within those bands. Using the area and error of the curves on the spectrum, I was able to obtain the DCO-Like ratios and see if it matched what was predicted.

III. RESULTS AND DISCUSSION

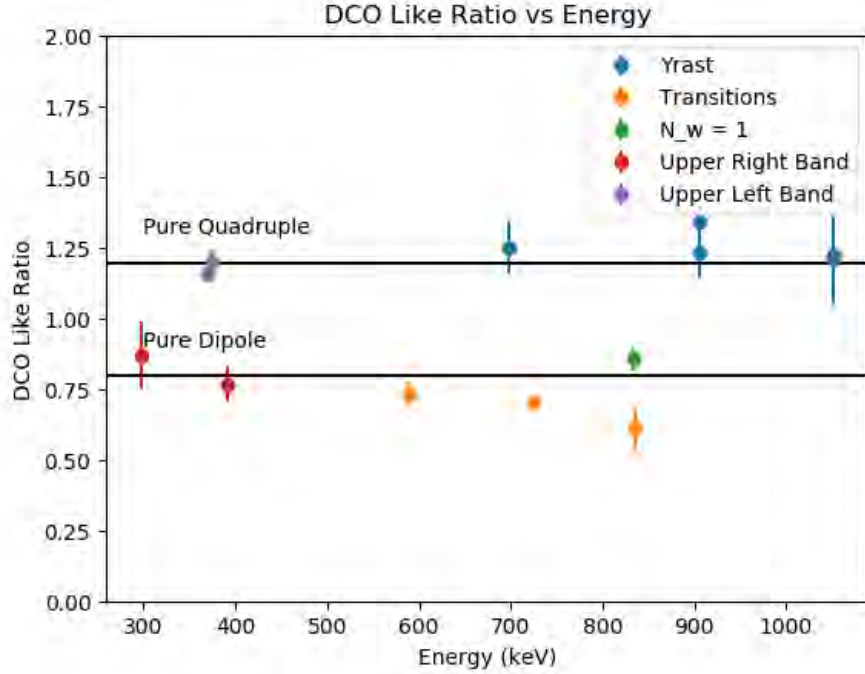


FIG. 5: The DCO Like Ratio vs Energy. The Pure Dipole and Pure Quadrupole lines are where we expected the DCO-Like ratio to be.

| | Energy | DCO like ratio | Error |
|-------------|--------|----------------|-------|
| yrast band | 698 | 1.25 | 0.09 |
| | 906 | 1.34 | 0.07 |
| | 906 | 1.24 | 0.09 |
| | 1052 | 1.21 | 0.16 |
| | 1052 | 1.22 | 0.14 |
| transitions | 724 | 0.71 | 0.02 |
| | 588.9 | 0.74 | 0.04 |
| | 836 | 0.61 | 0.08 |
| n=1 | 833.1 | 0.86 | 0.04 |
| Upper Right | 297 | 0.87 | 0.12 |
| | 392 | 0.77 | 0.06 |
| Upper Left | 375.3 | 1.21 | 0.04 |
| | 370 | 1.16 | 0.03 |

FIG. 6: The DCO-Like Ratios of the yrast, transition, $n_w = 1$, upper right, and upper left bands.

A wobbling band would produce a mixed ratio, meaning a value for the DCO-Like ratios between 0 and 0.8 if it was an odd proton (negative mixing ratio) or between 0.8 and 1.2

if it was an odd neutron (positive mixing ratio). ^{135}Ce has an odd neutron, so we expected a positive mixing ratio. However, as can be seen from Figure 5 and Figure 6, the DCO-Like Ratios for the connecting transitions are close to 0.8. This means that the transitions are pure dipole. Since the transitions are not a positive mixing ratio like we expected, we can conclude that the band we are looking at is more likely a signature partner band and not a wobbling band. To continue searching for wobbling bands, angular distribution measurements will be done to confirm the multipolarities of the connecting transition. We will also keep looking for wobbling motion in this region of nuclear chart.

IV. ACKNOWLEDGEMENTS

This work has been supported in part by the National science Foundation (Grants No. PHY-1559848, PHY-1419765 and PHY-1713857).

- [1] *P. Bringel, et al.*, Eur. Phys. J. A 24 (2005) 167–172, <https://doi.org/10.1140/epja/>
- [2] *S. Ødegård, et al.*, Phys. Rev. Lett. 86 (26) (2001) 5866–5869, <https://doi.org/10>
- [3] *G. Schönwaßer, et al.*, Phys. Lett. B 552 (2003) 9–16, [https://doi.org/10.1016/S0370-2693\(02](https://doi.org/10.1016/S0370-2693(02)
)03095-2
- [4] *H. Amro, et al.*, Phys. Lett. B 553 (2003) 197–203,
[https://doi.org/10.1016/S0370-2693\(02\)03199-4](https://doi.org/10.1016/S0370-2693(02)03199-4).i2005-10005-7.
- [5] *D.J. Hartley, et al.*, Phys. Rev. C 80 (2009) 041304,
<https://doi.org/10.1103/PhysRevC.80.041304>.
- [6] *J.T. Matta, et al.* Phys. Rev. Lett. 114 (2015) 082501, <https://doi.org/10.1103/PhysRevLett.114.082501>.
- [7] *N.Sensharma, et al.*, Two-phonon wobbling in ^{135}Pr ., Physics Letters B 792 (2019) 170–174
- [8] *S. Frauendorf, F. Dönau*, Phys. Rev. C 89 (2014) 014322, <https://doi.org/10.1103/PhysRevC.89.014322>.
- [9] *AIP Conference Proceedings 764*, 99 (2005); <https://doi.org/10.1063/1.1905297>

- [10] R. Ma , E.S. Paul, 'D.B. Fossan, Y.Liang, N.Xu. Rotational bands in ^{135}Ce : Collective prolate and oblate rotation. Physical Review (1990) C;41(6)

Monte Carlo Analysis of the St.George Detector using Geant4

Adam Sanchez

2020 NSF/REU Program

Physics Department, University of Notre Dame

Advisor: Dr. Manoel Couder

Abstract

The St.George recoil mass separator at the University of Notre Dame is used to study the nuclear reactions that power the stars. These reactions are rare and this rarity necessitates that the efficiency of the detection system of St.George is well understood. Monte Carlo simulations created in Geant4 were used to simulate the detection system of St.George for this purpose. In particular, the role of position of the incoming ion beam and its respective energy on the efficiency was studied. Upon examination, a positional dependence on the efficiency was determined to be significant. Only about 55% of the low energy ions that entered the detection system at a large diameter made it to the detector compared to the overall efficiency of about 92%. Through analysis of the efficiency sensitivity to the incoming ion energy, future researchers will be able to apply the efficiency corrections deduced in this work.

Introduction

The mechanisms through which stars produce vast quantities of energy and various elements has been continuously studied since the discovery of nuclear fusion in the 1930s. With this discovery came an array of new questions that needed to be answered. How are heavier elements created as a result of these collisions? How likely are they to occur?

Therein lies the interest of the St.George group at Notre Dame. Armed with the recoil mass separator of St.George, they can measure the nuclear reaction rates of elements up to an atomic mass number of 40. Specifically, they are interested in what are known as helium

capture reactions where, as the name would suggest, helium is captured by heavier elements within stars producing vast quantities of energy. Measuring these reaction rates not only allows us to understand the production of energy in stars but also how our universe was populated with the elements that appear on the periodic table. With this knowledge, more refined models of stellar energy production and evolution can be created.

The St.George recoil mass separator is designed to accept incoming beams of ions that are then focused onto a target composed of helium gas. Both the beam and the reaction products continue on to a mass filter, which rejects the beam and allows the reaction products to continue on to the detection system.

Inside the detection system, there are two foils whose purpose is collecting time of flight of the passing ions, as the magnetic field present around the foils deflects the released electrons into another detector that keeps track of the timing [1]. However, as is the case with all detectors, St.George is not 100% efficient in detecting all the reaction products that are generated. In order to extract cross sections from experiment, the efficiency of the detector needs to be well understood. This is where the simulation comes in.

Using the Geant4 simulation software [2], a model of the detection system of St.George is being built that will allow for an analysis of the detection system's efficiency. Taking into account the rarity of the interactions being observed, this information will be used to understand the limitations of St.George.

The focus of the current research on the simulation of St.George is adding components to the simulation that make it more similar to the real detection system. This is all in

service of determining the effect the position of the incoming beam has on the efficiency. Due to deflections caused by multiple Coulomb scattering (MSC), there is reason to believe that there will be a significant radial dependence on the efficiency. The idea is that as the particle travels along its path to the detector, and the further away it is from the center of the foils it travels through, the more likely it is that its deflection due to MSC will cause it to miss the detector. In the process of testing this hypothesis we showed that there was also a large energy dependence on the deflection of incoming ions, so this is an additional parameter that was explored.

Methods and Materials

Simulations are built in Geant4 which is a powerful Monte Carlo simulation software and it is well suited for the efficiency analysis that is required. The analysis software known as ROOT [3] was also used in tandem with Geant4 in order to analyze the results of the simulation. It is a common practice when designing systems in Geant4 to use a previous example that is similar to the detector that is needed, and build off of it. That was the case with the simulation that was initially handed to us, all of the relevant physics and detection systems had already been programmed, but the actual detection system was bare-bones and did not fully reflect that of St.George. For example, as it was, the foils were essentially floating in midair, and deflected particles were free to circumvent them and hit the detector, whereas in reality there would be a plate of metal preventing this. As a result, a large portion of the work done was set aside to make the simulation more representative of the actual detection system as shown in Figure 1.

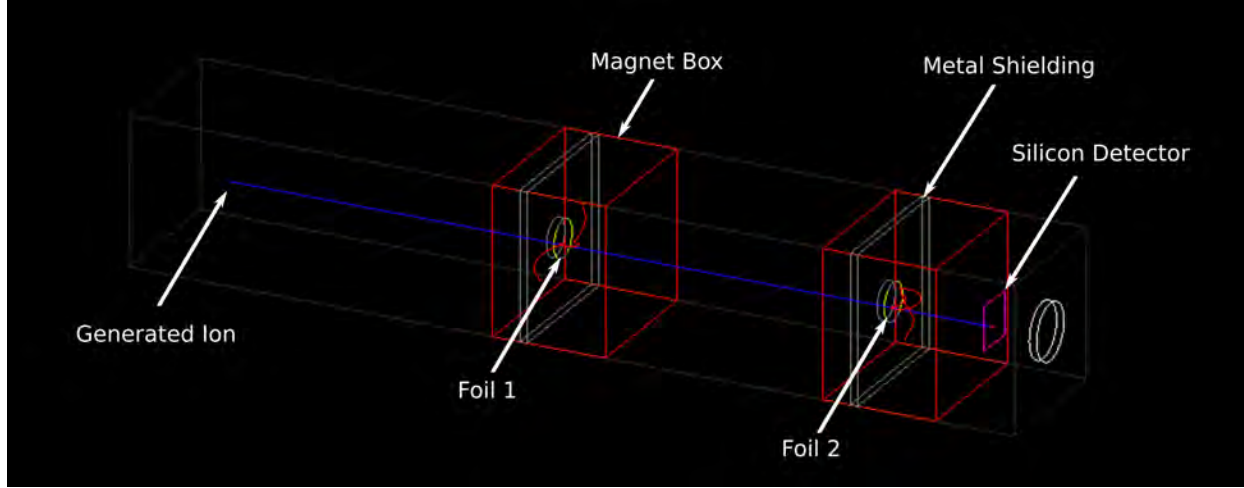


Figure 1: A visualization of the final state of the simulation.

The Wentzel model of MSC was used in the simulations. It was chosen in order to eventually compare results with the data provided by the Urban model that Geant4 uses by default. In addition, research conducted by Makarova, et al. indicates that the Wentzel model agrees best with the findings of similar experiments [4].

For the purpose of examining the best and worst case scenario with regards to particles reaching the detection system, two methods of generating particles were tested. The first is what will be referred to as random generation, and represents the extreme case where the particles come in at angles near the acceptance range of the device.

To generate particles in this manner, two points are randomly selected on the surface of both foils. The incoming ion is then sent on a path where, without the inclusion of the foils, it would fly through these two points (see Figure 2). Alternatively, the second method is representative of the ideal case where all incoming ions are parallel to the detection system. Here the generation method is simple: randomly select a point on the surface of the first foil and select the same point on the other foil and send the ion on the appropriate path.

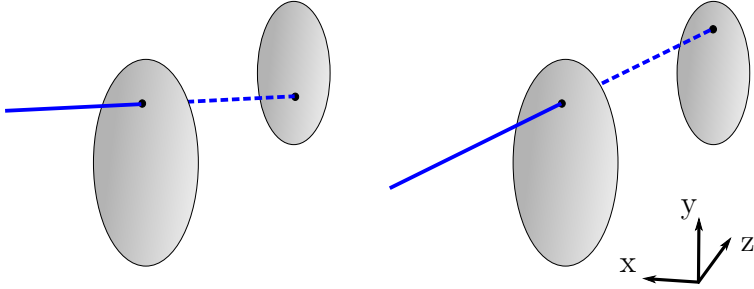


Figure 2: The random generation method (left) and the parallel generation (right).

Radial efficiency was calculated by taking the number of particles within a certain radius range on the first foil that hit the detector and dividing it by the number that just hit the first foil in the same radius range. Likewise, the energy dependent efficiency was calculated by taking the number of particles that are generated with a certain energy and hit the detector, and dividing it by the number of particles that generate with that energy.

In addition to the predicted inefficiency due to MSC as the ion interacts with atoms in the foils, another source of inefficiency is inherent to the 70 Gauss magnetic field present in the boxes in which the foils are contained. The magnetic field in these boxes is directed upwards in the positive y-direction, so for the positively charged atoms that were tested, there will be a slight deflection to the right as seen looking towards the silicon detector.

This deflection is slight overall, as shown in Figure 3. Note that while the mean shows that the deflection is in the negative x-direction, this is just a quirk of the coordinate system chosen (see Figure 2), and the deflection is indeed to the right as confirmed by the visualization of the simulation. This effect will need to be considered when analyzing the radial efficiency but the deflection is slight and should only cause ions near the outer edges of the foil to hit the metal shielding.

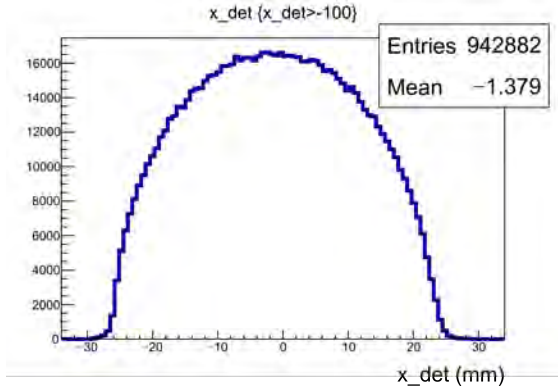


Figure 3: Graph of the location on the x-axis of where the ions hit the detector.

Two different simulations were being tested: one with a 1 inch set of foils with a carbon coating of about 0.5nm, and one with a 2 inch set of foils with an aluminum coating of a similar thickness. The 1 inch foils were used in St.George prior to this research, and the 2 inch foils have only recently been installed. For each of these two foils, three separate ions were tested: argon-40, fluorine-19 and carbon-12.

The bulk of the analysis was done via macros created in ROOT. One macro was created to scan across energy and radii ranges in order to examine the radial efficiency, and another was used to study the overall efficiency based on the energy per nucleon of the incoming ions.

Results

After analyzing the output of the ROOT macros, there was a notable sensitivity of the efficiency to both the radius and the incoming energy. As shown in Figure 4, the radial sensitivity is only apparent in the last few mm of the foil radius. Averaging across both generation methods, in the last 0.508mm of the 2-inch foils, only 59% of the ions with an energy of 1 MeV per nucleon are detected, compared to the average overall efficiency of

about 94%. Contrasting this with the respective efficiencies of the 1-inch foils, 50% in the last 0.254mm and 90% overall, the 2-inch foils seem to be slightly more efficient. There does seem to be a large disparity between the radial efficiency of the particle generation methods however. As seen in Figure 4, the data for the parallel generation methods is very smooth, and follows the line of best fit nicely. However, with the random particles the data is much more noisy so it was hard to find a good model to fit to the data. This noise can likely be attributed to the randomness of the generation method.

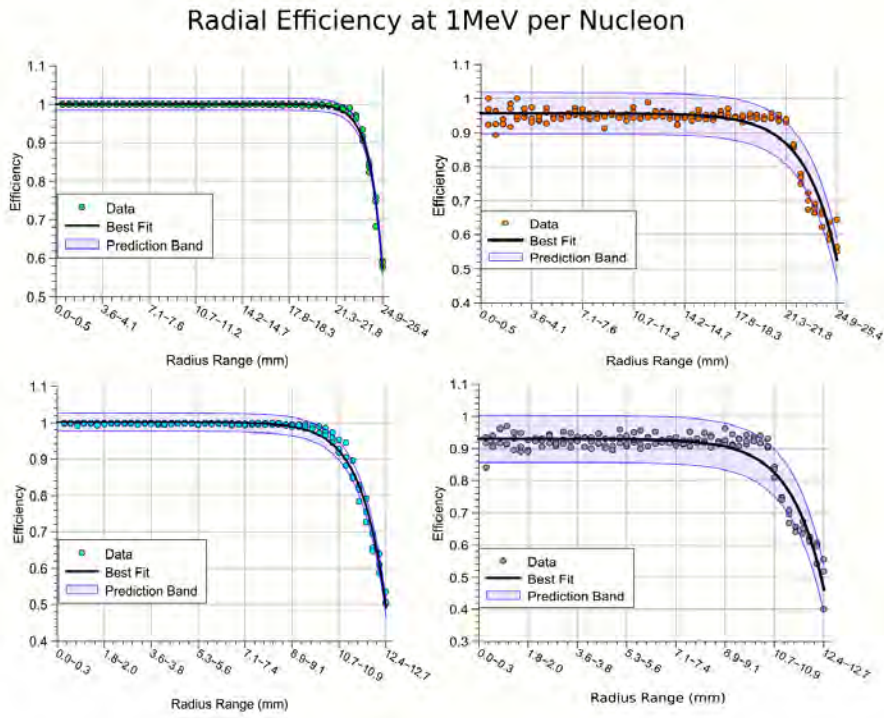


Figure 4: Radial efficiency for parallel ions (left) and random ions (right) for various energy ranges. The two graphs at the top are for the 2-inch foils, and the bottom two are for the 1-inch foils.

After analyzing the data from the three ions that were tested, the results seemed to be largely independent on the amount of nucleons the ion had. Therefore for the purpose of analysis, the data for the three ions was compiled together to produce Figures 4 and 5.

With regards to the predicted inefficiency caused by the presence of a magnetic field, the effect had a small but detectable difference. In a simulation of one hundred thousand carbon-12 particles, the efficiency was decreased by approximately 1.6% as a result of the magnetic field. The deflections due to its effects were taken into account in all of the data that was collected.

Figure 5 shows the data collected for both foils that explored the relationship between the overall efficiency and the energy of the ion.

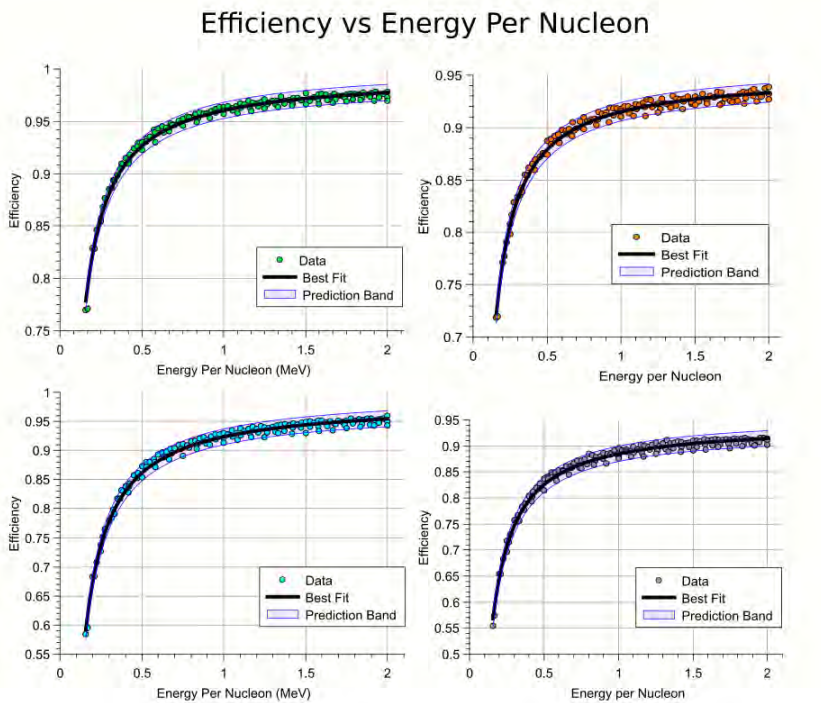


Figure 5: Efficiency vs energy per nucleon for parallel ions (left) and random ions (right). The two graphs are the top at for the 2-inch foils, and the bottom two are for the 1-inch foils.

While the shape of the graphs are all similar, there is a clear difference between the two foils. Across both particle generation methods, the 2-inch foils have a higher efficiency compared to the 1-inch foils at all of the energy ranges tested. This is promising as the

2-inch foils were installed in the hopes of having a more efficient detection system.

Conclusion

In studying the parameters that characterize the efficiency of St.George, it has been determined that the energy of the incoming ions and the position at which they come into the detection system plays a significant role. For the newly installed 2-inch foils, the impact of beam position was shown to be less impactful to the overall efficiency than it was with the 1-inch foils. This leads to the conclusion that the detection system is more efficient with the 2-inch foils installed. While not all of it was shown here, the radial efficiency analysis can be extended beyond 1 MeV per nucleon to the $\approx 0.2\text{MeV}-2\text{MeV}$ per nucleon range for all the ions tested with the data provided with the created ROOT macros. Using this in conjunction with the efficiency vs energy per nucleon analysis provided, future researchers will be able to apply the efficiency corrections deduced in this work.

References

- [1] M.Couder, G.P.A Berg, J. Görres, P.J. LeBlanc,L.O. Lamm, E. Stech, M. Wiescher, J. Hinnefeld, *Design of the recoil mass separator St. George*, Nucl. Instr. and Meth. A, Volume 587, Issue 1, 2008.
- [2] S. Agostinelli, et al., GEANT4 - A simulation toolkit, Nucl. Instrum. Methods Phys. Res. A 506 (2003) 250–303
- [3] Brun R and Rademakers F ROOT Object Oriented Data Analysis Framework *New computing techniques in physics research V. Proceedings, 5th International Workshop, AIHENP '96 (Lausanne, Switzerland, September 2-6, 1996)*
- [4] Makarova, Anastasia Gottschalk, Bernard Sauerwien, Wolfgang. *Comparison of Geant4 multiple Coulomb Scattering models with theory for radiotherapy protons*. Physics in Medicine and Biology. 62. 10.1088/1361-6560/aa6ce3 (2016)

Simulating Stars:
Analyzing the Efficiency of the St. George Recoil Separator

Isabella Valdes

2020 NSF/REU Program

Physics Department, University of Notre Dame

Advisor: Dr. Manoel Couder

Abstract

The Strong Gradient Electromagnetic Online Recoil separator for capture Gamma Ray Experiments (St. George) measures (α, γ) reactions by detecting heavier reaction particles. Comparing particle detections with beam count gives the reaction probability. However, the detection system of St. George lacks efficiency data, meaning there may be less particles detected than created. To correct for reaction probability, we simulated the detector and characterized efficiency. In the simulation, recoil particles passed through two separate foils that record time, before striking a detector plate. We measured global efficiency and its dependence on foil radius, particle energy, and atomic number. The simulated detector was ~95% efficient for a 1" diameter foil, and ~98-99% efficient for a 2" diameter foil. Efficiency varied 7-17% as a function of energy, and up to 6% as a function of radius. In addition, recoil elements including ^{19}F , ^{12}C , and ^{40}Ar were simulated and revealed no efficiency dependence on atomic number. These measurements can be applied to experimental detection data and used to calculate reaction probabilities in St. George.

1. Introduction

The existing knowledge of how different chemical elements are formed is enabled by our understanding of nuclear reactions in stellar cores. Helium capture reactions are experimentally observable with the use of recoil separators. The St. George separator [1], or **Strong Gradient Electromagnetic Online Recoil separator for capture Gamma Ray Experiments**, detects reaction products from (α, γ) helium capture processes. Of these products, we were interested in detecting heavier element particles such as fluorine 19 (^{19}F), the byproduct of nitrogen 15 (^{15}N) and helium 4 (^4He) fusion.

To better understand nuclear fusion reactions, the validity of stellar models needs to be boosted. Measuring an accurate reaction probability in St. George implies an equivalent statistic

in stars. An accurate probability measurement requires an understanding of efficiency. Although particles are detected, St. George is not 100% efficient in that not all reaction products reach the detector. We cannot assume that all particles produced are all particles detected. Thus, analyzing the detector's efficiency is paramount to deducing an accurate reaction probability for heavier elements like ^{19}F .

In order to detect the heavier element particles, St. George operates using inverse kinematics, which reverses the target-beam roles by using a heavier ion beam (e.g. ^{15}N) aimed at a lighter target. In St. George, the lighter target is a stationary ^4He source. When a lighter target is struck by a heavier beam, the heavier beam will pass through alongside any reaction products. To separate the original beam from the reaction particles, St. George includes a velocity filter that deflects most of the ion beam away from the heavier element particles. Once the particles move to the final detector, we can distinguish the reaction particles by comparing their energies with the time they spent in the detector. Particle mass can be deduced from the time and energy data, which confirms the presence of the heavier element.

To analyze the detector's efficiency, we need a way to measure how many particles were being produced but not being detected. Consequently, a simulated detection system could fill this knowledge gap. An existing simulation[2][3] for St. George provided equivalent data to experimental results, and was used for efficiency analysis. The simulation efficiency would then indicate how many total particles were produced, and provide the necessary corrections to reaction probability for St. George.

To analyze simulation efficiency, we focused on the heavier element particles that were not detected. In St. George, particles travel through two separate foils before hitting the surface of a silicon detector. The foils are necessary for recording elapsed time, whereas the silicon

detector measures final energies. In the simulation, we can also record position, initial energy, and momentum. Despite the foils' necessity, they lower the efficiency of both the simulation and St. George by scattering the striking particles, causing energy and detection losses.

In order to obtain a full efficiency characterization, we simulated adjustments to the foils and recoil particles, and measured the resulting efficiencies. The detection system uses two types of foils, varied by size, thickness, and material. Each configuration may impact how many particles deflect. We were also interested to see if efficiency depended on radius and energy. Meaning does the position the particle hits the first foil, or its initial energy, affect its chances of being detected? And does this vary with the type of foil as well? Additionally, heavier elements with different atomic numbers may yield higher or lower detection counts. For this purpose, we also considered carbon 12 (^{12}C) and argon 40 (^{40}Ar) as incoming ions in simulation, to compare with ^{19}F . All of these measurements and adjustments would allow us to achieve an independent characterization of efficiency. An independent characterization would provide corrections for the rate at which heavier elements are formed using St. George.

2. Operating the St. George Simulation Detector

The computerized simulation for St. George simulates the final detector chamber of the recoil separator, depicted in Fig. 1.

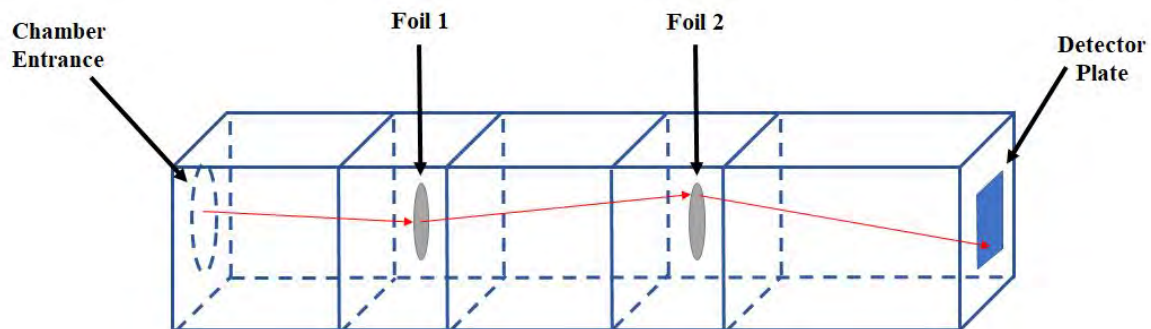


Figure 1. Model of the simulated detector chamber for St. George, or Strong Gradient Electromagnetic Online Recoil separator for capture Gamma Ray Experiments. Heavier element particles, produced in a helium capture reaction, are focused into the chamber entrance by a quadrupole magnet. Particles pass through two foils, necessary for recording elapsed time, and stop in a silicon detector that records kinetic energies. The thin arrow shows a sample trajectory for a successful particle detection. Particles that deflect and miss the foils or detector plate are detection losses and lower the efficiency of the simulation and St. George.

The reaction products are focused by a magnet into the chamber entrance. The particles' initial positions, energies, and momentum directions are recorded at the entrance. At foil 1, foil 2, and the detector plate, we again record particle positions, energies, momentums, and elapsed times in the chamber. Most, if not all, particles will hit foil 1 before beginning to deflect. A successful detection is defined by a particle that strikes both foils and the detector. Particles that miss foil 2, miss the detector, or lose all of their initial energy are not counted and thus reduce the overall efficiency of the detector.

To set up a simulation, we would first initialize a starting amount of heavier element particles. For the sake of simplicity, we disregarded the presence of remaining ion beam particles that weren't removed by the velocity filter. We would declare the atomic number and nucleon count of the element being considered. An initial energy range was declared to approximate a 0.2MeV/nucleon minimum to 2.0MeV/nucleon maximum. We randomly generated striking positions on both foils to set initial momentum directions for the particles. Adjustments to the detector design, including foil dimensions and composition, were also performed for various simulations. After completing a simulation, we processed the data and measured detection counts for total efficiency. We also analyzed efficiency as a function of radius and initial energy to observe any dependencies.

3. Simulating reactions of ^{19}F , ^{12}C , ^{40}Ar

There were six separate simulation runs performed, two for each ion. St. George exchanges two separate foil sizes: one- and two-inch diameter foils. The 1" foils accept ions with a smaller energy distribution and incoming angle. Smaller foils are suitable for ions with approximately +/- 3% in energy distribution, which fall within a ~20 mrad incoming angle. The 2" foils accept ions with both a larger energy distribution and incoming angle. For our simulation

purposes, the foils' ion suitability was irrelevant to characterizing the efficiency of the detector. Instead, we simulated at both foil sizes in order to compare differences in energy and radial dependencies. Thus, two simulations per ion, one for each foil, was appropriate.

The ^{19}F isotope was simulated with an atomic number of $z = 9$, 19 nucleons, and an initial energy range of 4.0 MeV to 40 MeV. Similarly, for ^{12}C , created from beryllium 8 (^8Be) and ^4He , the parameters were $z = 6$, 12 nucleons, and an energy range of 2.4 MeV to 24 MeV. Following with ^{40}Ar , the product of sulfur 36 (^{36}S) and ^4He , the parameters were $z = 18$, 40 nucleons, and an energy range: 8.0 Mev to 80 MeV. These elements were chosen for their atomic numbers. If there was an efficiency dependence on z , particles with sufficient differences in value would need to be analyzed. Although ^{19}F and ^{12}C were relatively close in atomic number, we anticipated that ^{40}Ar , at twice the atomic number of ^{19}F , would indicate dependence if it existed.

4. Efficiency Behavior for 1" and 2" Foils

Simulations for ^{19}F , ^{12}C , and ^{40}Ar reaction elements were run using the 1" and 2" foil configurations. Each simulation had an input of 1,000,000 particles, which allowed for a more precise analysis of efficiency statistics. Global sample efficiencies were 95.64% for ^{19}F , 94.89% for ^{12}C , and 95.54% for ^{40}Ar using 1" foils. For the 2" foils, global efficiencies were 98.24%, 97.89%, and 98.15% respectively. From these data it can be seen that, on average, St. George detected approximately 95-98% of all recoil particles created in reaction. This was a satisfactory finding, in that the reaction probability would only need a 2-5% correction for undetected particles. In addition, the lack of variation in ion efficiencies suggests efficiency independence from atomic number.

For a comprehensive analysis, efficiency was recorded in function of initial energy. From ^{19}F data, efficiencies were calculated for every set of particles within a 1MeV sample. Given the energy range of 4.0MeV to 40MeV, there were 36 separate efficiencies. For a direct comparison

with ^{12}C and ^{40}Ar , efficiencies were calculated every 0.6MeV and every 2.0MeV respectively, providing 36 data across the 2.4MeV to 24MeV and 8.0MeV to 80MeV ranges. Calculated efficiencies, as functions of initial energies, were plotted in Fig. 2, using 1" foils, and Fig. 3, using 2" foils. Initial energy was given in terms of energy per nucleon for x-axis uniformity.

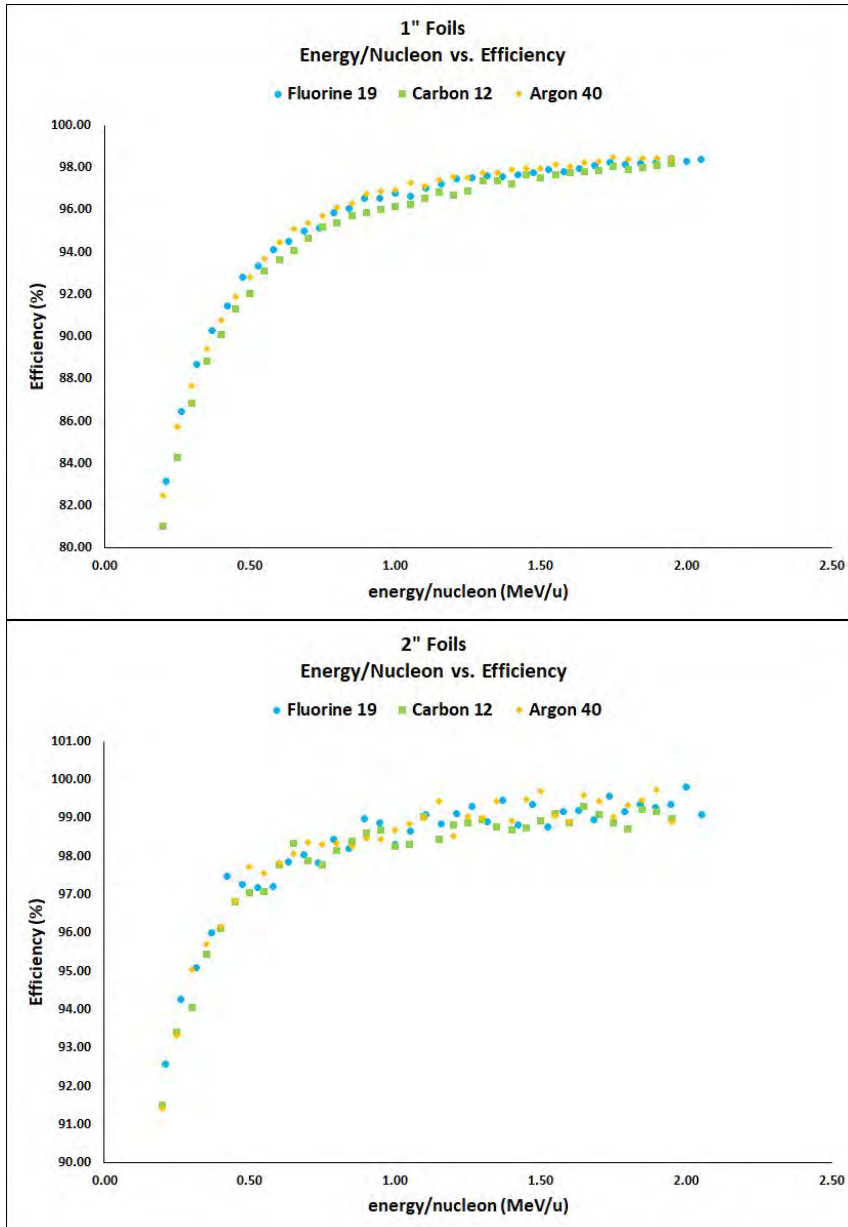


Figure 2. Plot of efficiency as a function of energy/nucleon for simulations of the St. George detector using 1" foils. Simulation data for recoil particles: ^{19}F , ^{12}C , and ^{40}Ar are shown. Each element is simulated with initial particle energies corresponding to 0.2MeV/nucleon to 2.0MeV/nucleon. Particles with lower initial energies have lower efficiencies, and are less likely to be detected. Particles with higher initial energies have higher efficiencies, and are nearly guaranteed to be detected. There are negligible differences between each element, which implies that efficiency does not depend on the atomic number of the particle.

Figure 3. Plot of efficiency as a function of energy/nucleon for simulations of the St. George detector using 2" foils. Simulation data for recoil particles: ^{19}F , ^{12}C , and ^{40}Ar are shown. Each element is simulated with initial particle energies corresponding to 0.2MeV/nucleon to 2.0MeV/nucleon. Particles with lower initial energies have lower efficiencies, and are less likely to be detected. Particles with higher initial energies have higher efficiencies, and are nearly guaranteed to be detected. There are negligible differences between each element, which implies that efficiency does not depend on the atomic number of the particle.

Both Figure 2 and 3 demonstrate clear efficiency dependence on initial energy. Particles that had lower initial energies were less likely to be detected, and those with higher initial energies were more likely to be detected. This relation was anticipated due to the likelihood that

a lower energy particle could lose most, if not all of its energy at the foils. For each element, energies greater than 1.0MeV/u had minimal efficiency improvements, seen in the plateauing behavior of the curves. Average efficiency range varied about 17% from low to high energies in 1" foils, versus only 7% in 2" foils. This discrepancy is explained upon further analysis of the 2" foils, in particular the efficiency dependence on radius. Also, since each element follows a similar curve, there is further evidence that efficiency has no z-dependence.

A similar analysis was performed to investigate the effect of foil striking radius on efficiency. When particles enter the detector, they are focused to strike the first foil. Their striking positions on this foil can range from inner to outer radii. Radial increments of 0.72 mm were considered, for a total of 18 efficiency measurements with 1" foils, and 36 with 2" foils. By measuring efficiency in this way, as with energy dependence, we sought to confirm or deny the hypothesized behavior. Efficiency dependence on radius made sense. If a particle struck the first foil at a wider radius, it had a greater chance of deflecting and missing the second foil and silicon detector. Similar to the energy analysis made previously, efficiencies were measured for each radial increment, and plotted in Figs. 4 and 5. Again, all three elements were superimposed to simultaneously evaluate any differences from atomic number.

In Figure 4, there appears to be no significant change in efficiency going from inner to outer foil radii on the 1" foils. On average, there is a ~95% chance that particles striking anywhere on the 1" foil will be detected. To justify this variance from expected behavior, the overall size of the 1" foil could have just lacked enough radius for efficiency to have a noticeable dependence. Meanwhile, in Fig. 5, there was an efficiency dependence on where the particles struck the 2" foils. This dependence did not become apparent until after half the full radius, which explained the lack of radial dependence using the 1" foils. Particles that struck the first

foil within 12.7 mm were detected at 100% efficiency. Particles beyond 12.7 mm were detected at decreasing efficiencies for increasing radii, varying 6% across the entire foil size. This dependence was observed with equivalent statistics for all three elements.

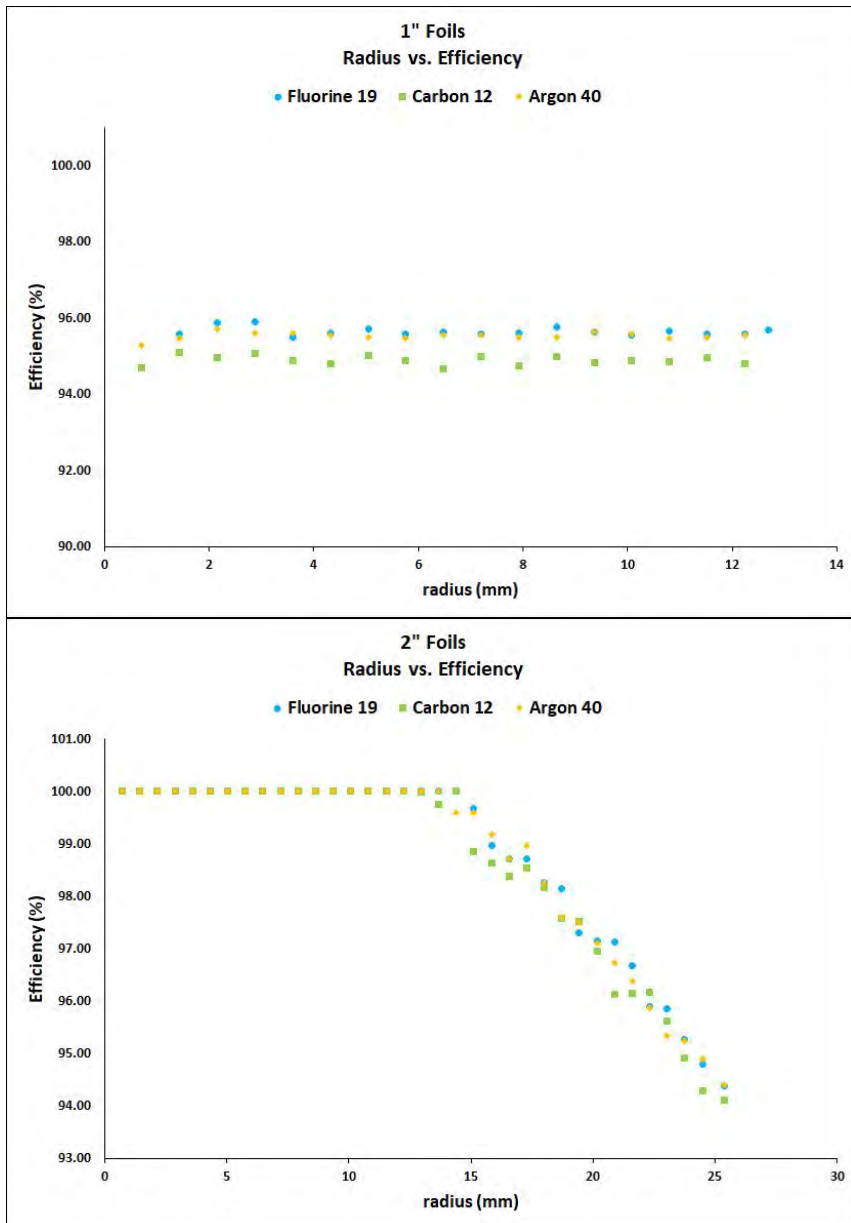


Figure 4. Plot of efficiency as a function of striking radius on 1" foils for simulations of the St. George detector. Simulation data for recoil particles: ^{19}F , ^{12}C , and ^{40}Ar are shown. Efficiencies for particles in radial increments of 0.7 mm are calculated and shown. There is no significant dependence of efficiency on radius for the smaller foils. The foils are likely just small enough for there to be no effect. Furthermore, the agreement of the three elements' efficiencies supports a lack of efficiency dependence on atomic number.

Figure 5. Plot of efficiency as a function of striking radius on 2" foils for simulations of the St. George detector. Simulation data for recoil particles: ^{19}F , ^{12}C , and ^{40}Ar are shown. Efficiencies for particles in radial increments of 0.7 mm are calculated and shown. There is no significant dependence of efficiency on radius below 12.7 mm. There is an efficiency dependence on radii beyond half of the full radius. Particles that strike the foil at outer radii have a lower chance of detection than those that strike within 12.7 mm. Agreement among the three elements supports efficiency independence from atomic number.

Since efficiency only depended on initial energies for the 1" foils, the larger efficiency variance indicated that initial energies had a greater independent impact. For the 2" foils, efficiency depended on both initial energies and foil striking radius. Dependence on energy contributed part of the overall efficiency behavior, with a lesser independent impact. Dependence

on energy and foil striking radius comprised the full impact and efficiency variation associated with low to high energies and inner to outer radii.

5. Remarks and Conclusions

By characterizing the efficiency of St. George in simulation, reaction probabilities can be measured, thereby boosting the validity of stellar models. Three beam ions, ^{19}F , ^{12}C , and ^{40}Ar were simulated for 1" and 2" foil configurations. Global efficiencies were found to be ~95% using 1" foils, and ~98% using 2" foils. The smaller foil provided a smaller target for particles to strike after scattering, which explains the lower percentage. Efficiency did depend on initial particle energies for both foils, but only on radius for the 2" foils. Data from the 2" foils showed that efficiency did not vary inside half of the full radius, which supported the lack of dependence in the 1" foils. The efficiency behavior, in function of energy and radius, were superimposed for each element. There were negligible differences in efficiency behavior among the ions. This lack of dependence on atomic number allows for standardized corrections to reaction probability.

Further characterizations of efficiency are being made to include the effect of magnetic fields, as well as how closely detected particles fit the time versus energy relationship. The more comprehensive the characterization of efficiency, the more accurate the reaction probability will be. For an accurate probability, the validity of St. George can be trusted to study behaviors of nuclear reactions. The use of recoil mass separators like St. George can then further our understanding of how chemical elements are created in stars.

6. References

- [1] M. Couder et al. "Design of the recoil mass separator St. George". In: *Nuclear Instruments and Methods in Physics Research A* 587.1 (Mar. 2008), pp. 35-45. DOI: 10.1016/j.nima.2007.11.069.
- [2] S. Agostinelli, et al., GEANT4 - A simulation toolkit, *Nucl. Instrum. Methods Phys. Res. A* 506 (2003) 250–303
- [2] Brun R and Rademakers F ROOT Object Oriented Data Analysis Framework *New computing techniques in physics research V. Proceedings, 5th International Workshop, AIHENP '96 (Lausanne, Switzerland, September 2-6, 1996)*

REACH OUT FOR SCIENCE OUTREACH:

THE U.S. NEEDS YOU!

MC KENNA CORINNE WALLACE

2020 NSF/REU Program
Physics Department, University of Notre Dame

ADVISOR: Dr. Michael Kilburn

Abstract:

Not everyone needs to be a professional scientist, but in order to make informed decisions about society, we need to raise the nation's scientific literacy. According to Jon Miller (a researcher from Michigan State University), "approximately 28 percent of American adults currently qualify as scientifically literate... Over recent decades, the number of public policy controversies that require some scientific or technical knowledge for effective participation has been increasing..."[4]. One of the easiest ways to increase scientific literacy is science outreach, yet it is often an afterthought. In this paper, I will discuss a few ways I did science outreach this summer: Zoom activities like rock candy, recycling old paper/junk mail into new paper, and making paper circuits. I also improved the current ion trap Notre Dame uses as a demonstration, and finally, I mentored three high school physics students for a week. Through my personal experience, I have seen nonscientists grow to be curious critical thinkers. Now, more than ever, we need to continue to perform this kind of outreach in order to increase scientific literacy.

Introduction:

From policy making about Global Warming to flat Earth arguments to Autism and the anti-vaccination movement, scientific literacy plays an important role in how our society progresses and makes informed (or **uninformed/misinformed**) decisions. According to the National Science Education Standards (NRC, 1996), scientific literacy is defined as, "the knowledge and understanding of scientific concepts and processes required for personal decision making, participation in civic and cultural affairs, and economic productivity." [1] They

elaborate by explaining people who are scientifically literate are able to: answer to questions from their own curiosity, explain and predict natural phenomena, read, understand, discuss articles about science in popular media, identify scientific issues requiring national and local decisions, and use evidence and data to evaluate the quality of information and arguments by scientists and the media.

One of the easiest ways to increase scientific literacy is to do science outreach, yet it has often been an afterthought for colleges and universities. It is one of the most common ways for younger students to be exposed to and excited by science. According to Steve Shropshire, as quoted in the spring 2012 issue of Radiations (a magazine by the Society of Physics Students), “Due to limitations in school district budgets and teacher training, in many places students rarely get to do more than read about the more exciting aspects of science. Science outreach can help reverse negative attitudes, expose students to more exciting aspects of science, spark interest and enthusiasm, and encourage communities to support science education.”[2].

The goal of my research experience was to enhance science education and outreach by creating some activities to be presented over Zoom and live streamed on YouTube. Using materials commonly found at home, any person interested in the Zoom activities could tune in and follow along with the experiments. I also added a new demonstration for the physics department at Notre Dame to use in future outreach. Finally, I mentored three high school physics students for a week.

The demonstration for the physics department to use in the future is an ion trap (3-D printed parts, internal circuit, powered by a 9V battery and a power supply). We continue to work towards creating physics demonstrations for non-physicists in an engaging and exciting

way. By doing so, we hope to inspire the next generation of scientists and critical thinkers, and raise the scientific literacy of the US.

In this paper, I will discuss a few of the online activities- making rock candy, recycling old paper/junk mail into new paper, and making paper circuits. I will also describe the procedures used to fix/improve the current ion trap Notre Dame uses as a demonstration, and my experience mentoring three high school physics students for a week.

Zoom/YouTube Live Art 2 Science Activities:

I led three Zoom/YouTube live activities for Notre Dame's *Art 2 Science* summer program: making rock candy, recycling old paper/junk mail into new paper, and making paper circuits. I will only describe methods in detail for the rock candy activity. The other two activities did not have as many participants and the idea for increasing scientific literacy is the same for all three activities: get students to ask questions, propose ideas, and develop further experiments.

The Zoom/YouTube live rock candy activity was intended for children as young as five to do without parental supervision. I adapted the usual methods of making rock candy to work for that audience. For all the following instructions, I also verbalized and showed the children what I was doing for each step and paused for questions.

In a microwave safe dish, I poured 1 cup of water. I then added 1/4th cup of sugar and mixed until the water was clear. I added another 1/4th cup of sugar and mixed again. At this point, mechanical mixing will not dissolve all the sugar into the water; we need heat. I microwaved the mixture for thirty seconds and then mixed again. I continued this step until the mixture was clear. I added another 1/4th cup of sugar and repeated the mix-microwave-mix

routine until the sugar was completely dissolved. This process was repeated until two cups of sugar were dissolved in the one cup of water. While the mixing process was being repeated, the children asked questions. Some of my favorite were:

- Can I put lemon juice in? Would my rock candy be lemon flavored?
- Can I put peppermint oil in?
- Can I make this with brown sugar?

The last question led into a discussion of different things we might be able to dissolve in water and make crystals with. The children came up with salt, honey, artificial sweeteners, and maple syrup.

When the two cups of sugar were completely dissolved in the water , I dipped two bamboo skewers in the sugar water mixture, then rolled in dry granulated sugar. I set these on wax paper and let them dry. While the skewers were drying, I prepared the jars that the rock candy would form in. I poured the sugar water mixture into two wide mouth 16 ounce mason jars. I secured wooden clothes pins to the bamboo skewers so that the clothes pins would lay across the mouth of the mason jar and hold the skewer in the center of the jar, not touching the sides or bottom.

I placed the two jars on my windowsill and advised the children participating to do the same. This provoked some interesting questions:

- What if I put it somewhere dark? Is it better in the light?
- Can I put one jar in the fridge and one in the freezer?
- Will it work faster if I put my jars outside?

We discussed heat and evaporation, and the role they play in crystals forming. The children were full of ideas to try and questions about what we did and what they could try. These questions show that they are curious, and their attempts to answer these questions for themselves and each other promote their understanding of the world and their scientific literacy.

Quadrupole Ion Trap:

The quadrupole ion trap that I was given to work on was originally created by freshman physics students at Notre Dame following the instructions and using the schematics from a CERN high school activity from 2018. The STL files for the 3D printed parts are available on the CERN website[3]. Unfortunately, the ion trap the students built no longer worked due to materials such as conductive paint flaking off, and parts not being securely aligned. I was given the task of fixing and improving the ion trap so that it can be used in future Notre Dame physics demonstrations.

The CERN 2018 quadrupole ion trap has the option of a simple LED in a circuit with an on/off switch (Figure 1) or a strobing LED in a circuit with a strobe/off/on switch (Figure 2). The students originally created the simple circuit, so to improve the demonstration, I converted to

the strobe circuit.

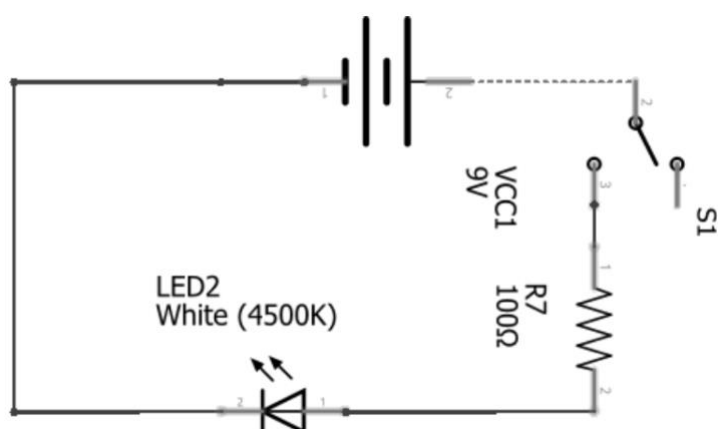


Figure 1 (left). Simple LED circuit diagram from CERN's 2018 Quadrupole Ion Trap activity.[3]

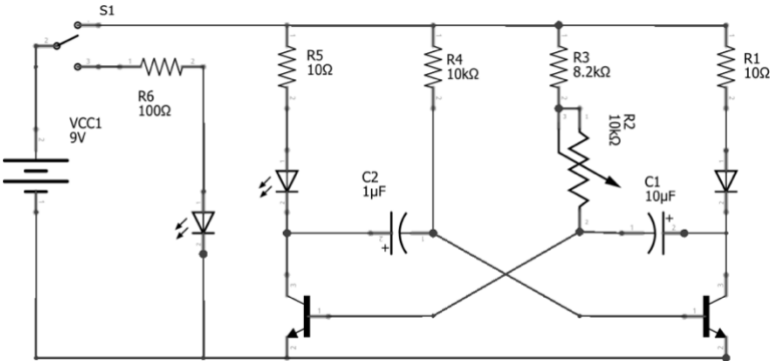
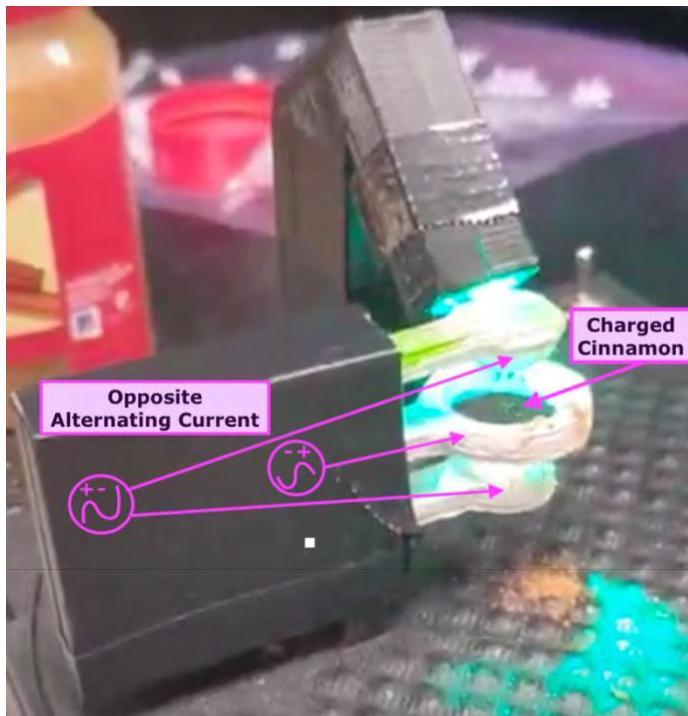


Figure 2 (right). Astable multivibrator circuit diagram for the strobing LED from CERN's 2018 Quadrupole Ion Trap activity.[3]

Once the strobe circuit was working, I began fixing the 3D printed components. I reprinted some parts that were not printed well or had worn down or broken.

With all the parts printed and assembled for the ion trap, I only needed to figure out how to make the endcap electrodes and ring conductive. I tested conductive paint, flux paste,



conductive 3D printing filament, and conductive ink. I found conductive ink to be the best choice and completed the ion trap by coating the endcap electrodes and ring in conductive ink. After assembling the entire device, and testing it using ground cinnamon as our charged particles, we found that it worked (Figure 3).

Figure 3 (above). The working quadrupole ion trap, showing the endcap electrodes and ring with opposite AC, causing the cinnamon to float in the ring.

Mentoring High School Physics Students:

My favorite part of my time at Notre Dame's Physics REU Program was mentoring three high school physics students for a week through JINA-CEE's online version of the Physics of

Atomic Nuclei Program (PAN Program). Due to COVID-19, this experience was converted from in-person to virtual. For four afternoons, I went to the Notre Dame campus, set up equipment for our experiment, and logged on Zoom with a senior and two juniors in high school. We did atomic spectroscopy by running a current through a gas tube and looking through a diffraction grating. I moved the camera and the students took data and measurements, then solved for wavelengths and used patterns to identify what the gas in the tube was (see Figure 4).

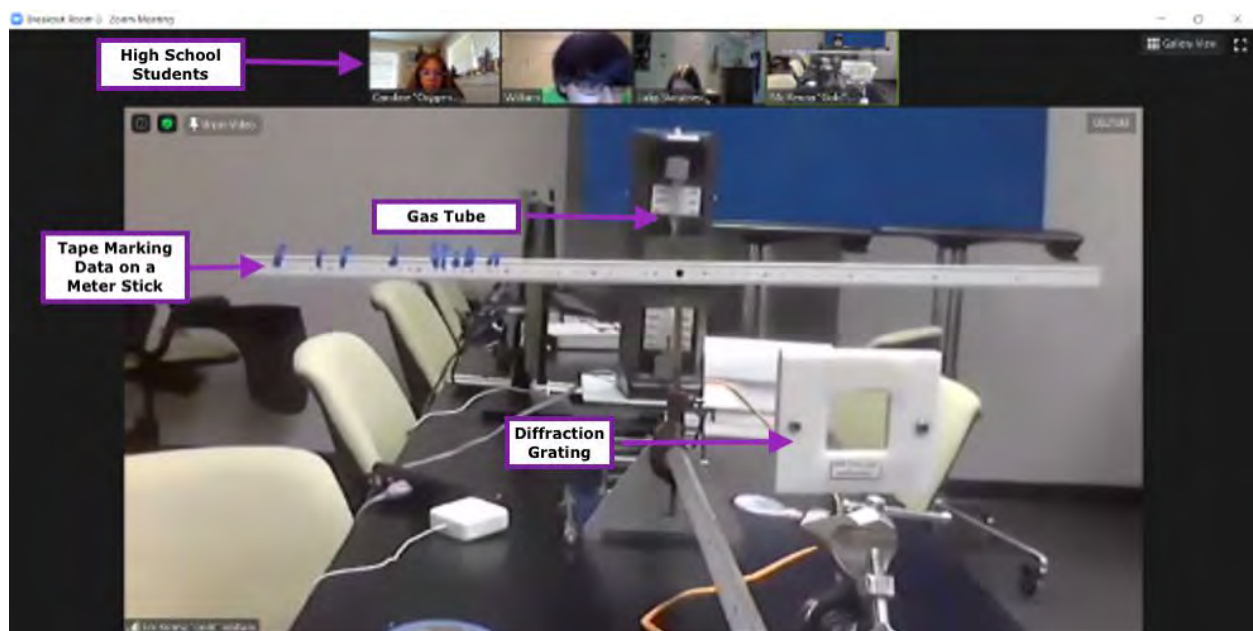


Figure 4 (above). A screenshot of our Zoom call and experimental set up, with labels. The gas identified by the students from this setup was helium.

We spent the first three days working with this set up and two gases, hydrogen and helium. The last day we extended the experiment to the world outside of the lab. Using a piece of black paper, tape, a needle, a diffraction grating, and our phones we took pictures of the solar spectrum and attempted to identify elements in the sun. Using Fraunhofer lines, the students were able to identify magnesium, hydrogen, iron, sodium, helium, and oxygen. Once the experiments were completed, the students created a capstone presentation of their

research project on atomic spectroscopy and presented it via Zoom to all PAN participants and coordinators (see Figure 5).

This was the most rewarding part of my summer research at Notre Dame: watching the three high school students discuss the experiments we did, their interpretations, and further applications of the methods we used. They started the program with only an interest in physics but finished with physics research experience and ideas for their future.

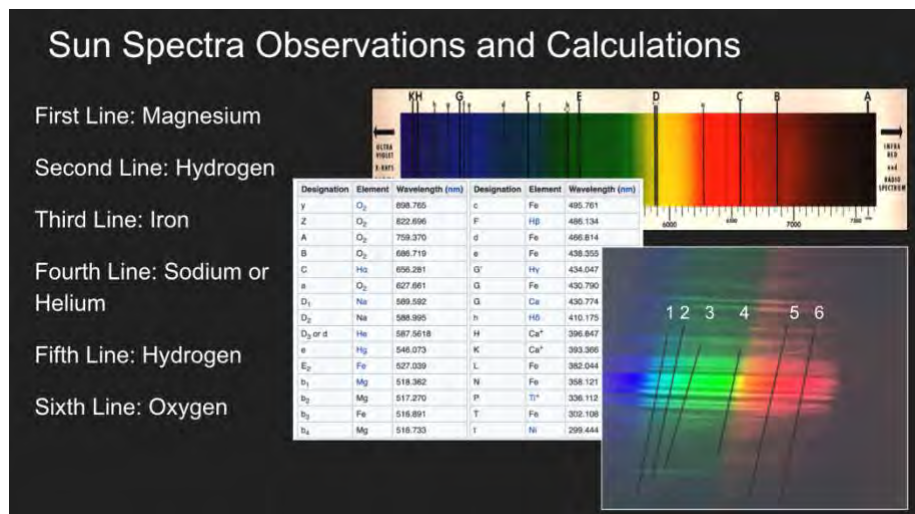


Figure 5 (left). A slide from my students' presentation on their solar spectroscopy experiment showing what elements they found and how they identified those elements.

Conclusion:

Not everyone needs to be a professional scientist, but in order to make informed decisions about society, we need to raise the nation's scientific literacy. According to Jon Miller (a researcher from Michigan State University), "approximately 28 percent of American adults currently qualify as scientifically literate..."[4]. With over 70% of American adults scientifically illiterate, we should be scared. We should be motivated to solve this issue. Outreach, interesting science demonstrations, and modeling inquiry are key if we want to increase the scientific literacy in the United States.

By bringing science home in the *Art 2 Science* family activities I did over Zoom, building an ion trap that Notre Dame will use for physics demonstrations to non-physics majors, and mentoring three high school students, I hoped to bring more science and inquiry into the life of the average American. This is particularly challenging during COVID-19, with in-person science outreach being converted into online. The work to improve the U.S.'s scientific literacy is far from over, and as I continue to learn and to teach, I continue to work towards a more scientifically literate United States of America. Whether virtually or in person, I encourage all scientists to do the same!

References:

- [1]. National Research Council. (1996). *National science education standards*. Washington, DC: National Academy Press.
- [2]. Shropshire, Steve. *The Importance of Science Outreach*. 30 Sept. 2015,
www.spsnational.org/the-sps-observer/spring/2014/importance-science-outreach.
- [3]. "CERN Quadrupole Ion Trap." *3D-Printable Quadrupole Ion Trap / S'Cool LAB*, CERN, 2018,
scoollab.web.cern.ch/3d-printable-quadrupole-ion-trap.
- [4]. Michigan State University. "Scientific Literacy: How Do Americans Stack Up?." ScienceDaily.
ScienceDaily, 27 February 2007.
www.sciencedaily.com/releases/2007/02/070218134322.htm

Variance extrapolation in an oscillator basis

Isabella Zane

2020 NSF/REU Program

Physics Department, University of Notre Dame

Advisor: Dr. Mark Caprio

1 Abstract

Solving the many-body problem using the no-core shell model (NCSM) is challenging due to the increasing computational demands as nucleons are added. The full-space solution can be approximated by extrapolating from solutions in finite spaces. However the quality of the approximation is limited by the largest space computational methods can handle. Extrapolation techniques can be used to increase precision without increasing computational demands. Variance extrapolation has been used to successfully predict energies of the Monte Carlo shell model. We now want to understand if the method can be extended to the NCSM based on a truncated oscillator basis. Variance extrapolation uses energy variance as an indicator of the precision of the approximation since the energy variance is the variance of the larger space. We expect to find a linear relationship between the error in the calculated energy and the energy variance for the wave function. Therefore, we can then extrapolate to zero variance in order to find the energies of the full space. We first explore how this method works in finite oscillator bases by solving a simpler one dimensional problem. We then apply the method to the more complicated nuclear problem such as light nuclei.

2 Introduction

The solution to the Schrodinger equation for the complete no core shell model gives us the eigenvalues and eigenstates of the system. This provides

valuable information such as the allowed energies of the quantum system as well as the probability amplitude. However, solving the problem for the complete many-body problem in the NCSM is computationally challenging due to the size and complexity of the eigenvalue problem. The energies of the nuclei are calculated by diagonalizing the Hamiltonian matrix of the system. Thus in order to obtain a sufficiently accurate solution, the dimension of the square Hamiltonian matrix approaches infinity. The computational power necessary to diagonalize such a large matrix is extremely challenging to satisfy and thus very inefficient. Therefore, current methods of solving the Schrodinger equation for nuclei involve truncating the basis to a finite Hilbert space. One is then able to calculate the eigenvalues of the Hamiltonian in the truncated finite basis and use these results to make predictions about the eigenvalues for the complete space. Since this space is finite, the accuracy of such an approximation is limited to the largest space current computational methods can handle. Since the complexity of the problem grows exponentially as particles are added to the system, there only exist solutions for light nuclei such as H and He. Therefore, the challenge is to find a method to improve the accuracy of the predictions of the eigenvalues without increasing computational demands. [1]

The aim of this paper is to explore a method of approximating the Schrodinger equation solution for the complete problem by utilizing properties of variance in eigenstates to accurately extrapolate data. We will first solve a one dimensional Schrodinger problem of a Gaussian potential in an

oscillator basis. After, we will apply the variance extrapolation method to this simpler ‘toy’ problem in order to see how solutions behave and what methods of extrapolation work best. The research discussed in this paper will mostly cover this initial problem and the results.

The fundamental property of variance that is used is the fact that the variance of the energy calculated in an eigenstate is zero. Moreover the approximate energy eigenstate calculated in a truncated space has zero variance when calculated in the same space. However, when the eigenstate is embedded in a larger space, the variance is non-zero. The more accurate the eigenstate approximation is in the larger space, the closer the variance value will be to zero. Thus, in a good wave function approximation, the variance approaches zero linearly as the energy approaches the true eigenvalue in the full space. The variance extrapolation method calculates approximate wave functions in a sequence of increasing truncated spaces to find the linear relation between energy and variance. Then, by extrapolating the data to zero, one is able to find the eigenvalues of the full space.

In exploring the method of variance extrapolation, the first challenge will be to determine if there is even a linear relationship between the energy eigenvalues of the successive truncated spaces and energy variance. If so, we will need to quantify the linear relation and determine which values of space dimension should be weighted differently and how. Moreover, the challenge will be to find a generalized method of extrapolating the data to zero variance which yields accurate predictions that can be compared with experimentally

verified results of light nuclei. Many methods of approximating energy eigenvalues of the complete space are not compatible with heavier, more complex nuclei. Additionally, there is not as much experimentally verified results to compare the theoretical predictions with due to the computational demands of increasingly complex nuclei. The final challenge of this project will be to determine if the method is even extendable to these complex nuclei for which accurate predictions are greatly needed.

3 Method

In order to build better intuition for the variance extrapolation method, we first consider the one-dimensional ‘toy’ eigenproblem for a Gaussian potential. The Hamiltonian is thus,

$$\hat{H} = \frac{\hbar^2}{2m} k^2 - V_0 e^{-\frac{1}{2}(\frac{x}{s})^2}$$

Which can be simplified to a ‘dimensionless’ Hamiltonian of the form,

$$\hat{H} = k^2 - V(x)$$

We will solve this problem in a one-dimensional oscillator basis with oscillator length b , i.e,

$$\phi_n(x) = (b 2^n n! \sqrt{\pi})^{\frac{-1}{2}} e^{-\frac{1}{2}(\frac{x}{b})^2} H_n(\frac{x}{b})$$

Where $H_n(\frac{x}{b})$ are Hermite polynomials of the n^{th} order. The differential operator of Gaussian problem is then converted to a matrix operator so it can be diagonalized numerically in order to obtain the eigenvalues. The matrix elements of the Hamiltonian are found by the following,

$$H_{ij} = \langle i | H | j \rangle = \int_{-\infty}^{\infty} \phi_i^*(x)(k^2 - V(x))\phi_j(x)dx$$

The Hamiltonian is then diagonalized using numerical techniques and the final result expressed in matrices is of the form,

$$\begin{pmatrix} H_{00} & H_{01} & \dots \\ H_{10} & H_{11} & \\ \vdots & & \ddots \end{pmatrix} \begin{pmatrix} \psi_0 \\ \psi_1 \\ \vdots \end{pmatrix} = E_n \begin{pmatrix} \psi_0 \\ \psi_1 \\ \vdots \end{pmatrix}$$

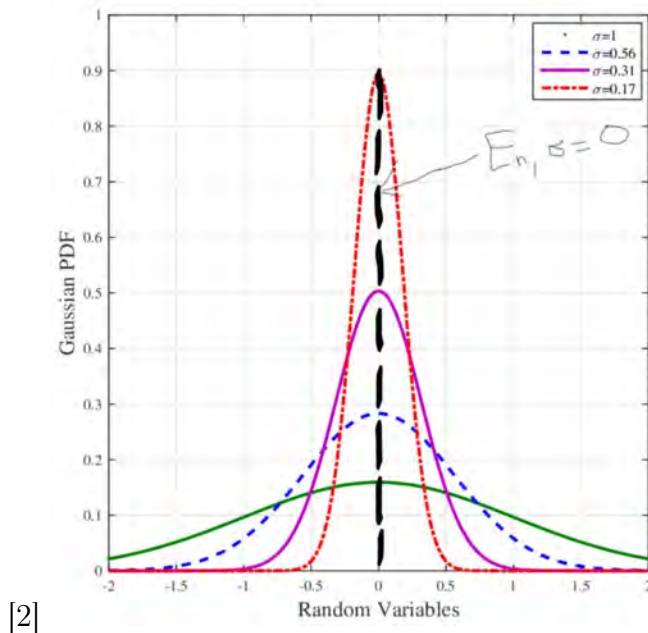
Where ψ is the eigenfunction and E_n is the corresponding eigenvalue of the Hamiltonian operator.

In order to present our variance extrapolation method, we first define what energy variance in a truncated space means. The expression we will use is defined as

$$\sigma_E^2 = \langle \hat{H}^2 \rangle - \langle \hat{H} \rangle^2$$

Variance is statistically defined as a measure of how far the spread of a data set deviate from the average value. This conceptually can be understood as the spread of the probability density of energy in the space. Physically

observable properties of a system are represented by Hermitian operators. The eigenvalues of these operator contain every possible energy of the observable when measured. If the energy variance is being calculated in the same eigenstate, it will result in zero energy variance. Since this value is being calculated in the same eigenstate, there exists a definite solution (the eigenvalue) and the probability density function collapses around the eigenvalue.[1]



[2]

Moreover,

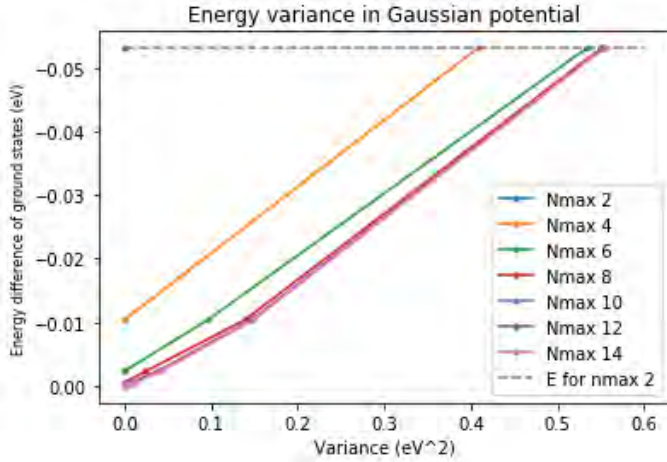
$$\langle \hat{H} \rangle = \int_{-\infty}^{\infty} \psi^* H \psi = E \int_{-\infty}^{\infty} \psi^* \psi = E$$

Thus, $\langle \hat{H} \rangle^2 = E^2$, for all spaces. However, if the energy variance is calculated in a different eigenstate, we will have $\langle \hat{H}^2 \rangle \neq \langle \hat{H} \rangle^2$, so the energy variance will be nonzero.

In order to gauge the accuracy of an approximation of a larger space from a smaller truncated space, we embed the energy estimate in the larger space and calculate the variance. Let the wave function approximation of the smaller space be denoted ψ_{n1} , similarly let the energy eigenvalue of the smaller space be denoted E_{n1} and the larger, \hat{H}_{n2} . Then we can rewrite the variance calculation as

$$\sigma_E^2 = \psi_{n1}^* \hat{H}_{n2}^2 \psi_{n1} - E_{n1}^2$$

To collect data points for variance extrapolation, we calculate the energy variance in successively larger spaces. For example, if the large space has the maximum order of basis function $n_{max} = 6$, we will perform three energy variance calculations. First, the eigenvalue of a space with $n_{max} = 2$ is embedded in $n_{max} = 6$ and then the variance is calculated in the larger space of the two. The same procedure follows for the $n_{max} = 4$ space in $n_{max} = 6$ and so on until the energy variance is calculated in the same space as the eigenvalue. This is done for successively larger spaces in steps of two and extrapolation is carried out in each. This can be seen in the following diagram. The energy difference denotes the difference between the energy eigenvalue of the smaller space and the energy of the complete space which was calculated at $n_{max} = 40$. This data was calculated with $V_0 = 10$, $b = 1$, and $s = 1$.



Extrapolation uses the linear relationship between close embedded spaces in order to approximate the function in the full space. This is done by forming a line between two successive points. Then the y-intercept at zero variance denotes the extrapolated approximation. Difficulty lies in determining which two points form the best linear relationship and whether certain spaces should be weighted differently than others.

4 Results and Analysis

The following data will be of the form (a, b) , where a denotes the maximum order of oscillator functions in the smaller embedded space and b denotes the same variable for the larger space. The percent error denotes the accuracy of the approximation to the actual solution.

| point 1 | point 2 | percent error |
|---------|---------|---------------|
| (2,8) | (4,8) | 842.74 |
| (4,8) | (6,8) | 5.46 |
| (2,8) | (6,8) | 112.12 |
| (2,10) | (4,10) | 3802.86 |
| (4,10) | (6,10) | 446.68 |
| (6,10) | (8,10) | 34.86 |

The variance extrapolation method was somewhat accurate in each case, however the accuracy is heavily dependent on which data points were used. From the data we collected, it seems that forming a linear relationship between adjacent data points which are closest to the large space produce the best results. Further analysis of various extrapolation techniques is required before methods can be expanded to the more complex problem of light nuclei.

5 References

- 1 Cresser, J D. Probability, Expectation Value and Uncertainty. physics.mq.edu.au/~jcresser/Phys301/Chapters/Chapter14.pdf.
- 2 Abd-Alaziz, Wael, et al. “Non-Binary Trellis Codes on the Synthetic Statistical MIMO Power Line Channel.” 2018 IEEE International Symposium on Power Line Communications and Its Applications (ISPLC), 2018, doi:10.1109/isplc.2018.8360199.